Ultra-Wideband Array Antennas

Von der Fakultät für Ingenieurwissenschaften

Abteilung Elektrotechnik und Informationstechnik

der Universität Duisburg-Essen

zur Erlangung des akademischen Grades

Doktor der Ingenieurwissenschaften (Dr.-Ing.)

genehmigte Dissertation

von

Zainul Ihsan

aus

Jambi/Indonesien

Abstract

Wireless communication has become an indispensable part of modern life. One of the most important components of wireless communication systems are antennas, termed as "eyes" and "ears" of communication systems. A printed antenna, one of the most commercial antennas, is widely used for civil and military applications, i.e., for communication systems, radar systems, satellite and transportation systems since the printed antenna provides some benefits such as light weight, compact structure and low manufacturing cost. A printed antenna design for a communication technology called Ultra-Wide Band (UWB) is discussed in this dissertation.

Ultra-Wide Band communication has undergone intensive investigation in the past decade since the Federal Communications Commission (FCC) released the free license spectral mask operation of the UWB radio over 7.5 GHz bandwidth from 3.1 to 10.6 GHz (UWB frequency range), a technology promising high-rate data transmission over a short range. On the other hand, a UWB communication system requires extremely low radiation power to avoid interferences to other communication systems. As an answer for this challenge, three strategies based on antenna aspects are proposed in the frame of this work.

The first strategy is to design a compact and directive single radiator. The printed monopole antenna was selected as the radiator, in particular the printed circular monopole antenna (PCMA), was reinvestigated and modified as a directive PCMA. Secondly, a UWB array antenna employing the directive PCMA element was designed to focus the radiation toward a certain direction. Some matching techniques were combined in the design to achieve impedance matching over the UWB frequency range. The measurement result of the antenna under test showed a focused radiation pattern and the impedance matching better than -10 dB was achieved for the whole frequency band.

The concept of frequency invariant beam pattern antenna arrays is applied as the third strategy. The concept, adopted from the broadband sensor's theory for acoustic purpose, is applied to the microwave frame. Based on this concept, a prototype of the PCMA array fed by a set of low pass filters was realized in planar technology at the first time to achieve frequency invariant beam patterns. The measurement of the fabricated antenna showed that the beamwidth can be kept constant over the whole frequency band.

Acknowledgment

Contents

List of Tables

List of Figures

Index of Used Acronyms and Symbols

Acronyms

ADS Advanced Design System

AUT Antenna Under Test

CST Computer Simulation Technology

EBG Electronic Band Gap

EIRP Effective Isotropic Radiated Power

FCC Federal Communications Commission

FIR Finite Impulse Response

FWHM Full Width at Half Maximum

HPBW Half-Power Beamwidth

IDFT Inverse discrete fourier transformation

IEEE Institute of Electrical and Electronics Engineers

LPF Low Pass Filter

LTI Linear Time Invariant

MIC Microwave integrated circuit

PCDA Printed Circular Dipole Antenna

PCMA Printed Circular Monopole Antenna

PCMAA Printed Circular Monopole Antenna Array

SMD Surface mounted device

UWB Ultra Wideband

Latin Symbols

Vector and matrices are printed in bold in this work, if it represents a corresponding scalar in the following list. Multiple use of symbols is possible with clear distinction in the context.

a_f	Array factor in time domain
a_{nm}	Complex weighting filter coefficient
AF	Array factor
B	Susceptance
B_s	Shunt susceptance
c_r	The speed of the light in substrate material
d	The spacing between antenna element
D	Directivity
e_i	Receiving antenna impulse response
e_rad	Transmitted antenna impulse response
E_i	Received electric far field
E_i	Field of the ith element at a distant point
E_nor	Normalized pattern
E_rad	Radiated electric far field
E_ψ	Electric field on azimuth plane
$\underline{E}_\psi$	Complex representation of vector electric field on azimuth plane
E_θ	Electric field on elevation plane
$\underline{E}_\theta$	Complex representation of vector electric field on elevation plane
$\underline{E}_s$	Complex representation of vector scattered field on elevation plane
f	Frequency
f	Isolated pattern
f_i	Active element pattern
f_0	Center frequency
f_c	Cut-off frequency
f_n	Element pattern of n-th element
f_L	Frequency at the lower limit spectrum
f_U	Frequency at the upper limit spectrum
G	Conductance
G	Gain of an antenna
G	IEEE Gain
G_abs	Absolute Gain
G_TX	Peak gain

G	Complex value regarding to sensitivity of the sensor
i	Integer index
I_i	The amplitude excitation
I_0	Current
h	Impulse response
h^+	Complex impulse response
h_{R}	Impulse response of the receiving antenna
h_{T}	Impulse response of the transmitting antenna
h	Gap between the circular radiator and the ground of the Printed Circular Monopole Antenna
H	Transfer function
$H_{\gamma x}$	Filter response
H_{C}	Transfer function of the experimental channel
H_{R}	Transfer function of the receiving antenna
H_{sys}	Calibration transfer function
H_{T}	Transfer function of the transmitting antenna
k	Wave number
k	Integer index
k_1	Fractional number of wavelength
k_2	Coefficient of the filter cut-off frequency
L	Losses
L_n	Length of delay line of n-th element
n	Integer index
n	Filter order
N	Number of sampling
N	Number of the section of Wilkinson power divider
p	Maximum value of the impulse response
p	Gaussian pulse
p_i	Pole distribution
P	Integer to represent the aperture length of the linear array
P_{in}	Accepted power
P_{in}	Input power of transmission line
P_{out}	Output power of transmission line
P_{inc}	Incident power
P_{loss}	Dissipated power
P_{rad}	Radiated power
P_{refl}	Reflected power

P_{TX}	Transmitted power
r	Distance to the coordinate origin of the wavefront
R	Radius of worm-shaped quarter circle
R_{r}	Radiation resistance of the antenna
R_{g}	Resistance of generator impedance
R_{L}	Loss resistance of the antenna
R_{L}	Load resistance
S_{11}	Input reflection parameter
S_{21}	Forward transmission parameter
S	Signal incident and received at the sensor
t	Time
t	Thickness of the substrate
T	Pulse Duration
T_N	Chebyshev polynomial of N order
u_{RX}	Received voltage in time domain
u_{TX}	Transmitted voltage in time domain
U	Radiation intensity
U_{G}	Electric voltage of generator
U_{RX}	Received voltage
U_{TX}	Transmitted voltage
w_n	Complex weighting function of n-th antenna element
W	The width of microstrip line
x	Input signal in time domain
$x,\, y,\, z$	Cartesian coordinate
$x',\, y',\, z'$	Cartesian coordinate
X	Input signal in frequency domain
X_{g}	Reactance of generator impedance
X_{A}	Antenna reactance
X_L	Reactance
V_{g}	Peak generator voltage
y	Output signal in time domain
y	Output of the array
Y	Output signal in frequency domain
Y_0	Admittance of transmission line
Y_L	Admittance of the load
Z_0	Characteristic impedance
Z_{F}	Free space impedance

Z_{g}	Generator impedance
Z_{L}	Load impedance
Z_{TX}	Characteristic impedance of transmitting antenna
Z_{RX}	Input impedance of receiving antenna
Z_f	Output of linear continuously sensor

Greek Symbols

α_i	Partial value of maximum peak of impulse response
α_i	Phase excitation
β	Wave number
Γ	Reflection coefficient
Γ_m	Maximum reflection coefficient
Δf	Frequency resolution
Δf	Bandwidth
ΔL	Progressive delay
Δt	Time resolution
ϵ_r	Relative dielectric permittivity
ϵ_e	Effective dielectric permittivity
η	Radiation efficiency
η	Wave impedance
η_a	Antenna efficiency
θ	Elevation angle
θ	Electrical length
θ_0	Oriented angle
θ_m	Maximum angle
λ	Wavelength
λ_e	Effective wavelength
λ_0	Wavelength at center frequency
λ_0	Wavelength at free space
λ_L	Wavelength at the lowest frequency
λ_U	Wavelength at the highest frequency
ϕ	Phase of the field component
ϕ	Electrical length of multi-step Wilkinson power divider
φ	Phase of transfer function
τ	Group delay

τ_n	Time delay of n-th element
τ_FHWM	The width of full pulse at half maximum
$\tau_{\mathrm{r},\alpha}$	Ringing time
ψ	Azimuth angle
ω	Angular frequency
ω_c	Angular cut-off frequency
Ω_c	Normalized angular frequency
$\tan\delta$	Loss tangent

Constants

c	$2,998\cdot 10^8\,\mathrm{m/s}$	Velocity of light in vacuum
e	$2,718\ldots$	number of Euler
ε_0	$8,854\,\mathrm{As/Vm}$	Permittivity of the vacuum
π	$3,14159\ldots$	Pi

Operators and Mathematical Symbols

$Arg(\cdot)$	Argument (complex analysis)
$\delta(\cdot)$	Dirac function
$(*)$	Convolution operator
$\mathcal{F}$	Fourier transformation
$\mathcal{F}^{-1}$	Inverse Fourier transformation
$\mathcal{H}$	Hilbert transform
$\frac{\partial^n}{\partial t^n}$	Derivation n-th order
$\Re(\cdot)$	Real part
$\Im(\cdot)$	Imaginary part
∞	Infinity
$\forall$	For all

1 Introduction

1.1 Background

In the middle ages, if someone had imagined and proposed an idea that people could speak to each other from a long distance via a small black-box, it would have been certainly unbelievable. Started by imagination, excited by strong passion and accomplished by keen working of many scientists, the wireless communication has been realized. Nowadays, it has become an important demand of human being.

Great attention has been addressed to increase the quality of wireless communication. One of the most interesting issues is how to increase the data rate which is the amount of the information which can be transmitted/received during a specific time interval. According to the Shannon theory, the channel capacity can be increased by increasing the bandwidth. Ultra-Wide Band (UWB) communication which provides very large bandwidth then was proposed as a strong candidate for the high data rate communication. UWB radio is a fast emerging technology with unique attractive features inviting major advances not only in wireless communications but also in networking, radar, imaging, positioning systems. In addition to promising very high speed communication, it is also very attractive to be implemented as localization system at centimeter-level accuracy, high-resolution ground-penetrating radar, through-wall imaging, precision navigation and asset tracking [1].

UWB terminology in fact was born when the first wireless experiment was developed by Heinrich Rudolph Hertz in Karlsruhe Germany by 1886, when he did a spark gap experiment to investigate the electromagnetic wave propagation. This experiment pioneered radio technology and Hertz became the father of radio [2]. His experiment lead to a base-band communication by means of which the communication was established without carrier and the half-wavelength dipole that was utilized as the antenna was denoted as the first UWB antenna. Some of the first UWB antennas however have been disclosed since the narrowband communication became popular. Oliver Lodge who pioneered the narrow band communication introduced the concept of syntony where the transmitter and the receiver should be tuned to the same frequency so as to maximize the received signal. The renewed interest in wideband antennas for commercial application was started again with the advent of television technology where the interest in antennas that could handle wider bandwidth became a fact. This lead to the rediscovery of UWB antennas, for example: Biconical antenna and monopole antenna by Carter in 1939, spherical dipole by Schelkunof in 1940 and omni-directional coaxial horn by Brilloin in 1948 [3].

In 2002, the Federal Communications Commission (FCC) released the free license for UWB communication from 3.1-10.6 GHz which allowed very low radiated power -43 dBm/MHz that can provide high-rate data transmission above 110 MB/s over a short range (10-15 m). The regulatory limit of radiated power is defined as effective isotropic radiated power (EIRP), given as:

$$EIRP\,(f) = P_{\mathrm{TX}}(f)G_{\mathrm{TX}}(f) \tag{1.1.1}$$

where G_{TX} is the peak gain of the antenna in any orientation and P_{TX} is the transmitted power. Therefore, the design aim in UWB systems is to keep the value of $P_{\mathrm{TX}}(f)G_{\mathrm{TX}}(f)$ to conform to the FCC mask [4]. The 7.5 GHz free license bandwidth has drawn a great interest for commercial purposes, specially in terms of short distance communications that brought the UWB communication to be widely investigated in the last decade. However, further investigation is necessary to manage the radiated power efficiently due to the low power level requirement. Regarding to the antenna aspect, one approach to improve the link budget of such a short range communication could be to focus the radiation towards certain direction using an array antenna. A problem associated with an array antenna is that the beam width decreases with increasing frequency (and gain and EIRP increases and may violate the FCC mask) which could be solved by an array design providing a frequency invariant antenna pattern.

1.2 State of the art of UWB antenna research

Since the FCC released the free license regulation of the UWB band, the research of the UWB communication has rapidly grown and has been continuously increasing in the last decade with the focus on impulse based systems. Microwave devices required for supporting the large band characteristic then have been widely investigated. With respect to the function, UWB antenna design requires not only broadband characteristics but also low pulse distortion characteristics since the antenna will be utilized for impulse-based communication.

To investigate UWB antennas for base band technology, both time domain and frequency domain representations are important to describe the performance of the antenna. The classical representation of the antenna's performance in frequency domain has been generally used to characterize narrowband antennas. The time domain representation further was explored to complete the description of the impulse-based UWB antenna. Some terms to illustrate the electrical properties of the broadband antenna in time domain are: impulse response, ringing time and group delay which have been derived in [5]. It has been found that some of the UWB antennas provide large bandwidth and offer stable radiation pattern across the frequency as well, however the antennas are not appropriate to be used for base-band communication due to the dispersive characteristic: The Log periodic antenna is an example of a dispersive antenna which exhibits a ringing time which is much longer than in other UWB antennas [6] but, on the other hand, the antenna is able to cover a broadband frequency range.

The research of UWB antennas has concentrated on and has produced significant progress in planar antenna design due to the attractive merits such as low cost and compact structure. One of the most widely investigated UWB antennas is the printed monopole antenna which covers more than 100 % bandwidth as well as being realized in small size. Moreover, a further investigation has demonstrated 40 % reduction in size of the printed monopole antenna [7] by exploiting its structural symmetry but, on the other hand, still keeping the bandwidth the same as the original geometry. The printed monopole antenna has been realized in several types of radiators: circular, ellipse, triangular, rectangular. It provides near omni-directional pattern in the H-plane. A modification of the printed circular monopole antenna has been explored in this work in an effort to achieve a better suitable directional pattern.

One advanced goal for the UWB antenna is a frequency invariant far-field beam pattern of the antenna array. As the theory of antenna arrays shows, the radiation pattern is a function of the frequency. Therefore, in the range of the UWB frequency, the Half-Power Beamwidth (HPBW) varies dramatically, thus the spatial distribution of the radiated power over the frequency is not constant. Some attempts have been published with the issue of performing frequency invariant far-field beam patterns. One example is a rectangular array of monopole antennas with integrated attenuators as the weighting factors applied to each element working across the 1.9-2.5 GHz frequency range [8]. Another example is a circular array of mono cone antennas which are fed by FIR filters for frequencies of 1.5-2 GHz [9]. A Rotman-Lens has been introduced as the feeding network of a linear array of vertical Vivaldi antennas to achieve frequency invariant beamforming [10].

1.3 The contribution of the dissertation

In this contribution, we concentrate on the investigation of the UWB impulse radio system regarding to the antenna aspect, in particular the UWB planar antenna. A compact UWB antenna in planar technology is very attractive to be integrated in wireless communication systems as can be seen from a large number of publications related to this issue. However, an UWB planar antenna array has not been widely explored yet. The implementation of a UWB antenna array is one strategy to control the spatial distribution of radiated power that could be offered as one solution to use the free license bandwidth regulated by FCC efficiently. The other proposed strategies for controlling the radiated power are designing a directive single radiator and finally, applying the concept of the frequency invariant far-field beam pattern. Those three strategies are included in this work. Moreover, a practical planar UWB antenna array has been developed and fabricated for the band of interest of 3.1-10.6 GHz. The printed circular monopole antenna was explored as the radiator for the array and then modified as a directive UWB antenna. Finally, an advanced beamforming concept which uses a set of passive low pass filters in the feed network in order to achieve frequency invariant far-field beam pattern is presented. Such a concept is essentially adopted from the broadband sensor's theory for acoustic purpose and we review the theory, and as far as the author knows for the first time implement it in the

microwave frame. A prototype of the UWB antenna array was fabricated in order to prove the concept. The simulation and measurement show that the concept can be successfully used for UWB beamforming and the beamwidth of far-field radiation pattern can be kept constant [11].

1.4 Organization of the dissertation

The electrical properties of antennas both in frequency domain and time domain are discussed in chapter 2. Moreover, a brief theory of a linear array antenna is presented as well. In chapter 3, the UWB printed antenna is initially characterized, namely the printed circular monopole antenna. The original model of PCMA is modified as a directive, so called U-shaped PCMA. In chapter 4, a four-element U-shaped PCMA linear array antenna is designed. Furthermore, an UWB T-junction power divider for the feeding network of a four-element UWB directive printed circular monopole antenna is demonstrated. The measurements of the fabricated antenna are shown in this chapter as well.

In chapter 5, the strategy of frequency invariant far-field beam pattern from a linear array UWB antenna is discussed. This strategy is based on designing a set of low pass filters as part of the feeding network of the linear UWB antenna array and the general beam forming concept using a set of low pass filters is examined. As the next step, eight printed circular monopole antenna elements are implemented as the radiators of the UWB antenna linear array where the strategy of frequency invariant far-field beam pattern is applied in the design. It is performed by feeding the antenna array by a three-stage broadband Wilkinson power divider network with a set of low pass filters inserted between the antenna elements and the power dividers. In the last chapter, the fabricated printed circular monopole antenna array with frequency invariant far-field beam pattern is measured to prove the concept and to validate the simulation result.

2 Fundamental Antenna Theory in Frequency Domain and Time Domain

This chapter is dedicated to the antenna's terminologies which are reviewed to introduce several parameters for the discussion in next chapters. In general, the antenna parameters can be categorized based on frequency domain and time domain. Some general antenna parameters in the frequency domain are [12]: directivity, gain, efficiency and input impedance, which have been widely utilized to describe the antenna's characteristic in narrow frequency bands. To describe the characteristic of UWB antennas for impulse radio system purposes, the UWB antenna has been modeled as a linear time invariant (LTI) system which yields two terminologies, namely the antenna transfer function and the antenna impulse response. The antenna impulse response is the key to formulate the antenna parameters in time domain. Some antenna parameters in the time domain have been defined based on the performance of the impulse response in [5] which will be reviewed in this chapter. In addition, a brief theory of antenna arrays is presented which is concentrated on the theory of linear arrays. Furthermore, the concept of beam scanning of a linear array antenna is discussed as well. To introduce the concept of beam scanning, the theories of phase shifter beam scanning and of time delay beam scanning are given. Finally, the beam scanning concept in the time domain will close this chapter.

2.1 The Fundamental Antenna Parameters

2.1.1 Directivity and gain

Two fundamental antenna parameters in the antenna theory are directivity and gain which describe the ability of an antenna to focus the radiated power. The directivity is defined as the ratio of the radiation intensity at a given direction from the antenna to the averaged radiation intensity over all directions at a specific frequency [12], formulated as:

$$D(f, \theta, \psi) = \frac{4\pi U(f, \theta, \psi)}{P_{\text{rad}}} \tag{2.1.1}$$

where $D(f, \theta, \psi)$ represents directivity for frequency f, at an azimuth and an elevation angle ψ and θ; $U(f, \theta, \psi)$ represents the radiation intensity and P_{rad} denotes the total radiated power overall all directions as illustrated in the polar coordinate system in Fig. 2.1. The gain definition is close to the directivity definition and is defined as the ratio of
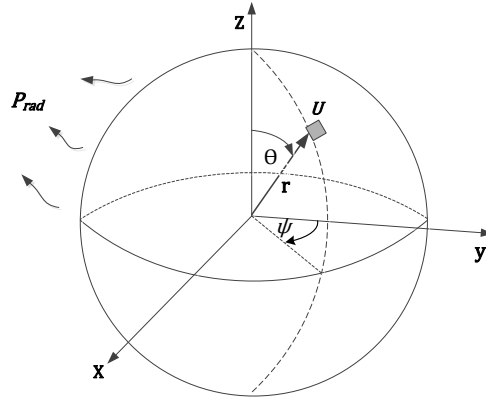
Figure 2.1: Polar coordinate system

the radiation intensity at a given direction to the average intensity created by isotropic radiation of the power accepted by the antenna, written as

$$G(f, \theta, \psi) = \frac{4\pi U(f, \theta, \psi)}{P_{\text{in}}} \tag{2.1.2}$$

where $G(f, \theta, \psi)$ represents the gain, P_{in} represents the power accepted by the antenna. The terminologies of the gain and the directivity are generally meaning the maximum gain G and the maximum directivity D over all directions. The gain definition in equation (2.1.2) is generally known as the *IEEE gain* where such a definition doesn't include the mismatch of the antennas input impedance (mismatch losses). Another definition of gain is defined as the absolute gain G_{abs} which is considering the mismatch losses. The relation between the IEEE gain and the absolute gain is expressed as

$$G_{\text{abs}} = \left(1 - |S_{11}|^2\right)G \tag{2.1.3}$$

where G_{abs} and S_{11} represent the absolute gain and the reflection coefficient of the antenna respectively. With respect to the antenna simulation, the above definitions: directivity, IEEE gain, and absolute gain are generally used in a commercial full-wave simulator where they allow to observe the losses dissipated either in the antenna or in the feeding network. The power losses in the antenna can be determined based on the power distribution in the antenna system, as described in Fig. 2.2. It can be seen in Fig. 2.2 that a fraction of the incident power P_{inc} is reflected as the reflected power P_{refl} due to the mismatch at the excitation (port) of the antenna. The other fraction is accepted by the antenna as the accepted power P_{in}. On the other hand, a part of the accepted power is dissipated by conductors and dielectrics as the conductivity and the dielectric losses which is denoted as P_{loss}. The rest of the accepted power is radiated to the free space as the radiated power P_{rad}. Hence, according to the schematic in Fig. 2.2, the relation between the power losses and the power distribution in the antenna system can be formulated as

$$P_{\text{inc}} = P_{\text{refl}} + P_{\text{loss}} + P_{\text{rad}} \tag{2.1.4}$$
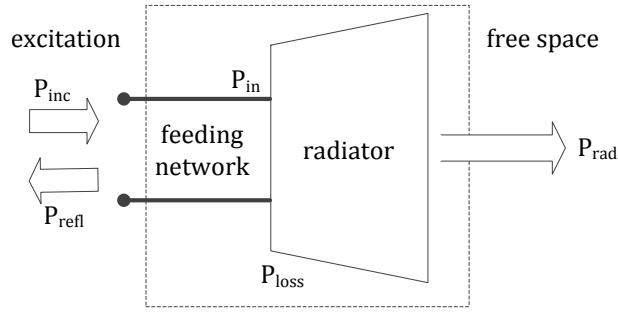
Figure 2.2: Schematic of the power distribution in the antenna system

$$P_{\text{in}} = P_{\text{loss}} + P_{\text{rad}} \tag{2.1.5}$$

The radiation efficiency and the antenna efficiency are the quality measures of the antenna which can be formulated based on the power distribution in the antenna system. The radiation efficiency η is defined as the ratio of the radiated power to the accepted power

$$\eta = \frac{P_{\text{rad}}}{P_{\text{in}}} \tag{2.1.6}$$

whereas the antenna efficiency η_a is defined as the ratio of the radiated power to the incident power

$$\eta_a = \frac{P_{\text{rad}}}{P_{\text{inc}}} \tag{2.1.7}$$

If the antenna input impedance is perfectly matched to the generator input impedance, the antenna efficiency is equal to the radiation efficiency. According to equations (2.1.1), (2.1.2) and (2.1.6) the radiation efficiency can be expressed as the ratio of the gain G and the directivity D

$$\eta = \frac{G}{D} \tag{2.1.8}$$

As can be seen in the equations (2.1.4) and (2.1.5), the material loss is a significant variable which degrades the radiation efficiency and, on the other hand, its quantity is complicated to be obtained analytically. However, the conduction and the dielectric losses of the antenna can be assessed practically by calculating the directivity and the gain in a full-wave simulator. The losses in dB denoted as $L(dB)$, can be assessed as the difference of the directivity and the gain

$$L(dB) = D(dB) - G(dB) \tag{2.1.9}$$

Another type of losses in the antenna system could be the losses due to spurious radiation of the feeding network which yields antenna pattern degradation [13], in particular for a large array antenna. Since the power of such a radiation is relatively small compared to the total radiated power, this effect could be neglected.

2.1.2 Antenna equivalent electric circuit

A simple antenna as a transmitter can be modeled as an antenna equivalent circuit [14] as illustrated in Fig. 2.3 where
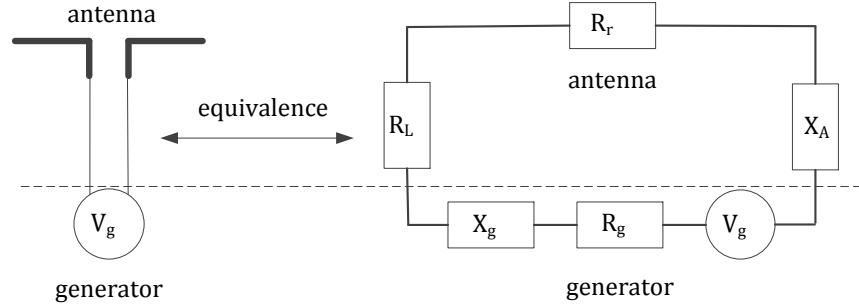
Figure 2.3: Antenna equivalent circuit of the transmitting antenna [14]

R_r = radiation resistance of the antenna
R_g = resistance of generator impedance
R_L = loss resistance of the antenna
X_g = reactance of generator impedance
X_A = antenna reactance
V_g = peak generator voltage

As can be seen in Fig. 2.3, the dissipation losses in the antenna are modeled as the loss resistance R_L and the radiated power is modeled as the radiation resistance R_r. Regarding to the efficiency, the radiation efficiency η can be expressed as the function of the radiation resistance and the loss resistance as given in equation (2.1.10). A simple illustration shows that the radiation efficiency strongly depends on the losses due to the material.

$$\eta = \frac{R_\mathrm{r}}{R_\mathrm{L} + R_\mathrm{r}} \tag{2.1.10}$$

As shown in the equivalent circuit, the antenna is excited by the source with the peak voltage V_g and the generator impedance is denoted as Z_g where

$$Z_\mathrm{g} = R_\mathrm{g} + jX_\mathrm{g} \tag{2.1.11}$$

A fraction of the input power is delivered to the antenna reactance X_A which is not radiated to free space, yet it is stored as reactive power. The maximum power transferred to the antenna at frequency f is obtained if the antenna input impedance is equal to the complex conjugate of the generator impedance which is expressed as *perfect impedance matching* condition, given as

$$X_\mathrm{g} = -X_\mathrm{A}$$
$$R_\mathrm{g} = R_\mathrm{L} + R_\mathrm{r} \tag{2.1.12}$$

The impedance matching could be achieved by tuning the value of X_g. This could be implemented by inserting *a matching circuit* between the antenna and a generator. In the planar technology, the matching circuit has been widely implemented as serial/parallel microstrip-stubs which will be discussed in chapter 3.

2.2 Antenna as Linear Time Invariant (LTI) System

2.2.1 Antenna transfer function

In the investigation of a narrowband antenna, the characteristics of the antenna are represented based on the centre frequency, for example the gain/directivity of the antenna is represented as the gain/directivity at the center frequency. In case of a wideband antenna, the parameters are strongly frequency dependent; the gain/directivity could vary across the frequency band. Therefore, the characteristics of a wideband antenna have to be represented for the whole frequency band. One approach to characterize a UWB antenna has been to model the antenna as a Linear Time Invariant (LTI) system. The LTI system is defined as a system which exhibits the superposition property in its input-output relationship and this doesn't change with time [15].

As the rule of thumb, the characteristics of the LTI system are described as the transfer function $H(f)$ in the frequency domain and as impulse response $h(t)$ in the time domain. Both representations can be transformed from one to another by applying Fourier transform $\mathcal{F}$ or Inverse Fourier transform $\mathcal{F}^{-1}$ as illustrated in Fig. 2.4. In the frequency
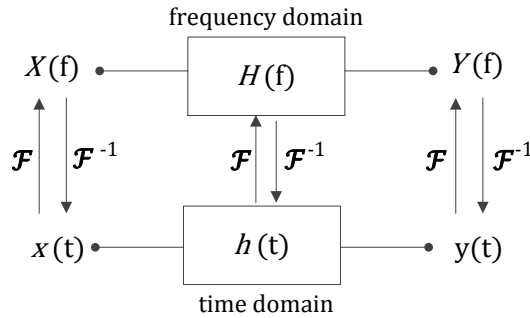
Figure 2.4: Fourier transform/inverse Fourier transform of an LTI system

domain, the output of the system $Y(f)$ is represented as the multiplication of the input signal is represented as the multiplication of the input signal $X(f)$ with the transfer function $H(f)$ and, on the other hand, in the time domain the output signal $y(t)$ is represented as the convolution of the input signal $x(t)$ with the impulse response $h(t)$, written as

$$Y(f) = X(f) \cdot H(f)$$
$$y(t) = x(t) * h(t)$$

(2.2.1)

The antenna as a LTI system has been derived based on network analysis in [5], [16]. The LTI systems of the transmitting and receiving antenna can be utilized to describe the communication link between the antennas which is summarized as following.

Fig. 2.5 shows a communication system with two antennas where the transmitting antenna and the receiving antenna are separated by a distance r. It illustrates that the transmitting
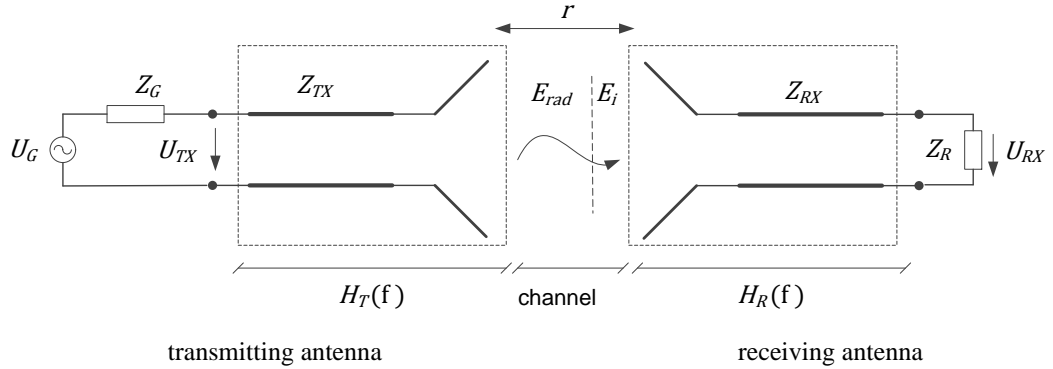
Figure 2.5: Communication system of two antennas

antenna radiates the electric field $\boldsymbol{E}_{\mathrm{rad}}(f, \theta, \psi)$ at a distance r from the antenna. The characteristic impedance of the antenna is represented as Z_{TX}, the antenna is excited by the generator at frequency f with voltage $U_{\mathrm{G}}(f)$ whereas the generator input impedance is represented as $Z_{\mathrm{G}}(f)$. Furthermore, the antenna is modeled as the LTI system with the transfer function $\boldsymbol{H}_{\mathrm{T}}(f)$. According to this model, the radiated electric field at a distance r is given as

$$\frac{\boldsymbol{E}_{\mathrm{rad}}(f, \theta, \psi)}{\sqrt{Z_{\mathrm{F}}}} = \frac{1}{2\pi rc}e^{-j2\pi fr/c}j\omega \boldsymbol{H}_{\mathrm{T}}(f, \theta, \psi)\frac{U_{\mathrm{TX}}(f)}{\sqrt{Z_{\mathrm{TX}}}} \tag{2.2.2}$$

where U_{TX} represents the transmitted voltage, c is the speed of light, ω is the angular frequency, Z_{TX} and Z_{F} represent the characteristic impedance of the antenna and the free-space impedance respectively. $\boldsymbol{E}_{\mathrm{rad}}$ and $\mathbf{H}_{\mathrm{T}}$, represented as bold symbols, are vectors related to the orthogonal polarization basis. At the receiving antenna, the radiated electric field is received as the electric field $\boldsymbol{E}_{\mathrm{i}}(f, \theta, \psi)$. Since the receiving antenna is defined as a LTI system with transfer function $\boldsymbol{H}_{\mathrm{R}}(f)$, the received voltage U_{RX} is formulated as

$$\frac{U_{\mathrm{RX}}(f)}{\sqrt{Z_{\mathrm{RX}}}} = \boldsymbol{H}_{\mathrm{R}}(f, \theta, \psi)\frac{\boldsymbol{E}_{\mathrm{i}}(f, \theta, \psi)}{\sqrt{Z_{\mathrm{F}}}} \tag{2.2.3}$$

where Z_{RX} represents the input impedance of the receiving antenna.

In order to describe the communication link of two antennas, the transmitted electric field at a distance r is assumed equal to the received electric field. Hence, according to equations (2.2.2) and (2.2.3) the communication link is derived as

$$\frac{U_{\mathrm{RX}}(f)}{\sqrt{Z_{\mathrm{RX}}}} = \boldsymbol{H}_{\mathrm{T}}(f, \theta, \psi)\,\boldsymbol{H}_{\mathrm{R}}(f, \theta, \psi)\frac{e^{-j2\pi fr/c}}{2\pi rc}j\omega\frac{U_{\mathrm{TX}}(f)}{\sqrt{Z_{\mathrm{TX}}}} \tag{2.2.4}$$

As can be seen in the equations (2.2.2) and (2.2.4), the channel is described as a linear channel with free space propagation. However, in the practical design of UWB communication systems, the characteristic of the channel exhibits multipath propagation and reflections from objects. Therefore, the general equation of the communication link is given as

$$\frac{U_{\mathrm{RX}}(f)}{\sqrt{Z_{\mathrm{RX}}}} = \boldsymbol{H}_{\mathrm{T}}(f, \theta, \psi)\, \boldsymbol{H}_{\mathrm{C}}(f, \theta, \psi)\, \boldsymbol{H}_{\mathrm{R}}(f, \theta, \psi)\, j\omega \frac{U_{\mathrm{TX}}(f)}{\sqrt{Z_{\mathrm{TX}}}} \qquad (2.2.5)$$

where $\boldsymbol{H}_{\mathrm{C}}$ represents the transfer function of the channel. In this work, the contribution of the experimental channel is not considered. However, the investigation of the experimental channel associated with UWB antennas has been presented in [17],[18].

The antenna transfer function can be extracted from the S-parameter transmission S_{21} of the two antennas. It can be derived by modeling the communication system as a two port network as described in Fig. 2.6 where the relations of the wave voltages $U_{\mathrm{TX+}}$, $U_{\mathrm{TX\text{-}}}$,
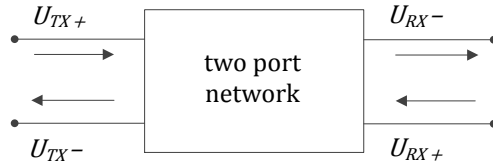
Figure 2.6: Schematic of two port network

$U_{\mathrm{RX+}}$, $U_{\mathrm{RX\text{-}}}$ with the total voltages U_{TX}, U_{RX} are given as

$$\begin{aligned} U_{\mathrm{TX}} &= U_{\mathrm{TX+}} + U_{\mathrm{TX\text{-}}} \\ U_{\mathrm{RX}} &= U_{\mathrm{RX+}} + U_{\mathrm{RX\text{-}}} \end{aligned} \qquad (2.2.6)$$

According to the two port network configuration, the transmission S-parameter is written as

$$S_{21} = \frac{U_{\mathrm{RX\text{-}}}}{U_{\mathrm{TX+}}}. \qquad (2.2.7)$$

Hence, according to equations (2.2.4), (2.2.6) and (2.2.7), the transmission S-parameter of two antennas at a distance r is formulated as

$$\boldsymbol{S}_{21}(f, \theta, \psi) = \boldsymbol{H}_{\mathrm{T}}(f, \theta, \psi)\, \frac{e^{-j2\pi f r/c}}{2\pi r c}\, j\omega\, \boldsymbol{H}_{\mathrm{R}}(f, \theta, \psi)\, \frac{\sqrt{Z_{RX}}}{\sqrt{Z_{TX}}} \qquad (2.2.8)$$

Finally, by making use of two identical antennas with the same polarization in equation (2.2.8) and according to the principle of reciprocity where $\boldsymbol{H}_{\mathrm{T}} = \boldsymbol{H}_{\mathrm{R}}$, one obtains

$$\boldsymbol{H}_{\mathrm{T}}(f, \theta, \psi) = \sqrt{\frac{rc}{jf}}\, \boldsymbol{S}_{21}(f)\, e^{j2\pi f r/c} \qquad (2.2.9)$$

The data of $\boldsymbol{S}_{21}(f, \theta, \psi)$ can be obtained based on a simulation in a full-wave simulator or from measurement. With respect to the measurement, delay and dissipation due to, e.g., a cable connections should be taken into account as an additional transfer function namely the calibration transfer function H_{sys}, which gives contribution in equation (2.2.8) as

$$\boldsymbol{S}_{21}(f, \theta, \psi) = \boldsymbol{H}_{\mathrm{T}}(f, \theta, \psi) \frac{e^{-j2\pi fr/c}}{2\pi rc} j\omega \boldsymbol{H}_{\mathrm{R}}(f, \theta, \psi) H_{\mathrm{sys}} \frac{\sqrt{Z_{RX}}}{\sqrt{Z_{TX}}} \tag{2.2.10}$$

The calibration transfer function can be calculated separately by measuring the transmission S-parameter of the two-ports separated at a distance r without the transmitting/receiving antenna where the connection between two port is replaced by cable [19]. Then, one obtains the transfer function of the antenna under test (AUT) by extracting the values of S_{21} from a network analyzer. If the measurement utilizes two different antennas, namely the reference (standard) antenna as the transmitting antenna and AUT as the receiving antenna, the transfer function of the reference antenna can be observed separately. As the next step, the transfer function of the AUT can be extracted base on equation (2.2.10).

It would be practicable if the transfer function could be extracted from the pattern measured in the *anechoic chamber* since the transfer function for all directions of one observed cut-plane can be obtained at the same measurement. The radiation pattern is measured to obtain the quantity of the gain pattern at frequency f over a particular cut plane and the relation between the absolute gain and the transfer function is given as [5]

$$G_{\mathrm{abs}}(f, \theta, \psi) = \frac{\omega^2}{\pi c^2} |\boldsymbol{H}(f, \theta, \psi)|^2 \tag{2.2.11}$$

Hence, by measuring the gain across the frequency, the antenna transfer function could be calculated.

Another antenna property in the frequency domain is group delay $\tau(f)$ which shows the linear phase-response of the antenna transfer function across the frequency. The relation of the group delay to the antenna transfer function is represented in the equations (2.2.12)

$$\boldsymbol{H}(f) = |\boldsymbol{H}(f)| e^{j\varphi(f)}$$
$$\tau(f) = -\frac{1}{2\pi} \frac{d\varphi(f)}{df} \tag{2.2.12}$$

where $|\boldsymbol{H}(f)|$ is the magnitude of the transfer function in meter and φ represents the phase in radians. The group delay response over frequency will characterize an UWB antenna. The UWB antenna would raise a minimum distortion to the incoming signal if the group delay were flat over frequency, otherwise it would raise strong distortion if the response were fluctuating.

2.2.2 Antenna impulse response

At the transmitting antenna, the radiated electric field in the time domain $\mathbf{e}_{\mathrm{rad}}(t,\theta,\psi)$ is obtained by applying the Inverse Fourier transform to equation (2.2.2), written as

$$\frac{\boldsymbol{e}_{\mathrm{rad}}(t,\theta,\psi)}{\sqrt{Z_{\mathrm{F}}}} = \frac{1}{2\pi rc}\delta\left(t-\frac{r}{c}\right)*\boldsymbol{h}_{\mathrm{T}}(t,\theta,\psi)*\frac{\partial}{\partial t}\frac{u_{\mathrm{TX}}(t)}{\sqrt{Z_{\mathrm{TX}}}} \tag{2.2.13}$$

where $u_{\mathrm{TX}}(t)$ and $\boldsymbol{h}_{\mathrm{T}}$ represent the transmitted voltage and the transmitting antenna impulse response. On the other hand, the received voltage $u_{\mathrm{RX}}(t)$ at the receiving antenna is obtained by employing the Inverse Fourier transform to equation (2.2.3), hence

$$\frac{u_{\mathrm{RX}}(t)}{\sqrt{Z_{\mathrm{RX}}}} = \boldsymbol{h}_{\mathrm{R}}(t,\theta,\psi)*\frac{\boldsymbol{e}_{\mathrm{i}}(t,\theta,\psi)}{\sqrt{Z_{\mathrm{F}}}} \tag{2.2.14}$$

where $\boldsymbol{h}_{R}(t,\theta,\psi)$ and $\boldsymbol{e}_{\mathrm{i}}(t,\theta,\psi)$ represent the receiving antenna impulse response and the received electric field in the time domain. By making use of equations (2.2.13) and (2.2.14), the communication link of two antennas in the time domain is derived as

$$\frac{u_{\mathrm{RX}}(t)}{\sqrt{Z_{\mathrm{RX}}}} = \frac{1}{2\pi rc}\delta\left(t-\frac{r}{c}\right)*\boldsymbol{h}_{\mathrm{T}}(t,\theta,\psi)*\boldsymbol{h}_{\mathrm{R}}(t,\theta,\psi)*\frac{\partial}{\partial t}\frac{u_{\mathrm{TX}}(t)}{\sqrt{Z_{\mathrm{TX}}}} \tag{2.2.15}$$

In addition, the pulse at the receiving antenna is corresponding to the time derivative of the pulse of the transmitting antenna which gives insight that the UWB antenna as a transmitter behaves as a time derivative component. The incoming pulse at the transmitting antenna is derivated before it propagates into the free space. However, it is only found at the transmitting antenna since the received pulse is not derivated at the receiving antenna.

As mentioned before, the impulse response can be obtained from the transfer function of the corresponding simulation/measurement. Since the simulation/measurement data are discrete data, the *Inverse Discrete Fourier Transform* (IDFT) will be applied to the transfer function, which is formulated as

$$\boldsymbol{h}^{+}(k\Delta t) = \frac{1}{N\Delta t}\sum_{n=0}^{N-1}\boldsymbol{H}^{+}(n\Delta f)\,e^{j\frac{2\pi}{N}kn} \tag{2.2.16}$$

where Δt and Δf denote the time resolution and the frequency resolution respectively, k and n are integer numbers, whereas N is the number of the sampling data. In addition, $\boldsymbol{H}^{+}(n\Delta f)$ represents the envelope of complex one-sided transfer function at frequency $f = n\Delta f$ where the relation with the transfer function $\boldsymbol{H}$ is given as [20]

$$\boldsymbol{H}^{+}(f) = \begin{cases} 2\boldsymbol{H}(f) & \text{for } f > 0 \\ \boldsymbol{H}(f) & \text{for } f = 0 \\ 0 & \text{for } f < 0 \end{cases} \tag{2.2.17}$$

Furthermore, $h^{+}(k\Delta t)$ represents the complex impulse response at time $t = k\Delta t$ for a given polarization

$$h^{+}(k\Delta t) = h(k\Delta t) + j\mathcal{H}\{h(k\Delta t)\} \tag{2.2.18}$$

where $\mathcal{H}$ denotes the *Hilbert transform* notation and $h(k\Delta t)$ is the real part of the complex impulse response. Hence, the impulse response is obtained as

$$h(k\Delta t) = \Re\left\{h^+(k\Delta t)\right\} \tag{2.2.19}$$

whereas the absolute value of the complex impulse response $\left|h^+(k\Delta t)\right|$ represents the envelope of the impulse response.

In order to increase the resolution of the calculated impulse response, *zero padding* is applied in the IDFT. *Zero padding* is realized by inserting zero numbers in the sampling data [21].

The antenna parameters in the time domain are defined based on the behavior of the impulse response, namely: peak value, the width of full pulse at half maximum (FWHM) and ringing time.

The peak value
The peak value $p(t)$ is defined as the maximum value of the envelope impulse response $\left|h^+(k\Delta t)\right|$, written as

$$p(t) = max_t\left|h^+(t)\right| \tag{2.2.20}$$

where $p(t)$ is defined in m/ns

The width of full pulse at half maximum (FWHM)
τ_{FHWM} mathematically is defined as the width of the envelope of the impulse response at the half of maximum peak value, given as

$$\tau_{\text{FHWM}} = t_1\big|_{\left|h^+(t_1)\right|=p/2} - t_2\big|_{\left|h^+(t_2)\right|=p/2} \tag{2.2.21}$$

The ringing time
Ringing is the signal oscillation after the signal achieved the maximum peak. The ringing time τ_{r} is defined as the duration of the signal from the maximum peak p until the partial value α of the maximum peak

$$\tau_{\text{r}} = t_1\big|_{h^+(t_1)=\alpha p} - t_2\big|_{t_2<t_1 \,\wedge\, h^+(t_2)=p} \tag{2.2.22}$$

A well performing UWB antenna is expected to have short ringing time. The duration of the ringing time depends on the geometry of the antenna. It may be complicated to suppress the ringing by modifying the antenna structure. However, it may be eliminated by absorbing materials [6].

2.3 Linear Array Antenna

An array antenna is an arrangement of radiator elements with a particular grid configuration where the main goal of constructing the array may be to realize high gain pattern with particular beam shaping. A radiator element is a single antenna; it could be a simple antenna like a patch, a dipole or even a more complex antenna like a parabolic antenna. In general, the array antenna consists of identical elements whereas the construction of the configuration grids could be linear, planar or circular [12] as described in Fig. 2.7(a), 2.7(b) and 2.7(c). Another arrangement is widely known as conformal array where the elements are placed to conform to a surface of a particular object. Fig. 2.7(d) shows an example of the grid configuration of the conformal array where the surface could be arbitrary and non-planar. Therefore, modeling of such an array leads to a more sophisticated mathematical framework than modeling the conventional arrays. Reference [22] provides the mathematical framework of modeling the conformal array antenna for further investigation.

(a) Linear array   (b) Circular array

(c) Planar array   (d) Example of a conformal array
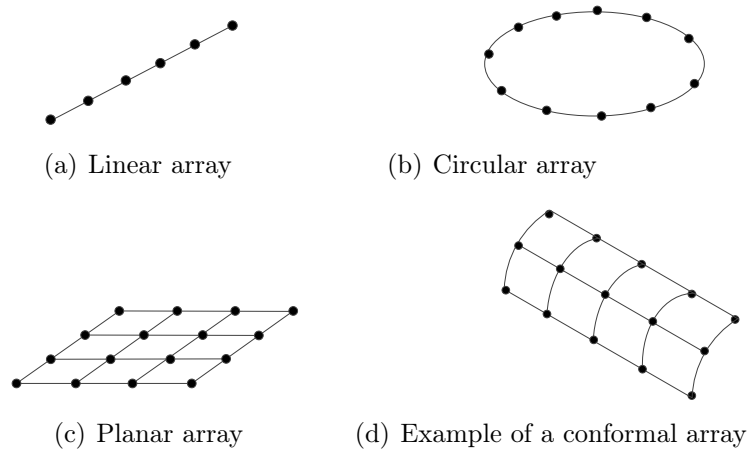
Figure 2.7: Array structure

2.3.1 Analytical expression of a linear array antenna

A linear array antenna is described as an array antenna where the elements are located along a line. Consider a linear array where the elements are located arbitrary in the coordinate system as described in Fig. 2.8. The field of the ith element at the distant point is given as [23]

$$E_i\left(\theta, \varphi\right) = f\left(\theta, \varphi\right) I_i exp\left[j\left(kr_i \cos\psi_i + \alpha_i\right)\right] \tag{2.3.1}$$

where $f\left(\theta, \varphi\right)$ is the far-field function of the corresponding element which is also represented as the *isolated pattern*. The amplitude and the phase excitation (weighting
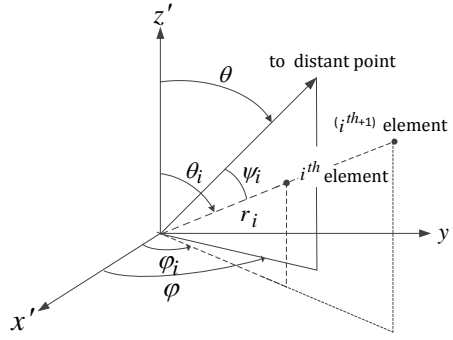
Figure 2.8: Representation of a linear array antenna in the coordinate system [23]

function) of the element is denoted as I_i and α_i respectively, whereas $k = \frac{2\pi}{\lambda}$ (λ represents free-space wavelength). In addition, ψ_i is derived as

$$\cos\psi_i = \cos\theta\cos\theta_i + \sin\theta\sin\theta_i\cos(\varphi - \varphi_i) \tag{2.3.2}$$

If the arrays consists of n identical elements and oriented in the z' axis, hence
$\theta_i = 0$, $r_i = z_i'$, $i = 1, 2, 3...., n$
The total field $E(\theta, \varphi)$ is the contribution of all elements

$$E(\theta, \varphi) = \sum_{i=1}^{n} E_i(\theta, \varphi)$$

$$= f(\theta, \varphi) \sum_{i=1}^{n} I_i exp\left[j\left(kz_i'\cos\theta + \alpha_i\right)\right] \tag{2.3.3}$$

The summing contribution in equation (2.3.3) is represented as the *array factor AF* which represents the contribution of the element configuration to the pattern, thus it can be written as

$$E(\theta, \varphi) = f(\theta, \varphi) AF \tag{2.3.4}$$

where

$$AF = \sum_{i=1}^{n} I_i exp\left[j\left(kz_i'\cos\theta + \alpha_i\right)\right] \tag{2.3.5}$$

The mathematical representation in equation (2.3.4) is widely known as pattern multiplication principle where the antenna pattern can be represented as the multiplication of the element pattern and the array factor. This mathematical representation is very powerful and widely used to describe the radiation pattern of antenna arrays. However, the *mutual coupling* between the elements is not considered in this formulation.

2.3.2 Mutual coupling

Although the array antenna consists of identical elements, the patterns of each element are not equal due to the phenomenon of the so called mutual coupling where the input impedance of each element is changed and the patterns are altered from the isolated one. Mutual coupling is described as the electromagnetic coupling in an element of an array which is stimulated by radiation or re-radiation from other radiators. Re-radiation is the scattered wave either from other elements or from other objects towards the active antenna. The radiated electromagnetic wave can stimulate current flowing in the other antennas. Moreover, the induced current will trigger the electromagnetic wave which is re-radiated to the active antenna, illustrated as label (1) in Fig. 2.9. The spurious electromagnetic coupling could be stimulated by scattering of another object as well, for example a finite conductive ground plane (chassis) closed to the antenna, which is illustrated as label (2) in Fig. 2.9. In this case, the incident wave is re-scattered to the free space and a part of it is re-scattered toward the active antenna which leads to the electromagnetic coupling. Therefore, the radiated field into the free space is the superposition of the
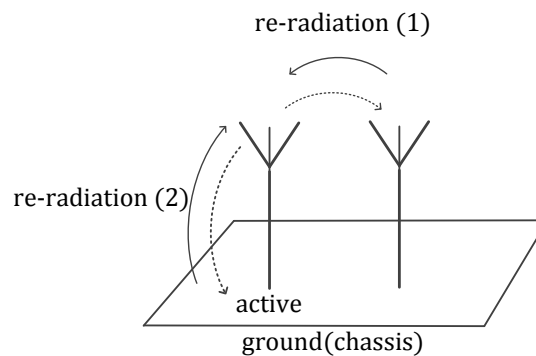
Figure 2.9: Electromagnetic coupling in antenna arrays

scattered radiation from the chassis and the radiation from the antenna. This phenomenon is very attractive and has been widely investigated in system applications, for example in the area of mobil-phone [24]. Furthermore, the effect of the chassis on the performance of a monopole array antenna has been investigated in [25] where the coupling from the chassis has been modeled as an equivalence circuit.

The definition of mutual coupling is more directed to the electromagnetic coupling between the antenna elements. Due to the mutual coupling, the input impedance of the active element is changed. Thus, the original input impedance is not appropriate to calculate the input impedance of the antenna arrays. Therefore, the *active impedance* [12] was defined as the impedance looking into a single element of an array with all other elements of the array excited. In terms of designing an array antenna, the active impedance is used as the reference impedance to optimize the reflection coefficient of the elements in the array antenna.

Moreover, the active impedance is also utilized to investigate the electronically beam-scanning antenna (phased array antenna). In the phased array antenna, the active impedance varies with the scanning angle. A phenomenon which is called *scan blindness* may occur in this antenna where the main beam is suppressed at a certain scanning angle because the value of the active impedance is altered dramatically at this angle. The phenomenon of scan blindness can be investigated by simulating the active impedance as shown in [26].

In addition, the *active element pattern* is defined as the radiation of a single element by considering the inter-element coupling (mutual coupling) [27]. The active element pattern strongly depends on the geometry of the element and the spacing between the elements. In numerical simulation, it can be generated by exciting the active element and simultaneously terminating the other elements with matched load. By using the active element pattern, the field of a linear array antenna is formulated as

$$E\left(\theta, \varphi\right) = \sum_{i=1}^{n} f_i\left(\theta, \varphi\right) I_i exp\left[j\left(kz_i^{'}\cos\theta + \alpha_i\right)\right] \tag{2.3.6}$$

where $f_i\left(\theta, \varphi\right)$ represents the active element pattern of the ith element.

2.3.3 Uniform linear array antenna
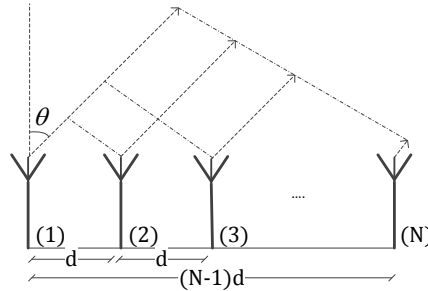
Figure 2.10: Uniform spacing linear array antenna

The terms of uniform linear array antenna here indicates an antenna array with N identical elements, distributed with equal spacing d and excited with the same amplitude I and the same phase α as described in Fig. 2.10, where the mutual coupling is not considered in this case. According to equation (2.3.3) and by taking the normal line as the reference angle, the total field of the uniform linear array antenna as depicted in Fig. 2.10 is obtained as

$$E\left(\theta, \varphi\right) = f\left(\theta, \varphi\right) I exp\left(j\alpha\right) \sum_{n=1}^{N} exp\left[j\left(kd\left(n-1\right)\sin\theta\right)\right] \tag{2.3.7}$$

As the first step to visualize the pattern, the isolated element pattern is assumed as an isotropic point source where the radiation is equally distributed over all directions. By

normalizing the amplitude of the point source, the normalized pattern of the array is written as

$$E_{norm}(\theta) = \frac{1}{N} \sum_{n=1}^{N} exp\left[j\left(kd\left(n-1\right)\sin\theta\right)\right] \tag{2.3.8}$$

Moreover, the pattern is generally expressed as the power pattern P in dB

$$P = 20log\left|E_{norm}(\theta)\right| \tag{2.3.9}$$
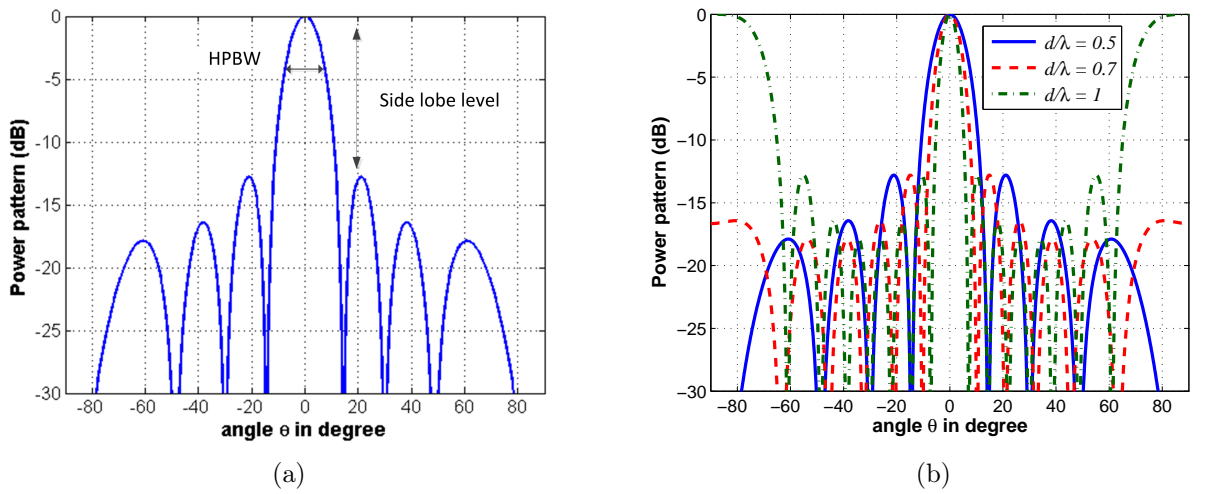
Figure 2.11: Pattern of 8-elements (a)at $d/\lambda = 0.5$ (b)with variation of d/λ

Fig. 2.11(a) shows the normalized pattern of an 8-element linear array antenna with spacing between the elements $d = 0.5\lambda$. It can be seen that the *Half Power Beamwidth* (HPBW) is approximately 12.8° and the first side lobe level is found at -13 dB below the main beam. As shown in Fig. 2.11(b), by reducing the ratio d/λ, the HPBW becomes larger. At the ratio $d/\lambda = 1$, two other beams raise at θ equal to -90° and 90° which are recognized as the *grating lobes* in the antenna terminology.

2.4 Beam Scanning Antenna

2.4.1 Phased array antenna

The beam scanning antenna is mostly used for radar applications. The beam can be scanned by physically moving the antenna through the desired azimuth and elevation angles which is called *mechanical beam scanning*. Another alternative to scan the beam

is by employing electronic beam scanning. This technique has the advantages of more flexible and remarkably faster beam scanning than mechanical. It can be realized by progressively shifting the phase from one to the other radiators which is widely known as *phased array antenna*. By considering equation (2.3.8) where the phase is progressively shifted, the normalized pattern of phased array antenna is written as

$$E_{norm}(\theta) = \frac{1}{N} \sum_{n=1}^{N} exp\left[j\left(kd\left(n-1\right)\sin\theta + \alpha_n\right)\right] \qquad (2.4.1)$$

In order to scan the beam to an oriented angle θ_0, the phase of the radiators is shifted progressively by factor $-kd\sin\theta_0$, hence

$$\alpha_n = -kd\left(n-1\right)\sin\theta_0 \qquad (2.4.2)$$

Fig. 2.12(a) shows the beam scanning of 8-isotropic radiators of the linear array antenna with ratio $d/\lambda = 0.5$, where the beam is scanned to scanning angles: 10°, 30° and 60°. As shown in Fig. 2.12(a), the performance of the pattern is deteriorated as the beam scanning increases. The grating lobe seems to raise at the scanning angle 60°. It is therefore one disadvantage of the electronic beam scanning compared to the mechanically beam scanning that the maximum range of the scanning angle is limited and the pattern is deteriorated as the scanning angle increases. The maximum grating lobe-free scanning angle θ_m of a uniform spacing linear array antenna with spacing d and for wavelength λ is given as

$$\frac{d}{\lambda} \leq \frac{1}{\left(1 + d\sin\theta_m\right)} \qquad (2.4.3)$$

In order to extend the range of the scanning angle, a combination of the mechanical and electronic beam steering can be realized.
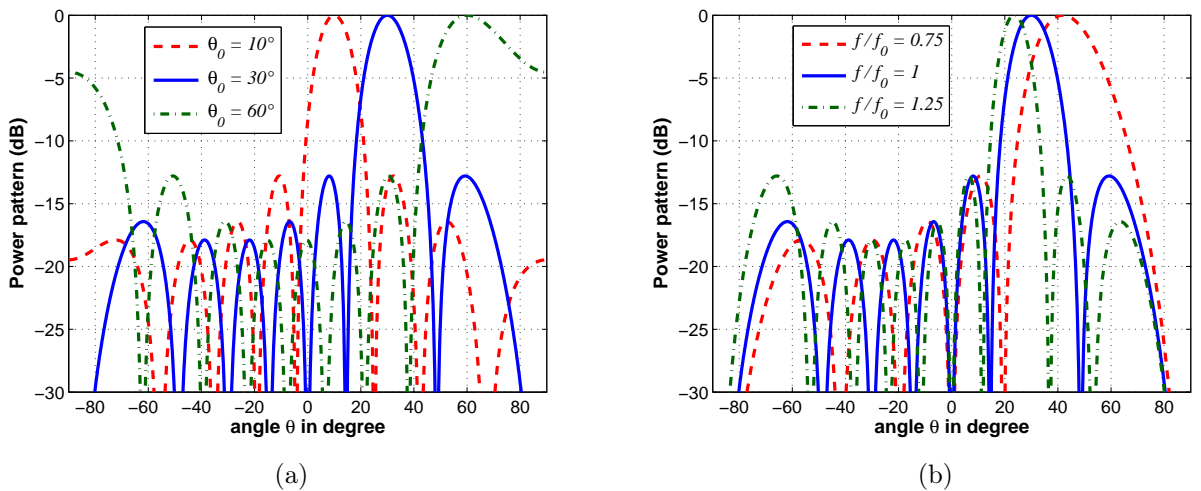
Figure 2.12: Phased array patterns (a)8-element phased array with beam scanning (b)Beam squinting phenomenon of 8-element phased array

We employ the equation (2.4.1) in order to see the effect of altering the working frequency in the phased array antenna. As can be seen, the normalized pattern is a function of the wave number k. With λ_0 corresponding to f_0, the operating frequency, the pattern at a shifted frequency f_1 can be written as

$$E_{norm}(\theta) = \frac{1}{N}\sum_{n=1}^{N} exp\left[j\left(2\pi\frac{f_1}{f_0}d/\lambda_0\,(n-1)\sin\theta + \alpha_n\right)\right] \qquad (2.4.4)$$

where

$$\alpha_n = -\frac{2\pi}{\lambda_0}d(n-1)\sin\theta_0. \qquad (2.4.5)$$

As described in equations (2.4.4), the beam scanning angle will be shifted when the working frequency is changed. This phenomenon is widely known as beam squinting [23] and it therefore limits the performance of a phased array antenna to only operate over a small bandwidth. Fig. 2.12(b) illustrates the *beam squinting* of a linear array where the value d/λ_0 is given as 0.5. It shows that by decreasing the operating frequency at the ratio 0.75, the beam is shifted approximately by $7°$ to the lower scanning angle and, on the other hand, by increasing the operating frequency at the ratio 1.25, the beam is shifted by around $11°$ to the higher scanning angle.

2.4.2 Time delay beam scanning

Another technique to realize the beam scanning antenna is by inserting time-delay into the feed network of the array antenna. The time delay beam scanning is widely utilized for broad band array antennas where the basic principle is that the beam is scanned to an oriented angle by progressively delaying the signal of the subsequent radiators. It can be realized by employing delay lines for instance by realizing a set of microstrip lines of different lengths.

As given in the equation (2.4.6), the radiated field is a function of the excitation phase

$$E_{norm}(\theta) = \frac{1}{N}\sum_{n=1}^{N} exp\left[j\left(2\pi\frac{f_1}{f_0}d/\lambda_0\,(n-1)\sin\theta + \alpha_n(f)\right)\right] \qquad (2.4.6)$$

To scan the beam to the angle θ_0 the excitation phase is given as

$$\begin{aligned} \alpha_n &= -kd\,(n-1)\sin\theta_0 \\ &= -2\pi f\tau_n \end{aligned} \qquad (2.4.7)$$

where τ_n is the time delay of the nth element. Assumed the length of the delay line of the nth element is given as L_n, the time delay is written as

$$\tau_n = \frac{L_n}{c_r} \qquad (2.4.8)$$

where c_r is the speed of the light in the material of the delay lines with relative permittivity ϵ_r. According to equations (2.4.7) and (2.4.8) the length of the delay lines for a desired scanning angle θ_0 can be formulated as

$$
L_n = \begin{cases} \dfrac{d\,(n-1)\sin\theta_0}{\sqrt{\epsilon_r}} & \text{for} \quad 0 \le \theta_0 \le 90 \\[2ex] \dfrac{d\,(N-n)\sin\theta_0}{\sqrt{\epsilon_r}} & \text{for} \ -90 \le \theta_0 \le 0 \end{cases} \tag{2.4.9}
$$
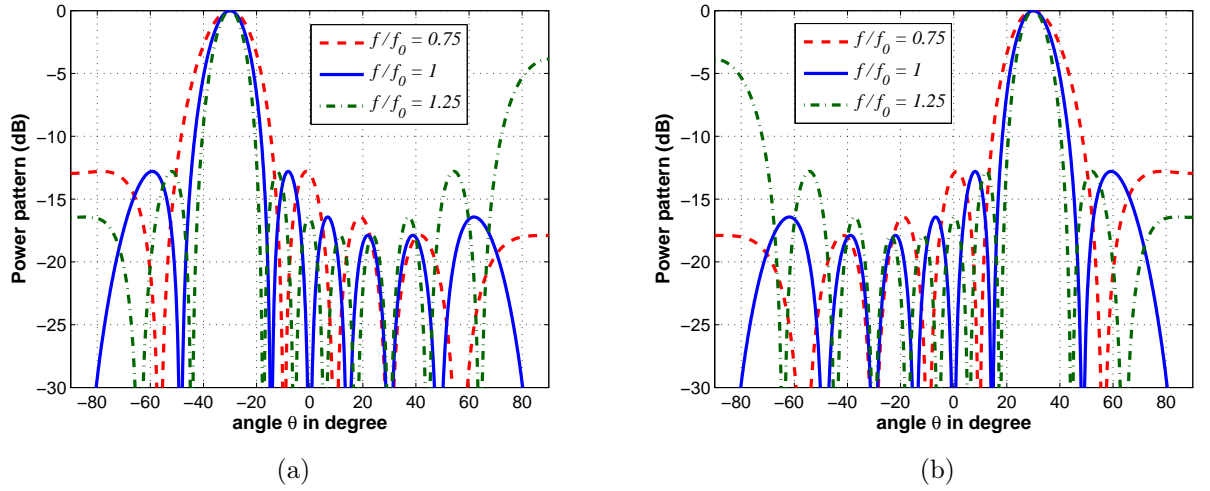
Figure 2.13: (a)Time delay beam scanning for scan angle -30°   (b)Time delay beam scanning for scan angle 30°
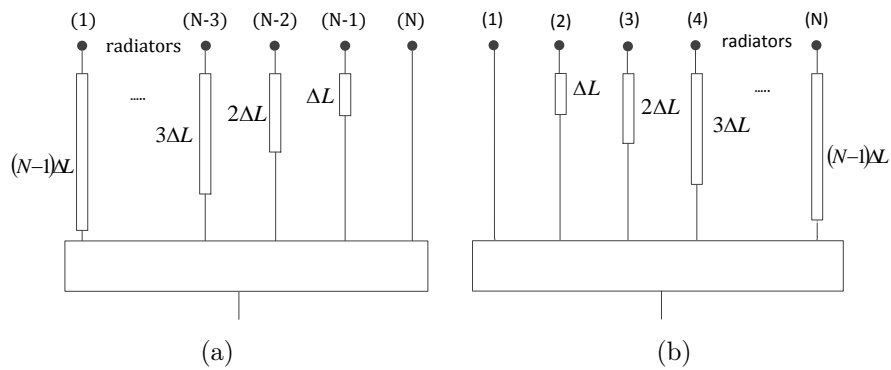
Figure 2.14: (a)Time delay configuration for $-90 \le \theta_0 \le 0$ (b)Time delay configuration for $0 \le \theta_0 \le 90$

Fig. 2.13(a) and Fig. 2.13(b) show the time delay beam steering of 8-elements uniform spacing linear arrays for $\theta_0 = -30°$ and $\theta_0 = 30°$. In this scenario, the operating frequency

is varied from ratio 0.75 to 1.25. It can be seen that the position of the main beam is kept constant and the beamwidth becomes smaller as the frequency increases.

Fig. 2.14(a) and Fig. 2.14(b) illustrate the configuration of the delay lines with progressive delay ΔL corresponding to the oriented scan angle where from (2.4.9) ΔL is obtained as

$$\Delta L = \frac{d \sin \theta_0}{\sqrt{\epsilon_r}} \tag{2.4.10}$$

To scan the beam toward the negative angles, the delay lines are designed decreasing progressively as shown in Fig. 2.14(a) and to scan the beam into the positive angles, the delay lines are designed increasing progressively as shown in Fig.2.14(b). The time delay is widely used for the wideband antenna arrays since the position of the beam can be kept constant. However, the beamwidth is seen to vary as the frequency increases/decreases. In chapter 5, we propose a different beam scanning concept by employing a set of low pass filters where the beamwidth can be maintained constant for the band of interest.

2.4.3 Beam scanning in the time domain

It is also highly interesting to investigate the contribution of the linear arrays to the pulse propagation. As discussed before in the sub section 2.3.3, the pattern of the antenna arrays in the frequency domain is strongly dependent on the operating frequency and the spacing between the elements. The main beam, side lobe and even grating lobes appear in the frequency domain representation. In order to see the time domain pattern of the linear arrays, one can start from the array factor as described before

$$AF(\theta) = \sum_{n=1}^{N} exp\left[j\left(kd\left(n-1\right)\sin\theta + \alpha_n\right)\right] \tag{2.4.11}$$

By making use of equation (2.4.11), the spacing between the elements can be expressed based on the time delay. It can be written as

$$AF(f,\theta) = \sum_{n=1}^{N} exp\left[j\left(2\pi f\left(\tau_d\left(n-1\right)\sin\theta - \tau_n\right)\right)\right] \tag{2.4.12}$$

where

$$\tau_d = \frac{c}{d} \tag{2.4.13}$$

and τ_n represents the time delay of the nth element. From equation (2.4.12), the time domain array factor $af(t,\theta)$ can be obtained by applying the inverse Fourier transform:

$$af(t,\theta) = \sum_{n=1}^{N} \delta\left(t - \left(n-1\right)\tau_d \sin\theta - \tau_n\right) \tag{2.4.14}$$

Assuming the array is excited by a pulse with duration T, the variable τ_d can be expressed as the fraction of T

$$\tau_d = K \cdot T \tag{2.4.15}$$

where K is a constant. By including the array factor into equation (2.2.13), the time domain radiation pattern of the linear array antenna can be given as

$$\frac{\boldsymbol{e}_{\mathrm{rad}}\left(t, \theta, \psi\right)}{\sqrt{Z_{\mathrm{F}}}} = \frac{1}{2\pi rc} \delta\left(t - \frac{r}{c}\right) * \boldsymbol{h}_{\mathrm{Ta}}\left(t, \theta, \psi\right) * af\left(t, \theta\right) * \frac{\partial}{\partial t} \frac{u_{\mathrm{TX}}\left(t\right)}{\sqrt{Z_{\mathrm{TX}}}} \tag{2.4.16}$$

where $\boldsymbol{h}_{\mathrm{Ta}}\left(t, \theta, \psi\right)$ represents the impulse response of the single antenna. The array factor in equation (2.4.16) relates to the uniform excitation and doesn't include a weighting function for the element currents. By including the weighting function w_n, the array factor can be written as [28]

$$af_w\left(t, \theta\right) = \sum_{n=1}^{N} w_n \delta\left(t - \left(n-1\right)\tau_d \sin\theta - \tau_n\right) \tag{2.4.17}$$

In the following simulation, we will illustrate the pulse propagation in order to investigate the contribution of the array factor to the spatial distribution of the radiated pulse. The scenario of the simulation is given as following. The uniform spacing linear array consist of 8-elements which are excited by the Gaussian pulse $p(t)$ where the duration of the pulse T is given as 300 ps. The spacing between the elements is denoted as $\frac{1}{2}cT$, where c is the speed of the light. In addition, the beam will be oriented to the scanning angle 30°. Furthermore, the elements are assumed as the isotropic radiators and the time derivative characteristic of the transmitter antenna is not included in this model. Therefore, the output of the array $y\left(t, \theta\right)$ is given as

$$y\left(t, \theta\right) = p(t) * af\left(t, \theta\right) \tag{2.4.18}$$

As can be seen in Fig. 2.15, the incident pulse flowing in the feed network is delayed progressively corresponding to the length of the delay lines. Due to the contribution of the delay lines, the pulse is steered to the scanning angle $\theta_0 = 30°$. At different angles toward the end-fire directions, the pulse is distorted, on the other hand at the oriented scanning angle the signal is increased and the shape of the pulse is maintained as well. With respect to the spatial distribution, peaks and nulls (as found as the side lobes in the frequency domain pattern) are not present in the time domain. This ideal representation of the pulse propagation shows that the array antenna is very efficient in an impulse radio system since the transmitted pulse can be gained and focused to a certain direction.

However, the antenna impulse response strongly affects the performance of the radiated pulse as shown in equation (2.4.16). In addition, the mutual coupling should be considered in the model as well since it yields a distortion to the antenna impulse response [29].
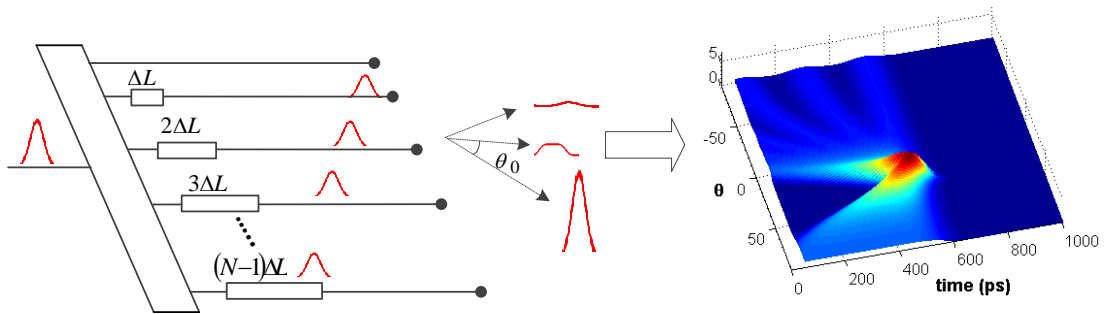
Figure 2.15: Pulse propagation of the linear arrays

3 Ultra-Wideband Printed Antenna

This chapter is dedicated to the discussion of UWB printed antennas. Firstly, some UWB printed antennas are introduced and their corresponding patterns are described. Further, the discussion is concentrated on designing a printed circular monopole antenna (PCMA) which starts out from the concept and continues to the simulation by using an industrial grade full-wave analysis EMPIRE XCcel [30]. A modification of the PCMA is carried out by reshaping the planar ground plane reflector in order to realize a directive PCMA. In order to achieve antenna impedance matching, the concept of matching circuit is introduced and then is applied to the PCMA. Finally, the mutual coupling of two directive PCMAs is investigated in order to utilize the directive PCMA as the element of a UWB linear array antenna.

3.1 Printed Antenna

3.1.1 The narrow band printed antenna

The printed antenna, generally known as microstrip antenna, is one of the most often designed commercial antennas due to its compact structure, light weight and low manufacturing cost [31]. Such kind of an antenna is generally designed as a thin metallic-patch printed on a grounded substrate. In addition, the microstrip antenna is widely integrated in many application systems for example integrated in aircraft platforms, remote sensing radars, radiometers, navigation system, and mobile radio systems [32].

The basic principle of the microstrip antenna is that the half-wavelength metal patch radiates electromagnetic waves at the patch edges where the so called *fringe field* generates maximum radiation at the normal direction of the antenna. The nearly hemispheric radiation characteristic allows a single microstrip antenna to generate relatively high gain, approximately 5-6 dBi. Eventhough the antenna has a number of advantages, the antenna is limited to operate only at a small frequency band; the bandwidth is around 1-10 % where the centre frequency is corresponding to the length of the metal patch. Some attemps have been done to increase the bandwidth of the antenna for instance by using a thicker substrate with low permittivity. However, the microstrip antenna is still not appropriate to be integrated in a UWB system since the bandwidth is not sufficient to cover the UWB frequency band.

3.1.2 Overview of UWB printed antenna

UWB antennas in planar technology actually have been investigated some decades ago, for instance the vivaldi antenna which covers the frequency range 2-20 GHz was investigated by Gibson in 1960 [33]. Since the FCC released free license for the UWB frequency band, international research has generated a lot of publications related to the topic of UWB antennas, specially UWB printed antennas. Some of the famous UWB printed antennas which can be widely found in the literature are the vivaldi antenna [34], printed circular monopole antenna (PCMA) [35] and printed circular dipole antenna (PCDA) [36]. In order to give a physical insight of UWB printed antenna, the layout and the pattern of the mentioned antennas will be shown.

(a)   (b)
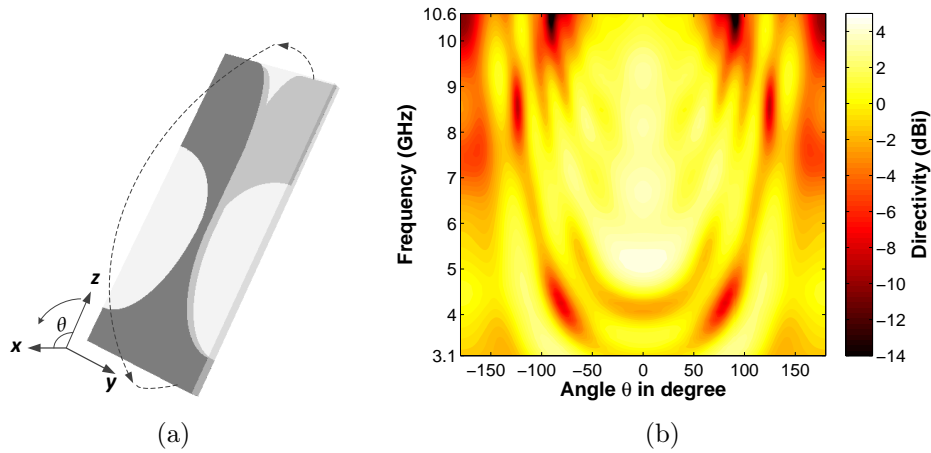
Figure 3.1: Vivaldi antenna (a)Layout (b)Pattern on the elevation plane

Fig. 3.1(a), 3.2(a) and 3.3(a) show the layout of some UWB antennas based on [34], [36] and [35] respectively. The layout of a vivaldi antenna, namely the balanced-antipodal vivaldi antenna [37] is described in Fig. 3.1(a). It can be seen that the combination of the metal layers in the vivaldi antenna is shaped as a flared tapered slot where such a tapered metalization strongly influences the wide band characteristic of the vivaldi antenna. Moreover, one cut-plane is illustrated in the picture as well, where the pattern of this cut-plane is shown in Fig.3.1(b). The pattern shows the directivity of the antenna for frequency 3.1-10.6 GHz. It can be seen that the vivaldi antenna has a directive pattern on the broadside direction(z-axis) in particular at the higher part of the frequency band where the maximum directivity of this antenna is calculated as 5 dBi.

The layout of a printed circular dipole antenna (PCDA) can be seen in Fig. 3.2(a). It shows a pair of circular radiator which is metalized on the top side of the substrate whereas the bottom side is partly metalized as the ground plane for the microstrip line. In this model, a 180° microstip-line phase converter is designed to reverse the phase of one circular radiator to make the two circular disks operating as a dipole. Further, the pattern of the PCDA for the corresponding cut-plane is depicted in Fig. 3.2(b) which shows a nearly omni-directional pattern in the frequency range 3-6 GHz.
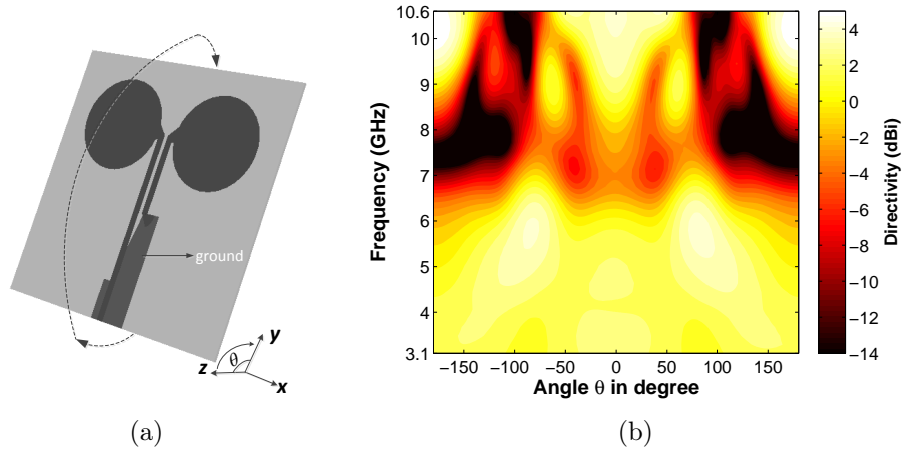
Figure 3.2: PCDA (a)Layout (b)Pattern on the elevation plane
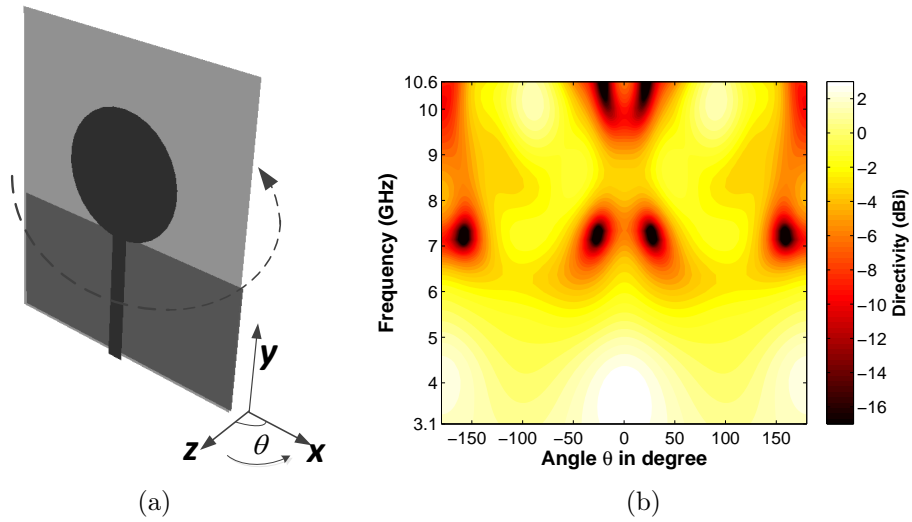
Figure 3.3: PCMA (a)Layout (b)Pattern on the elevation plane

Another layout of UWB printed antenna is given in Fig. 3.3(a). It shows a printed circular monopole antenna where a circular radiator is printed on the top side of the substrate and is fed by a microstrip line. On the other hand, the bottom side of the substrate is only partially metalized at the position below the microstrip line which is designed as the ground plane of PCMA. The dimensions of this design will be given in section 3.2.3. The pattern of the PCMA on the elevation plane is shown in Fig. 3.3(b) which describes a nearly omni-directional pattern in the frequency range 3.1-6 GHz where theoretically it gives an agreement with a rod monopole antenna which provides an omni-directional pattern on the corresponding plane.

Furthermore, the pattern of the PCMA on the azimuth plane can be seen in Fig. 3.4(b). It
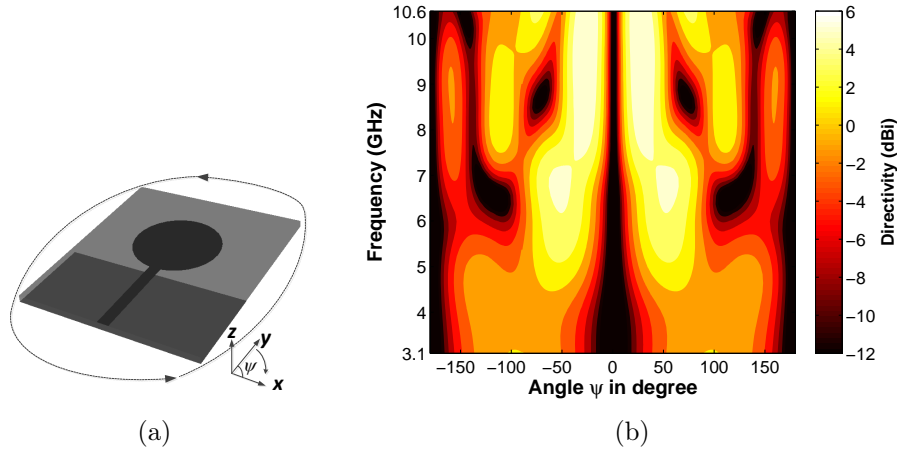
Figure 3.4: PCMA (a)Layout on the azimuth plane (b)Pattern on the azimuth plane

is seen that two symmetric beams raise on the right and the left side of the center position of the azimuth plane (xy-plane) where the peaks are found approximately at the angles -30° and 30°. In addition, the nulls is seen at the center position between the two peaks. Therefore, we call such a pattern as a V-pattern.

This introduction provides a brief description of UWB printed antenna patterns in the UWB frequency range. In many applications i.e. a home-based wireless system, it would be necessary to have a description of the antenna pattern, for example to select an antenna with a pattern appropriate to conform to the shape of a floor in the building. As an illustration, Fig. 3.5 shows a scenario of a floor plane which consists of O-shaped, I-shaped and V-shaped regions. Some antennas with particular patterns are required to be located in this floor plane in order to guarantee the quality of the signal. Such a scenario is called an adapted pattern floor plane and one investigation regarding to such a scenario by using a linear array dipole antenna has been shown in [19].

Based on the patterns which have been described before, the PCDA appropriates to be mounted in the O-shaped floor plane. The vivaldi antenna could be placed in the I-shaped floor plane and the PCMA regarding to its azimuth pattern could be located in the V-shaped floor plane. This scenario not only could be implemented in a building but also could be attractive to be implemented in a transportation system like in an aircraft cabin and inside a train to realize a high-speed wireless system. For example, a design of a double printed monopole antenna in terms of realizing a wireless in flight internet access system inside the aircraft cabin has been proposed in [38]

PCMA is a type of UWB printed monopole antenna similar to diamond-shaped printed monopole antenna [39], heart-shaped printed monopole antenna [40] and triangular printed monopole antenna [41]. Among the vivaldi antenna and the printed dipole antennas, the PCMA is the most compact UWB printed antenna. In addition, the PCMA has some advantages like simple structure, providing omni-directional pattern and very large bandwidth. This antenna not only provides omni-directional pattern on the elevation plane
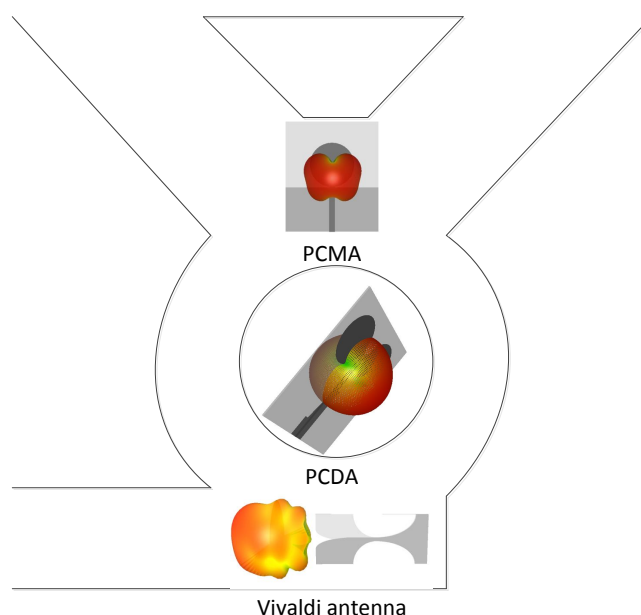
Figure 3.5: Floor plane scenario

but also provides V-pattern on the azimuth plane. Due to the reflected radiation on the ground plane, the maximum directivity in the azimuth plane is higher than the directivity in the elevation plane. Moreover, the investigation of the PCMA pattern is mainly still concentrated on the omni-directional characteristic. Therefore, it has drawn great interest to reinvestigate this antenna and to find the possibility to improve the pattern on the azimuth plane.

3.2 Printed Circular Monopole Antenna (PCMA)

3.2.1 Dipole and monopole antenna

The dipole antenna is the most simple antenna as depicted in Fig. 3.6 where the length of a two-arm thin metal rod is designed as half wavelength regarding to the operating frequency. The dipole antenna is widely utilized due to the omni-directional characteristic which produces directivity of approximately 2.3 dBi. A simple rod dipole antenna provides a small bandwidth. In order to extend the bandwidth, the rod and the transition from the feeding line to the radiator is modified as a tapered shaped conductor which is adapted based on the concept of a tapered transmission line. This concept is related to the invention of biconical antenna, one of the first broadband antenna, by Carter in 1939 and spherical dipole antenna by Schelkunoff in 1940 [42].

The monopole antenna is a derivative of the dipole antenna where the basic principle of the monopole antenna is correlated to the dipole antenna as can be seen in Fig. 3.6. Based on the electrical image theory, the one arm of the dipole antenna can be eliminated
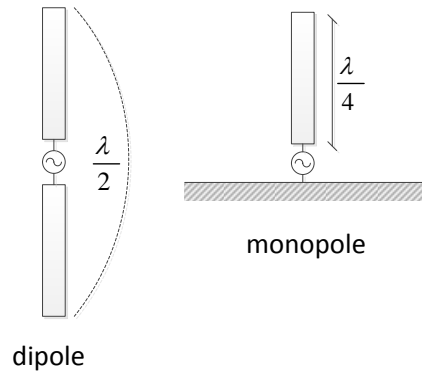
Figure 3.6: Dipole and monopole antenna

by using an infinite ground plane where the infinite ground plane works as an electric mirror. Hence, the dipole antenna can be substituted by a monopole antenna where the dimension of the monopole antenna is a quarter wavelength with respect to the operating frequency.

The monopole antenna is widely found in communication systems since it has smaller size than the dipole antenna while, on the other hand, still keeping the omni-directional characteristic. Further, the length of the monopole antenna can be shortened by modifying the top part of the monopole in order to realize a more compact structure, for example by realizing a top-loaded monopole antenna [43]. Another advantage of the monopole antenna is that it is very efficient to be mounted on a large metal surface where the metal can replace the antenna ground plane.

3.2.2 The geometry of UWB printed circular monopole antenna

The printed circular monopole antenna has been deeply investigated in [35]. The geometry of PCMA is adopted from the spherical monopole antenna as can be seen in Fig. 3.7(a). The spherical radiator is equivalent to a rod-monopole antenna yet it works for a larger bandwidth. In planar technology, the spherical radiator can be substituted by a printed circular disk on a planar substrate and the ground plane of the spherical monopole antenna is replaced by a printed ground plane as can be seen in Fig. 3.7(b).

As mentioned before, the basic principle of the monopole antenna is adopted from the dipole antenna based on the image theory where the size of the ground plane is assumed as infinity. In fact, the ground plane of a PCMA is arranged in the $x - y$ plane, i.e., is in plane with the monopole, as can be seen in Fig. 3.7(b), instead of orthogonal to the monopole and is realized in a limited way which makes the PCMA work rather like an asymmetrical dipole [44] where the size of the ground plane affects the characteristic of the asymmetrical dipole. In addition, the system ground plane behaves as a source of spurious radiation like a chassis. Therefore, any changes made in terms of the size and the position of the ground plane will change the performance of the PCMA.
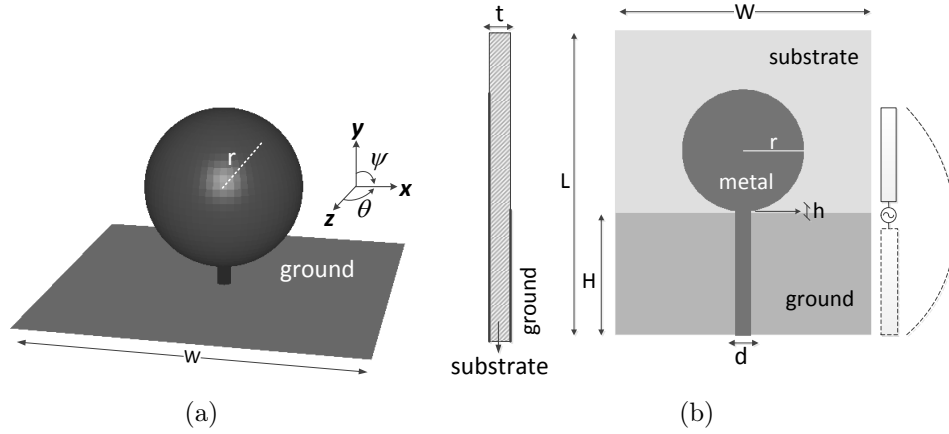
Figure 3.7: (a)Spherical monopole antenna (b)Schematic of PCMA
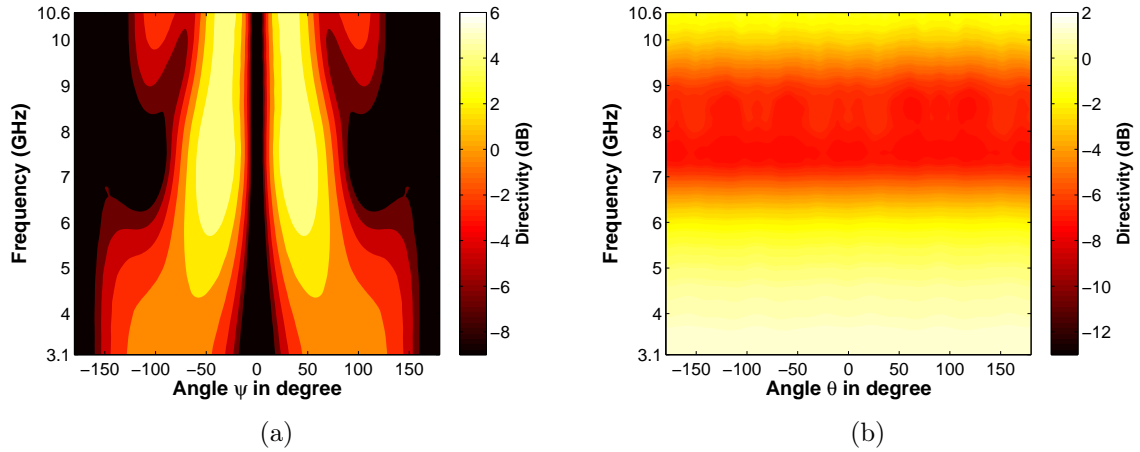
Figure 3.8: Patterns of of spherical monopole antenna (a)Azimuth plane (b)Elevation plane

Fig. 3.8(a) and Fig. 3.8(b) show the patterns of the spherical monopole antenna on the azimuth and the elevation plane respectively where in this model the radius r of the spherical is given as 10 mm and the width of the ground plane W is set as 40.8 mm. It shows a V-shaped pattern on the azimuth plane (x/y plane) and a perfectly omni-directional pattern on the elevation plane (x/z plane). The pattern on the elevation plane seems to be closer to the omni-directional characteristic as compared to the pattern of PCMA. It is due to the spherical geometry which provides equally spatial field distribution on the elevation plane.

3.2.3 The contribution of the substrate

It has been widely investigated that the properties of a microstrip antenna are strongly influenced by the permittivity and the thickness of the substrate. As well as in the microstrip antenna, the substrate affects the properties of UWB printed antennas even though the principle of the microstrip antenna and the UWB printed antenna are different. To see the contribution of the substrate to the UWB printed antenna properties, a PCMA with RT Duroid 5870 substrate is designed and then is compared to the PCMA which is developed by using FR4 substrate [35]. The dimension of the two PCMA models, which both correspond to the geometry in Fig. 3.7(b), are given in the table 3.1.

Table 3.1: Dimension of PCMA with FR4 and Duroid 5870 substrate (in mm)

PCMA	t	W	L	H	d	h	r
FR4 substrate[35], ϵ_r=4.7	1.5	42	50	20	2.6	0.3	10
Duroid 5870 substrate, ϵ_r=2.33	0.5	42	50	20	1.44	0.4	7.5

As shown in the table, the thickness t and the relative permittivity ϵ_r of the Duroid substrate differ. In addition, the radius of the circular disk r is optimized as 7.5 mm for Duroid substrate and 10 mm for FR4 substrate in order to achieve impedance matching to the 50 Ω microstrip feeding line with d calculated as 1.44 mm (Duroid) and 2.6 mm (FR4). The reflection coefficient of the two models can be seen in Fig. 3.9 which shows a maximum value of approximately -10 dB in the UWB frequency range. Moreover, some resonances are found in the calculation which are denoted by some minimum peaks in the curves.
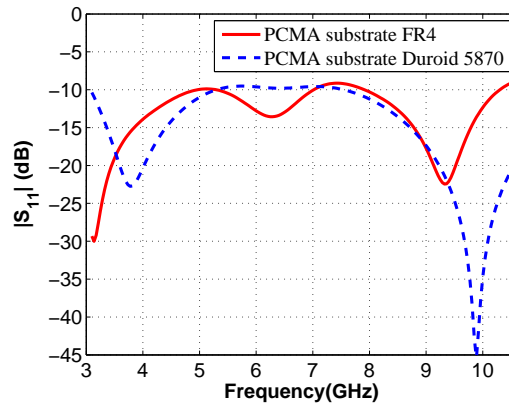
Figure 3.9: Reflection coefficients of PCMA substrate FR4 and substrate RT Duroid 5870

The pattern of the PCMA with Duroid substrate on the azimuth and elevation plane can be seen in Fig. 3.10(a) and Fig. 3.10(b) respectively. As depicted in Fig. 3.10(a), the
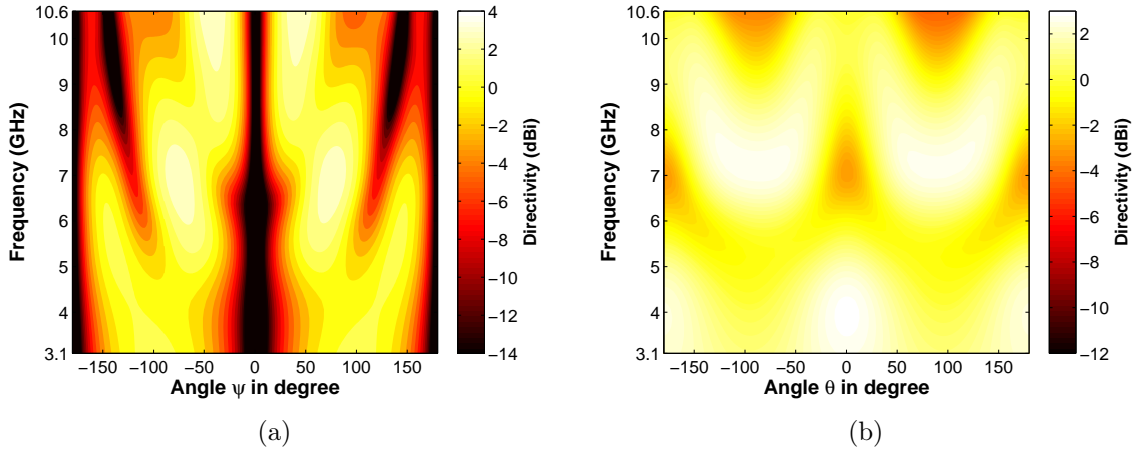
Figure 3.10: Patterns of PCMA with RT Duroid 5870 substrate (a)Azimuth plane (b)Elevation plane

azimuth pattern of PCMA with Duroid substrate shows a significant difference compared with the azimuth pattern of PCMA with FR4 substrate in Fig. 3.4(b). It can be seen that the maximum directivity of PCMA with Duroid substrate decreases to 4 dBi and the contour seems to be shifted to the higher frequency. It could be due to the effect of reducing the radius of the circular disk since a smaller radiator has smaller effective area than the larger one and additionally the smaller radiator makes the antenna to operate at the higher frequency range. On the other hand, the pattern of the PCMA with Duroid substrate on the elevation plane is depicted in Fig. 3.10(b) which seems to be closer to the omni-directional characteristic compared to the pattern of the FR4 version of PCMA in Fig.3.3(b). This deterioration at the higher frequency is expected as an effect of higher permittivity of FR4 substrate compared to the Duroid material.

Moreover, the influence of the substrate on the antenna pattern can be seen more clearly from the polar patterns in Fig. 3.11(a) and Fig. 3.11(b). Theoretically, the pattern of a monopole antenna on the elevation plane should be omni-directional. However, the patterns of the PCMA with FR4 substrate on the front and the back side of the antenna plane are not symmetric specifically at the upper part of frequency band as shown in Fig. 3.11(a). It can be seen that the pattern at 10 GHz is strongly degraded and the directivity at the angle $0°$ on the front side and at the angle $180°$ on the back side seem to be different. In addition, the radiation in the normal direction to the antenna plane is seen suppressed as compared to the radiation at the angles $-90°$ and $90°$. This could be the effect of the high permittivity substrate which influences the near-field of the PCMA. Likewise, as can be seen in Fig. 3.11(b), the PCMA with Duroid substrate shows more stable omni-directional patterns across the frequency. It appears that the omni-directional characteristic of the antenna can be maintained at the higher frequency. However, the trade-off by employing the lower permittivity substrate is that the physical stiffness of the antenna is reduced since the Duroid substrate is physically less rigid then the FR4 one. By using the Duroid and as well as the thinner substrate, the radiation performance of

the PCMA design in [35] can be improved.

(a)   (b)
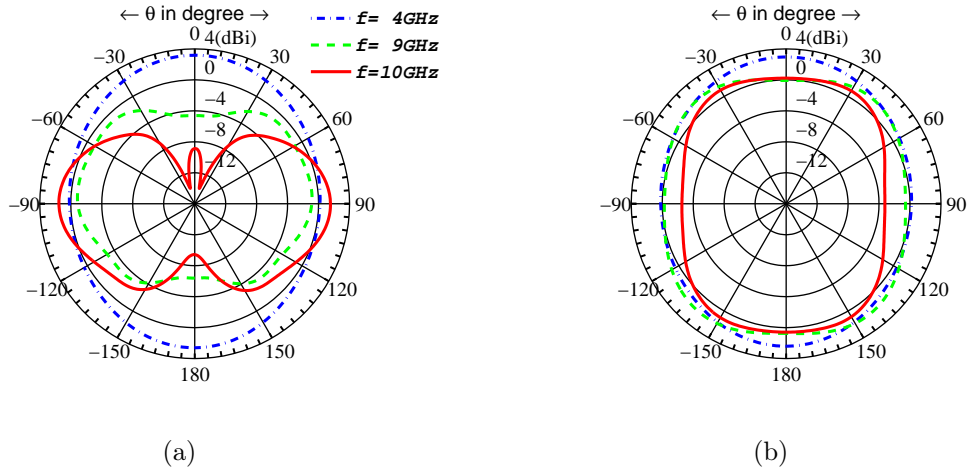
Figure 3.11: Polar pattern of PCMA on the elevation plane at frequencies: 4, 9 and 10 GHz (a)FR4 substrate (b)RT Duroid 5870 substrate

3.2.4 The contribution of the size of the ground plane

As discussed in subsection 3.2.2, any change in the size of the ground plane of PCMA will change the performance of the antenna.

(a)   (b)
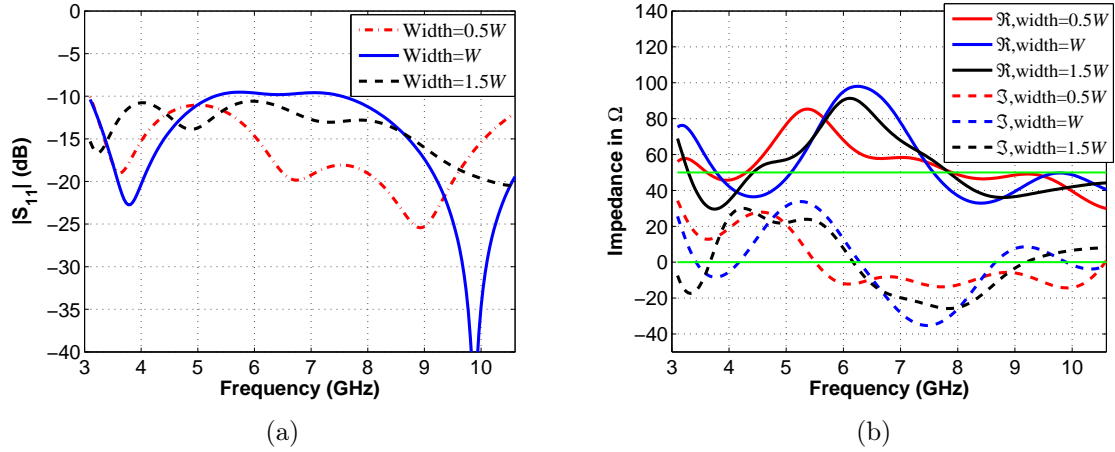
Figure 3.12: (a)Reflection coefficient of PCMA by varying the width of the ground plane W (b) Input impedance of PCMA, real part $\Re$ and imaginary part $\Im$, by varying the width of the ground plane W

In order to investigate the contribution of the ground plane, the PCMA on Duroid 5870 substrate is simulated by using the dimension provided in the table 3.1 where the width

of the ground plane W is modified as $0.5W$ and $1.5W$. Fig. 3.12(a) shows the reflection coefficients of the PCMA by varying the width of the ground plane. As can be seen in the picture, the reflection coefficient of the PCMA with dimension $0.5W$ is seen to be lower in the frequency range 5-9 GHz as compared with the original model. This could be due to the smaller size ground plane stimulating less electromagnetic coupling in this frequency range. Again, this can be seen from the antenna input impedance in Fig. 3.12(b) where in this frequency range the real part of the antenna input impedance is closer to 50 Ω and the imaginary part is closer to zero when the width of the ground plane is modified to $0.5W$.

(a)

(b)

(c)

(d)
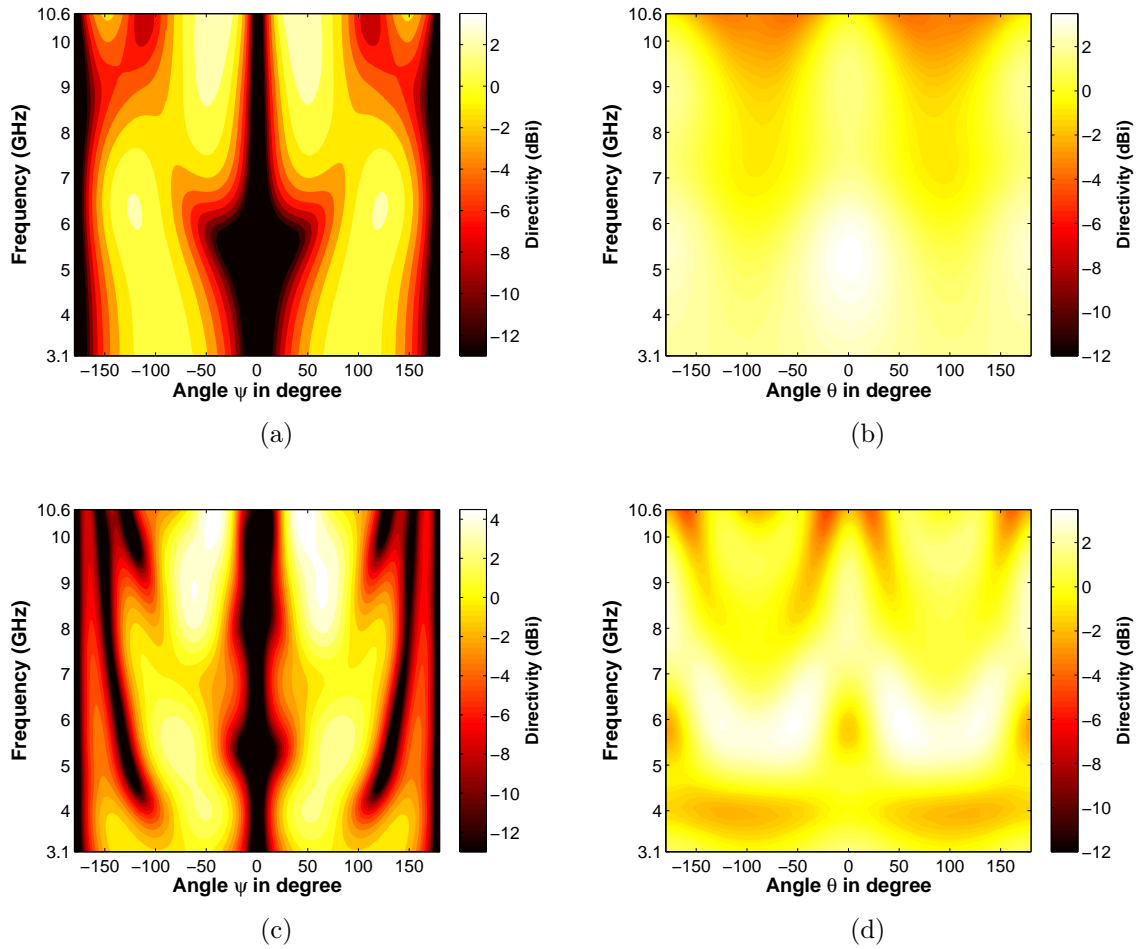
Figure 3.13: Contour plot of the pattern of PCMA with RT Duroid 5870 substrate by varying the width of the ground plane (a)Width=$0.5W$, azimuth plane (b)Width=$0.5W$, elevation plane (c)Width=$1.5W$, azimuth plane (d)Width=$1.5W$, elevation plane

Fig. 3.13 shows the PCMA pattern by varying the width of the ground plane. As can be compared in Fig. 3.13(a) and Fig. 3.13(c), the ground plane of dimension $1.5W$ generates more spurious radiation on the azimuth plane in comparison with the ground plane of dimension $0.5W$. Likewise, the larger ground plane seems to create higher peak directivity

on the azimuth plane than the smaller one. On the other hand, as can be compared in Fig.3.13(b) and Fig.3.13(d), the larger ground plane seems to stimulate spurious radiation on the elevation plane as well. As depicted in Fig.3.13(d), the effect of the spurious radiation can be seen clearly where the constructive superposition of radiation from the radiator and the ground plane is seen around the frequency 6 GHz whereas the destructive superposition of radiation from the circular disk and the ground plane appears around the frequency 4 GHz. It is also seen that the PCMA with smaller ground plane shows a more stable omni-directional pattern than the larger one as depicted in Fig.3.13(b).

By tuning the size of the ground plane, the spurious effects due to the interaction with the ground plane can be observed from the antenna pattern and the antenna input impedance. The best compromise between the amount of spurious radiation, the reflection coefficient and the maximum directivity could be achieved as well. According to these simulations, it is found that the PCMA with dimension W provides higher directivity than the PCMA with dimension $0.5W$ which, on the other hand, generates less spurious radiation than PCMA with dimension $1.5W$. Therefore, the model of the PCMA RT Duroid 5870 substrate with dimension W will be employed for the next investigation.

3.3 Directive Printed Circular Monopole Antenna

3.3.1 Nulls phenomenon in PCMA pattern

As shown in the previous simulations, the printed circular monopole antenna provides two distinct far-field characteristics on the elevation and the azimuth plane respectively. It provides an omni-directional pattern on the elevation plane which is required for many application systems, e.g. wireless LAN where the signal is expected to be transmitted equally for all direction. On the other hand, it provides the V-pattern on the azimuth plane which could be used in a V-shaped floor plane. Moreover, it can be seen that the maximum directivity of the azimuth pattern is higher than the maximum directivity of the elevation pattern due to the contribution of the ground plane. However, nulls are found on the center position of the azimuth pattern where, on the other hand, the radiation is essential in many applications requiring a broadside radiation pattern. Therefore, the question arises if it is possible to modify the V-pattern as a directive pattern where the nulls can be eliminated?

This nulls phenomenon can be derived mathematically based on the far-field equation of the monopole antenna which in the following derivation is approximated as the far-field equation of the Hertzian dipole, given as [12]:

$$\underline{E}_{\psi} = j\eta\frac{kI_0L\sin\psi}{4\pi r}e^{-jkr}, \qquad \underline{E}_{\theta} = 0 \tag{3.3.1}$$

where η, I_0, L, r represent the wave impedance, the current, the length of the Hertzian Dipole and the observation distance respectively. $\underline{E}_\psi$ and $\underline{E}_\theta$ represent the field on the azimuth plane and the field on the elevation plane as depicted in Fig. 3.14(a). In addition, the polarization of this model is the direction of $\underline{E}_\psi$. At the angle $\psi \approx 0$, it can be a approximated that $\sin\psi \approx \psi$ and the vector of $\underline{E}_\psi(\psi)$ at the angle $\psi \approx 0$ can be illustrated as the superposition of two vectors as shown in Fig. 3.14(b) where $\underline{E}_\psi(\psi_+)$ denotes the vector on the right side of the center position at $\psi = \psi_+$ and $\underline{E}_\psi(\psi_-)$ denotes the vector on the left side of the center position at $\psi = \psi_-$.

(a)   (b)
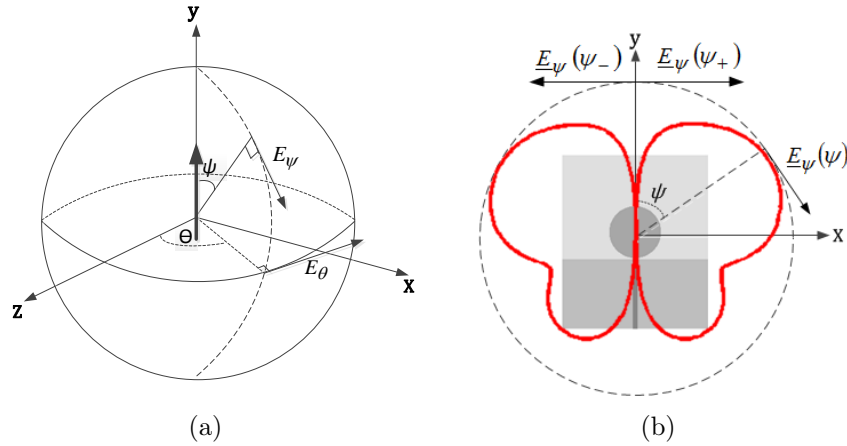
Figure 3.14: (a)Hertzian Dipole (b)PCMA azimuth pattern

Based on equation (3.3.1), the complex representation of $\underline{E}_\psi(\psi_+)$ and $\underline{E}_\psi(\psi_-)$ can be written as

$$\underline{E}_\psi(\psi_+) = \left|\underline{E}_\psi(\psi_+)\right| e^{j\phi_+} \tag{3.3.2}$$

$$\underline{E}_\psi(\psi_-) = \left|\underline{E}_\psi(\psi_-)\right| e^{j\phi_-} \tag{3.3.3}$$

where

$$\left|\underline{E}_\psi(\psi_+)\right| = \left|j\eta\frac{kI_0L\psi_+}{4\pi r}e^{-jkr}\right| \tag{3.3.4}$$

$$\left|\underline{E}_\psi(\psi_-)\right| = \left|j\eta\frac{kI_0L\psi_-}{4\pi r}e^{-jkr}\right| \tag{3.3.5}$$

and ϕ_+ and ϕ_- are the phases of the field components. The condition for a null at $\psi = 0°$ is

$$\underline{E}_\psi(\psi_+)\,\hat{e_\psi} + \underline{E}_\psi(\psi_-)\,\hat{e_\psi} = 0 \tag{3.3.6}$$

or

$$\left|\underline{E}_\psi(\psi_+)\right| e^{j\phi_+}\,\hat{e_\psi} + \left|\underline{E}_\psi(\psi_-)\right| e^{j\phi_-}\,\hat{e_\psi} = 0. \tag{3.3.7}$$

With the amplitude of the two vectors equal

$$\left| \underline{E}_\psi \left(\psi_+ \right) \right| = \left| \underline{E}_\psi \left(\psi_- \right) \right|, \tag{3.3.8}$$

the phase difference between $\underline{E}_\psi(\psi_+)$ and $\underline{E}_\psi(\psi_-)$ is obtained as

$$\phi_+ = \pi \pm \phi_- \tag{3.3.9}$$

Therefore, it can be concluded that the nulls in the PCMA pattern are created since the amplitude of the far-field vectors on the right and the left side of the antenna are equal, yet the phase of the two vectors are different by π radian.
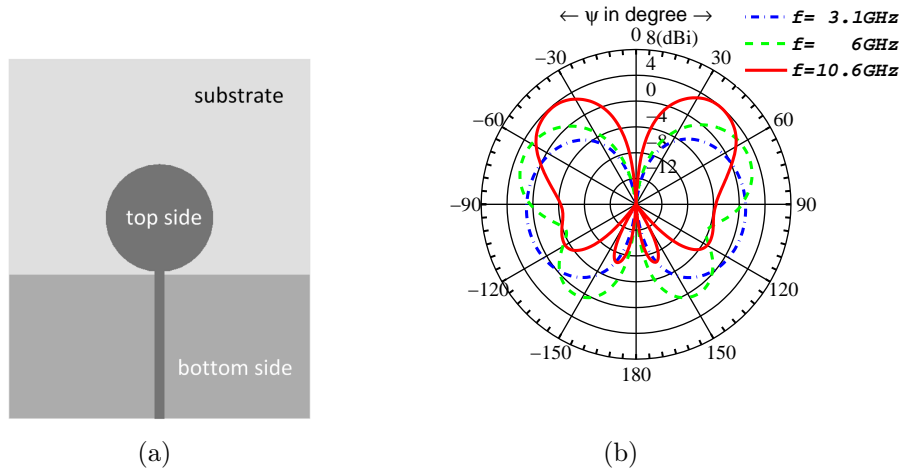
Figure 3.15: PCMA with substrate RT Duroid 5870 (a)Layout (b)Polar pattern on the azimuth plane
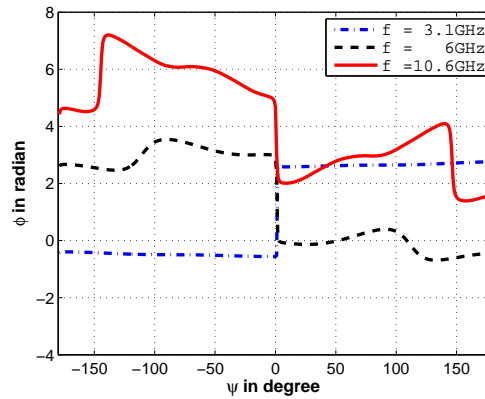
Figure 3.16: Phase of the far-field of PCMA with substrate RT Duroid 5870 on the azimuth plane

As a verification, the amplitude and the phase of the far-field of PCMA is calculated numerically. The polar pattern of the PCMA with substrate Duroid on the azimuth plane

for frequencies 3.1, 6 and 10.6 GHz is shown in Fig. 3.15(b) whereas the phase of the corresponding frequencies is shown in Fig. 3.16. It can be seen that the amplitude of the far-field on the right and the left side at the center position are identical and the phase seems to be nearly symmetrical with respect to the center position, yet at the angles 0° as well as 180° the phase changes by π radian. This remarkable phase transition denotes the null positions on the pattern which verifies the analytical expression.

3.3.2 L-shaped reflector PCMA

The nulls can be eliminated by changing either the 180° phase-difference or the amplitude of the vector $\underline{E}_\psi(\psi_+)$ and $\underline{E}_\psi(\psi_-)$ in terms of making the resultant vector at the center position to be unequal to zero. This can be realized by placing an additional reflector unsymmetrically expecting that the scattered radiation from the reflector would superimpose the radiation from the circular disk changing the resultant vector of the electric field on the center position. Fig. 3.17 shows the onset of a monopole antenna with additional
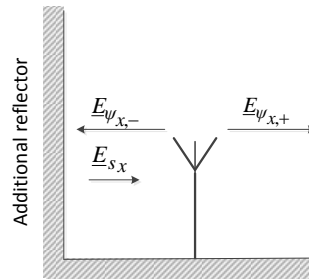
Figure 3.17: Additional reflector

reflector on the left side. The component of electric field vectors on the x-component are expressed as $\underline{E}_{\psi_{x,+}}$, $\underline{E}_{\psi_{x,-}}$ and $\underline{E}_{s_x}$, where $\underline{E}_{\psi_{x,+}}$ and $\underline{E}_{\psi_{x,-}}$ represent the electric field generated by the monopole on the right and left side respectively whereas $\underline{E}_{s_x}$ represents the scattered field from the reflector wall. The total field on the right and the left side are represented as $\underline{E}_{x,+}$ and $\underline{E}_{x,-}$ respectively, and their relations with the component of the electric vectors in the x-axis are

$$\underline{E}_{x,+} = \underline{E}_{\psi_{x,+}} + \underline{E}_{s_{x,+}}$$
$$\underline{E}_{x,-} = \underline{E}_{\psi_{x,-}} - \underline{E}_{s_{x,-}} \tag{3.3.10}$$

Equation (3.3.10) shows that the total electric field vectors on the left and the right side of the monopole are changed unsymmetrically due to the reflector. Therefore, this approach eliminates the null at the center position.

One realization of a planar reflector integrated in the PCMA can be seen in Fig. 3.18(a) where such a reflector is denoted as L-shaped reflector [45]. It can be seen that an additional planar wall with width D is added to the ground plane of PCMA with Duroid substrate in order to alter resultant far-field. The polar pattern for frequencies 3.1, 6 and
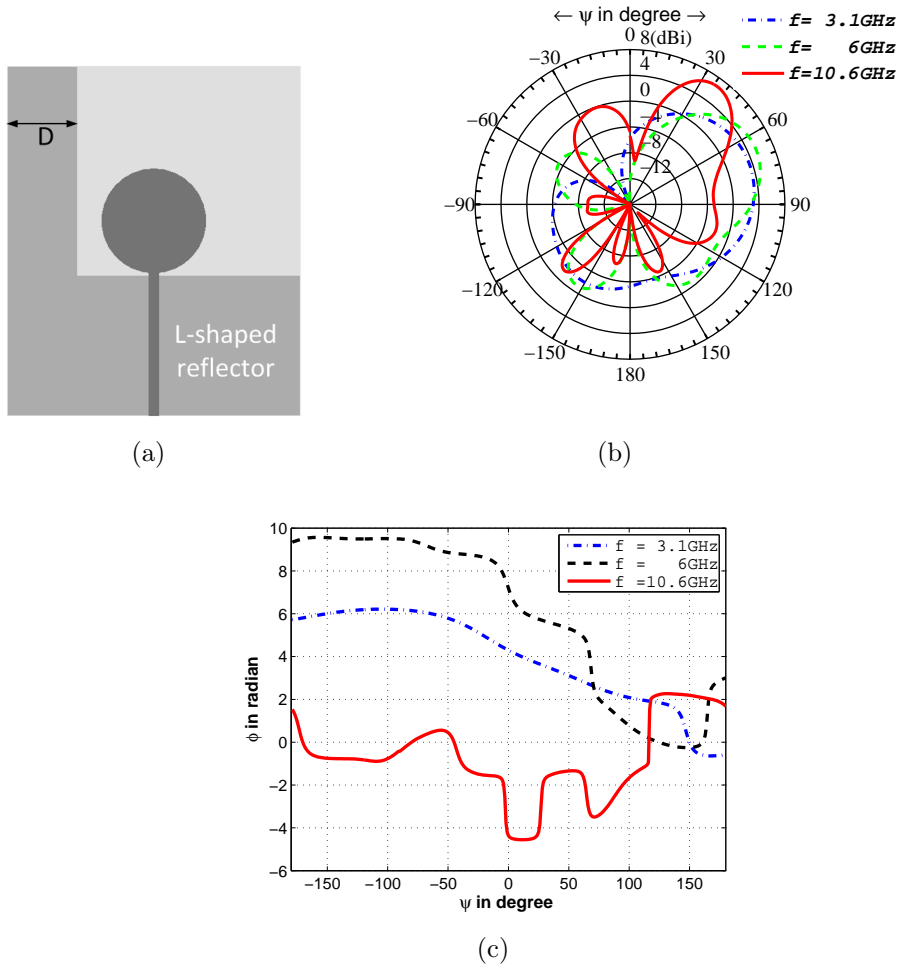
Figure 3.18: *L*-shaped PCMA (a)Layout (b)Polar pattern on the azimuth plane (c)Phase of the far-field

10.6 GHz is shown in Fig. 3.18(b) where in this scenario *D* is 10 mm. From the polar pattern, it appears that the beam of PCMA is changed dramatically where the null position is not only shifted from the center position but also the beam is steered to the right side and the maximum directivity increases as well.

However, the additional reflector not only gives contribution to the radiation pattern but also affects the reflection coefficient of the PCMA since the reflected field from the wall impinges the circular disk producing additional electromagnetic coupling. The reflection coefficient of the *L*-shaped PCMA can be seen in Fig. 3.19(a). In comparison with the reflection coefficient of the original PCMA, it is seen to be higher for the whole frequency band. Furthermore, the effect of the coupling can be seen clearly from the antenna input impedance as shown in Fig. 3.19(b). The deviation of the real and imaginary part of the input impedance due to the reflector can be seen in this presentation. It shows that the electromagnetic coupling due to the reflection from the wall changes the input impedance across the whole frequency band where the highest deviation of the real part is found at 6.5
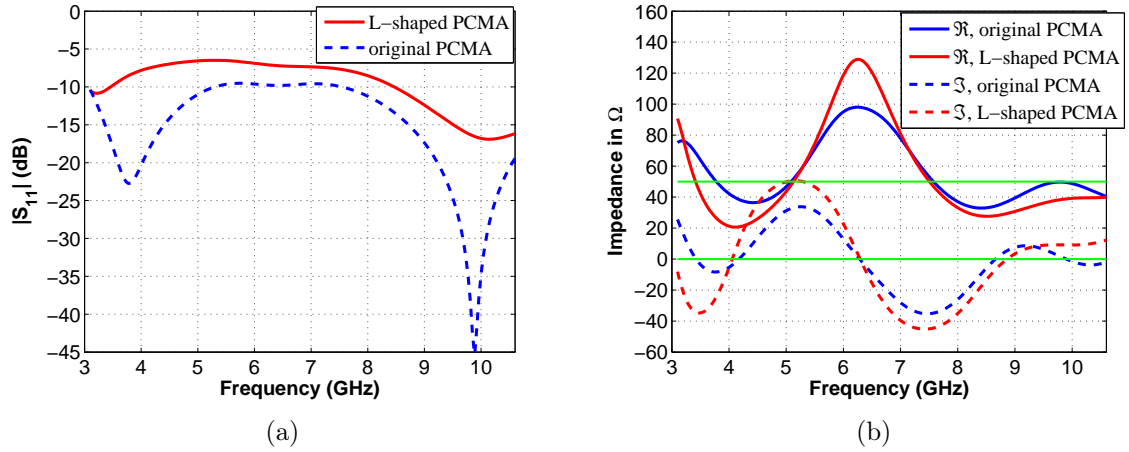
Figure 3.19: (a)Reflection coefficients of *L*-shaped PCMA compared to original PCMA (b)Input impedance of *L*-shaped PCMA and original PCMA, real part $\Re$ and imaginary part $\Im$

GHz and the highest deviation of the imaginary part is found at 5 GHz. To compensate such a deviation, an optimization can be done by tuning the geometry of the PCMA. An alternative solution can be achieved by realizing a matching circuit in the feeding line to match the antenna input impedance.

3.3.3 Strategy to realize the antenna impedance matching

Microstrip shunt-stub

A basic matching circuit in planar technology can be realized by using a microstrip stub, which can be designed as a series or a shunt stub [46]. The stub can be realized either as an open or a short stub where the short stub can be implemented by using a ground via. The open stub is more practicably implemented in a planar circuit, on the other hand, the short stub is best implemented in waveguide technology. In this sub-section, the analytical design of a microstrip stub matching circuit, especially using an open shunt-stub will be summarized and the concept of implementing the shunt stub matching circuit in a PCMA will be discussed as well. Fig. 3.20 illustrates the matching circuit using a shunt stub
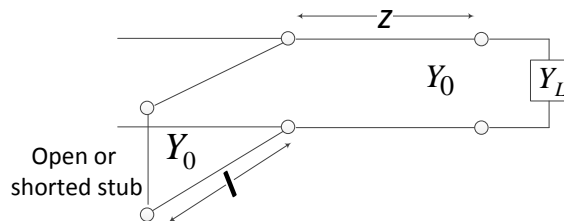
Figure 3.20: Shunt stub

which is inserted in a transmission line which is terminated by a load with admittance Y_L. In addition, the characteristic admittance of the shunt stub and the transmission line are denoted as Y_0. The shunt stub is located at a position z from the load and the length of the shunt stub is represented as l. The tasks of designing the shunt stub are: to find the best position of the stub from the load and to calculate the length of the shunt stub. The mathematical expression to calculate the shunt stub is given in [46] and will be summarized as following.

The load impedance Z_L can be written as $Z_L = 1/Y_L = R_L + jX_L$ where the value of impedance Z at a distance z from the load is given as

$$Z = Z_0 \frac{(R_L + jX_L) + jZ_0 t}{Z_0 + j(R_L + jX_L)t}, \tag{3.3.11}$$

where $t = \tan\left(\frac{2\pi z}{\lambda}\right)$, the admittance Y at this position is written as

$$Y = \frac{1}{Z} = G + jB, \tag{3.3.12}$$

where

$$G = \frac{R_L + (1 + t^2)}{R_L^2 + (X_L + Z_0 t)^2} \tag{3.3.13}$$

and

$$B = \frac{R_L^2 t - (Z_0 - X_L t)(X_L + Z_0 t)}{Z_0 \left[R_L^2 + (X_L + Z_0 t)^2\right]}. \tag{3.3.14}$$

The first step is to find the value of t which matches the real part $G = Y_0$. According to equation (3.3.13), this yields a quadratic equation

$$Z_0 (R_L - Z_0) t^2 - 2X_L Z_0 t + \left(R_L Z_0 - R_L^2 - X_L^2\right) = 0 \tag{3.3.15}$$

The value of t is obtained as the solutions of the quadratic equation

$$t = \frac{X_L \pm \sqrt{R_L \left[(Z_0 - R_L)^2 + X_L^2\right]/Z_0}}{R_L - Z_0}, \quad R_L \neq Z_0 \tag{3.3.16}$$

if $R_L = Z_0$ then $t = -X_L/2Z_0$. Hence, the solutions of z are

$$z/\lambda = \begin{cases} \dfrac{1}{2\pi} \tan^{-1} t, & \text{for } t \geq 0 \\[2mm] \dfrac{1}{2\pi} \left(\tan^{-1} t + \pi\right), & \text{for } t < 0 \end{cases} \tag{3.3.17}$$

The second step is to calculate the length of the open shunt stub l which is given by equation

$$\frac{l}{\lambda} = \frac{1}{2\pi} \tan^{-1} \left(\frac{B_s}{Y_0}\right), \tag{3.3.18}$$

where the shunt susceptance is given as $B_s = -B$. Thus, the length of the open shunt-stub is obtained as

$$l = \frac{1}{2\pi} \tan^{-1}\left(\frac{B}{Y_0}\right)\lambda. \tag{3.3.19}$$

Since the stub is realized as a microstrip-line stub, the wavelength λ in equations (3.3.17) and (3.3.19) is calculated as the effective wavelength λ_e, defined as

$$\lambda_e = \lambda_0/\sqrt{\epsilon_e}. \tag{3.3.20}$$

λ_0 represents the free-space wavelength and ϵ_e represents the effective dielectric permittivity which is calculated based on the thickness of the substrates t and the width of the microstrip line d, approximately given as [46]

$$\epsilon_e = \frac{\epsilon_r + 1}{2} + \frac{\epsilon_r - 1}{2} \frac{1}{\sqrt{1 + 12t/d}} \tag{3.3.21}$$
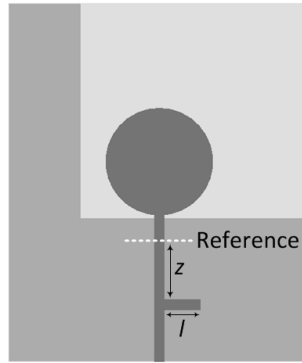
Figure 3.21: Open shunt-stub integrated in the L-shaped PCMA

The open matching stub integrated in the L-shaped PCMA can be seen in Fig. 3.21. In order to find the position of the matching stub, a reference plane is considered where the impedance represents the load Z_L, and the real/imaginary part of the impedance can be obtained from numerical calculation. The next step is to find the distance z from the reference plane and the length l of the open stub with respect to a particular frequency.

Fig. 3.22(a) shows the reflection coefficient of the L-shaped PCMA after the matching stub is inserted in the feeding line where in this scenario the open shunt stub is designed to achieve the impedance matching at 5.5 GHz. It can be seen that the reflection coefficient of the L-shaped PCMA is changed dramatically at 5.5 GHz. However, it effects the reflection coefficient of the other parts of the frequency band. It is also clearly seen from the antenna input impedance as calculated in Fig. 3.22(b). It shows that the real part of the input impedance is close to 50 Ω whereas the imaginary part of the input impedance is close to zero, yet above 7 GHz as well as below 4 GHz the input impedance strongly deviates from the reference.
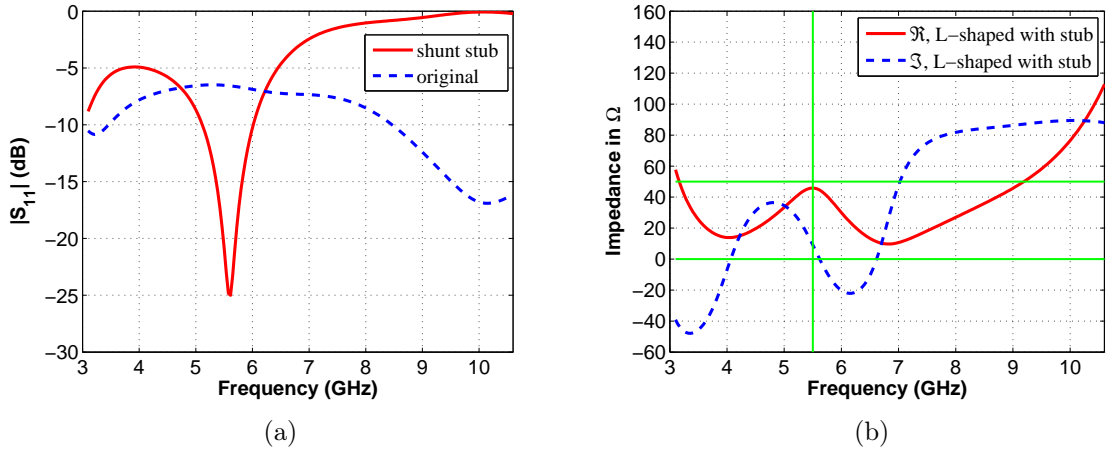
Figure 3.22: (a) Reflection coefficients of *L*-shaped PCMA with stub compared to original *L*-shaped PCMA (b)Input impedance of *L*-shaped PCMA with shunt stub, real part $\Re$ and imaginary part $\Im$

Considering the analytical expression and the simulation, the single shunt-stub achieves the impedance matching over a small frequency band only. It can be seen from equations (3.3.17) and (3.3.19) where the position of the stub position z and the length of the stub l are functions of the wavelength λ. By employing the shunt stub, matching for a certain part of the whole frequency band can be achieved which is called local matching. However, the local matching changes the reflection coefficient of the rest of frequency band as well. Therefore, a single stub can't be employed to achieve the impedance matching over the total UWB frequency band, yet it can be used as a preliminary step to optimize the impedance matching if the local matching doesn't effect the reflection coefficient of the rest of the frequency band dramatically, i.e, a trade-off between the local impedance matching and the reflection coefficient of the rest of the frequency band can be achieved. In addition, it can be used simultaneously with an additional matching method in order to achieve the impedance match over the whole frequency band.

Optimizing the feeding line transition of the PCMA
As discussed before, the planar ground plane scatters the radiation from the circular disk. A part of the radiation impinges at the circular disk and the microstrip-line transition below the circular disk. The electromagnetic coupling into the microstrip-line transition can be assumed to strongly influence the antenna input impedance since this part is very close to the ground plane and the circular disk. Therefore, by changing the width of the microstrip line in this part is expected to give a considerably contribution to the optimization of the matching impedance.

In order to prove this approach, the field distribution of a PCMA is simulated as can be seen in Fig. 3.23. In this scenario, the electric field component in *y*-direction, which is denoted as E_y, is plotted since this component is strongly contributed by the reflected radiation from the ground plane. It can be seen that the strong electric field distribution can be found in the area below the circular disk which, on the other hand, indicates
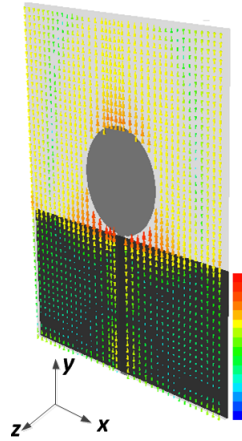
Figure 3.23: E_y-field distribution on the x-y plane of the PCMA with Duroid 5870 substrate

that the transition gap between the circular disk and the ground plane suffers a strong electromagnetic coupling. A concept for impedance matching, therefore, modifies the geometry of the transmission line in this area.

(a) (b)
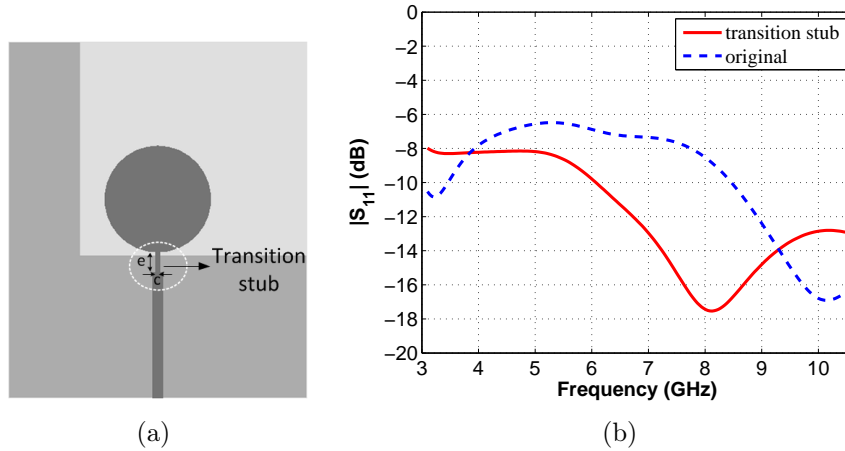
Figure 3.24: (a) Transition stub integrated in the L-shaped PCMA (b)Reflection coefficients of L-shaped PCMA with transition stub compared to original L-shaped PCMA

Fig. 3.24(a) shows an L-shaped PCMA with a modified microstrip line transition where the width of the microstrip line along the length of e below the circular disk is reduced as c. The reflection coefficient of this design can be seen in Fig. 3.24(b) where in this scenario the value of e and c are optimized as 2.8 mm and 0.8 mm. It shows that the reflection coefficient is improved in the frequency range 4 to 9.2 GHz and the reflection coefficient of better than -10 dB can be achieved for the frequency range above 6 GHz. Therefore, this method is very effective to improve the impedance matching of the PCMA with L-shaped

reflector ground plane. The same method, yet by including a dual-microstrip transition has been presented in [47] to match a PCMA from 3.5 to 31.9 GHz.

Microstrip pin stub

Another approach to achieve impedance matching of the PCMA is placing pin stubs from the circular disk radiator to the planar ground plane.
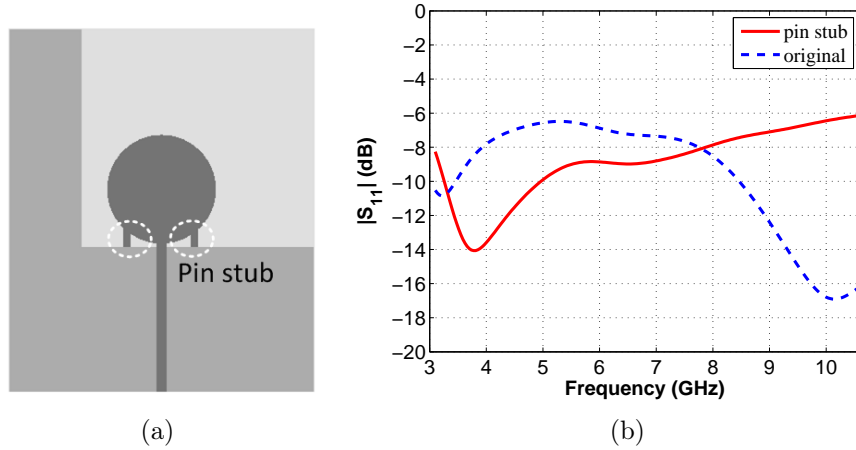
Figure 3.25: (a) Pin-stub integrated in the *L*-shaped PCMA (b)Reflection coefficients of *L*-shaped PCMA with pin stub compared to original *L*-shaped PCMA

The idea of utilizing microstrip pin stubs to improve the impedance matching of a printed monopole antenna has been proposed in [48]. The layout of the pin stubs integrated in an *L*-shaped PCMA can be seen in Fig. 3.25(a). In this design, two pin stubs are placed at the lower part of the circular disk and the length of the pin stub is adjusted to the top position of the ground plane without overlap. As has been shown in [48], the pin stub is considerably effective to achieve a local matching at the lower frequency band of a printed monopole antenna.

Fig. 3.25(b) shows the reflection coefficient of the *L*-shaped PCMA by utilizing the pin stubs. It can be seen that the reflection coefficient of this design decreases at the lower frequency band from 3.3-7.8 GHz. Even thought the impedance matching over the full frequency band can not be achieved, the pin-stub could be combined with the other matching methods to match the input impedance of a printed monopole antenna over a broad band.

3.3.4 *U*-shaped reflector PCMA

A different type of planar reflector to realize a directive PCMA is a parabolic reflector which has been proposed in [49]. The basic idea of the parabolic reflector is similar to the *L*-shaped reflector where the scattered radiation from the planar reflector superimposes the radiation from the circular disk to yield a directive pattern on the azimuth plane.

However, the resultant beam is not focused on the center position and also the direction of the beam strongly varies with the frequency as shown in Fig. 3.18(b). Therefore, a PCMA with a modified reflector, the so-called U-shaped reflector is proposed.

Fig. 3.26(a), 3.26(c) and 3.26(e) describe the sequential strategy to realize a PCMA with U-shaped ground plane. First, the PCMA with RT Duroid 5870 substrate is designed as shown in Fig. 3.26(a). Secondly, the circular radiator is tilted by 45° where the ground plane reflector conforms to its direction and a wall reflector is added at the left side of the circular disk as depicted in Fig. 3.26(c). Finally, another wall reflector is located at the right side of the circular disk which reshapes the ground plane as U-shaped reflector, Fig. 3.26(e).

Table 3.2: Dimension of inclined disk PCMA and U-shaped PCMA (in mm)

PCMA	W	L	H	D	h	r	a	b	c	l	y	d
Inclined disk	49.2	53	13.7	10	0.6	7.5	17.5	14.5	1	19.5	19.5	1.44
U-shaped	56	53.7	13.7	10	0.6	7.5	17.5	14.5	1	16.2	20.2	1.44

The polar patterns of the inclined reflector PCMA and of the U-shaped reflector PCMA can be seen in Fig. 3.26(d)and Fig. 3.26(f) respectively where the dimensions of both scenarios are provided in table 3.2. Further, the polar pattern of the two models for frequencies 3.1, 6, 10.6 GHz can be compared to the polar pattern of the original model in Fig. 3.26(b). The beams of the inclined reflector PCMA in Fig. 3.26(d) is scanned by approximately 45°, the tilt angle of the circular disk. The null position seems to be shifted to this angle whereas the beam at the left side points to center position. This could be an effective strategy to eliminate the null on the center position for the whole range of frequency which, at the same time, generates high gain at this position. However, the directivity on the right side of the null at approximately 90° is relatively high since the right side of the V-shaped beam is scanned as well, and this would be undesirable in many applications. By using the U-shaped reflector which is depicted in Fig. 3.26(e), this beam can be suppressed where, at the same time, the other one on the center position is amplified as shown in Fig. 3.26(f).

(a)

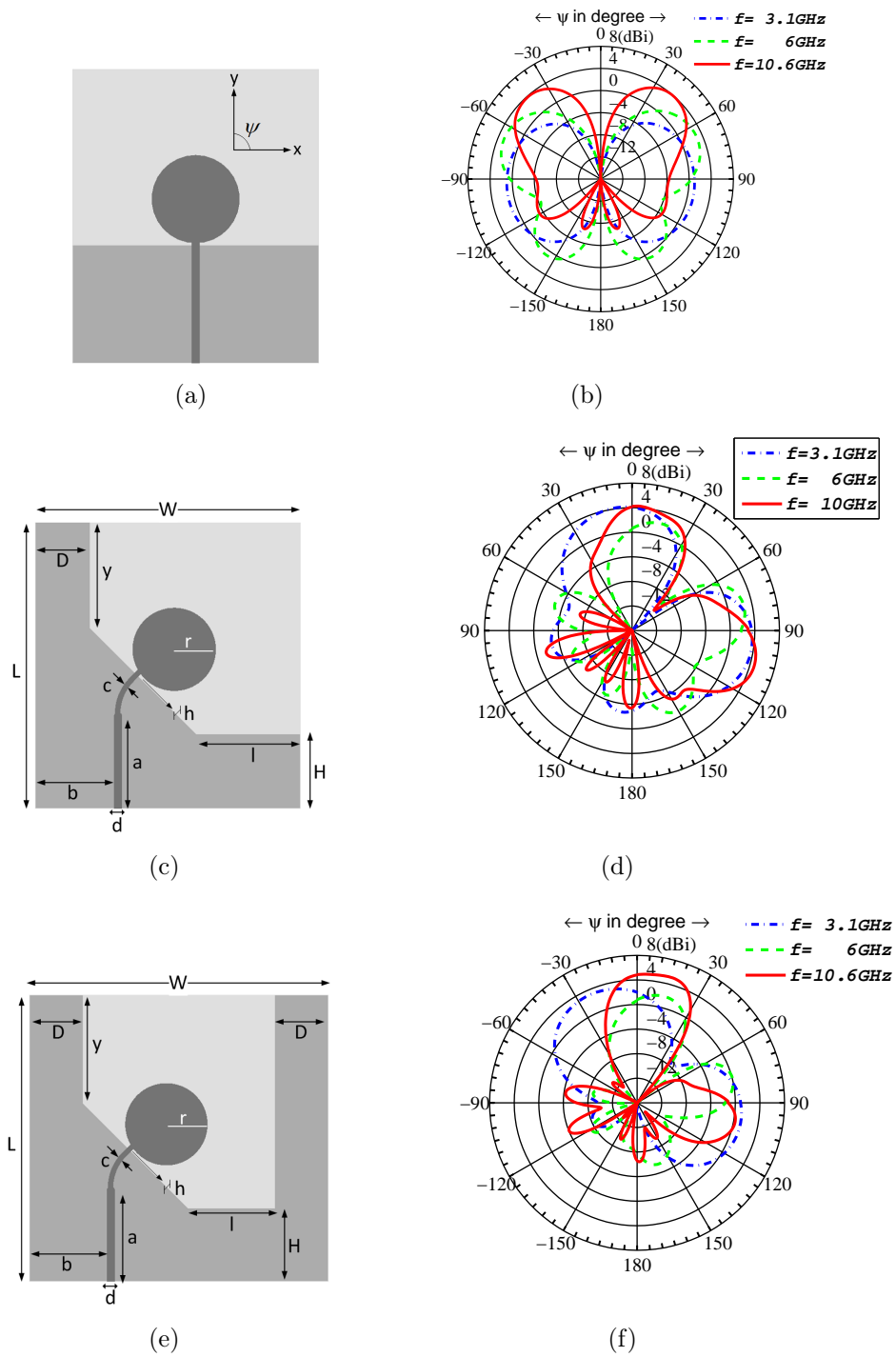(b)

(c)

(d)

(e)

(f)

Figure 3.26: Reshaping of PCMA on RT Duroid 5870 substrate (a)Original PCMA (b)Polar pattern of original PCMA (c)Inclined PCMA (d)Polar pattern of inclined PCMA (e)PCMA with U-shaped reflector (f)Polar pattern of PCMA with U-shaped reflector

3.3.5 Mutual coupling investigation in PCMA

As discussed in chapter 2, the source of the electromagnetic coupling is not only the scattered radiation from the ground plane but also the electromagnetic coupling of the element interaction in the array. Such a coupling changes the input impedance and the pattern of each element. Therefore, less mutual coupling between the elements is a goal in designing an antenna array. With respect to the planar array antenna, some ideas have been proposed in order to suppress the mutual coupling. A new concept uses electronic band gap (EBG) structures, e.g., in a microstrip array antenna since the EBG structure can suppress the surface wave propagating on the substrate. The EBG structure has been successfully used to reduce the mutual coupling of narrow-band planar array antennas as shown in [50]. In order to suppress the mutual coupling of an UWB array antenna, it requires theoretically a more complex periodic structure. With respect to the geometry and the cost, an effective strategy to design an EBG structure for UWB array antennas is required. Research related to this issue is still limited and it could be an interesting issue in the future. The reference [51] shows a recent investigation related to the EBG structure for a double UWB printed antenna.

In this work, a different approach is proposed to reduce the coupling between PCMAs. Since the principle of a microstrip antenna and a UWB printed antenna is different, the surface wave is not assumed as the main source of the coupling in an UWB array antenna. However, the direct radiation from the neighbouring elements is expected to be the main source of electromagnetic coupling. Since such a radiation can be suppressed, the mutual coupling can be reduced as well. Placing a kind of absorber between the elements could be a simple solution to absorb the spurious radiation. However, the effect of placing the absorber in the near-field introduces dissipation loss and reduces gain. A different approach could be placing an electric wall between the elements such that the electric wall can shield an element from the radiation of the next element. In planar technology, this can be approximated by reshaping the ground plane as an electric wall in case that the array is designed in one plane.

As can be seen in the U-shaped PCMA in Fig. 3.26(e), the U-shaped reflector could be the shield between two elements. In order to prove this concept, a scenario to visualize the mutual coupling is developed using simulations for two arrangements of two coupled elements, seen in Fig. 3.27(a) and Fig. 3.27(b).

Fig. 3.27(a) shows the model of a two-element PCMA where the elements are separated by a spacing of x=46 mm. The mutual coupling between them is expressed as the transmission S-parameter S_{21}. The S_{21} can be calculated by exciting the first element while loading the second element with 50 Ω impedance. In Fig. 3.27(a), this figure represents the distribution for frequency 5 GHz of the x-directed electric field E_x. This electric field component is assumed to be the main radiation component which stimulates the mutual coupling. The visualization shows the second circular disk induced by the radiation from the first element which further generates the current flowing through the feeding line of the second element.

(a)

(b)

(c)
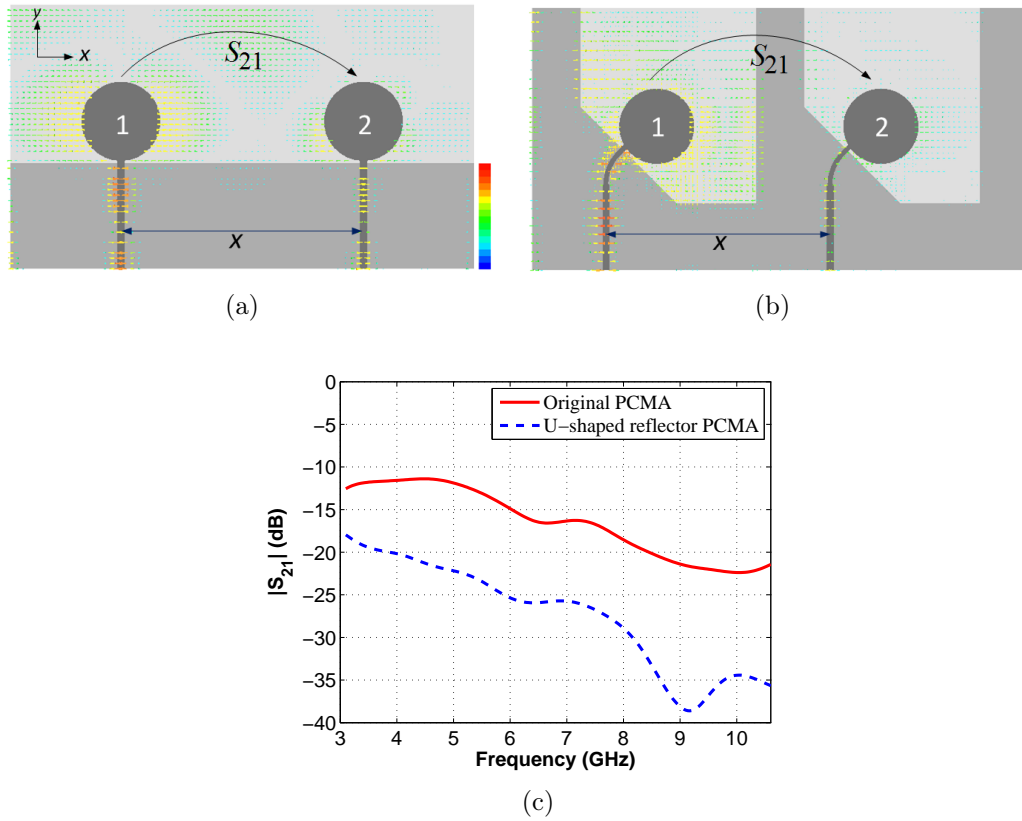
Figure 3.27: Representation of mutual coupling in double PCMA (a)E_x of original PCMA (b)E_x of U-shaped reflector PCMA (c)Coupling coefficients of the original PCMA and the U-shaped reflector PCMA

By applying the same scenario, the mutual coupling between the U-shaped PCMAs can be calculated as well. Fig. 3.27(b) shows a double U-shaped PCMA with spacing $x = 46$ mm. In order to calculate S_{21}, the first element is excited and the second element is terminated by 50 Ω impedance. Compared with the previous scenario, the coupling in the second element is strongly reduced due to the U-shaped wall. The wall is seen to shield the second element from the electric field E_x generated by the first element. The calculated coupling of both scenarios is shown in Fig. 3.27(c). The mutual coupling of the original PCMA is relatively high with the maximum value of the transmission S-parameter is -12 dB at the lower part of the frequency band. On the other hand, the average mutual coupling of the two-element U-shaped PCMA is reduced by -10 dB compared with the coupling of the original PCMA.

According to these scenarios, the contribution of the U-shaped ground plane to suppress the coupling between PCMAs can be seen clearly. The U-shaped reflector can not only be utilized to generate broadside radiation but also can be used to suppress the mutual coupling between two elements. Therefore, the motivation was to design the U-shaped reflector PCMA as the element of a UWB linear array antenna, which was investigated in the following chapter.

4 Ultra-Wideband Printed Circular Monopole Antenna Array

This chapter presents a design of directive printed circular monopole antenna array (PC-MAA). Firstly, the radiation pattern of a PCMAA with the original shaped PCMA element (later termed as original element) is demonstrated. Then, the radiation pattern of a PCMAA with the U-shaped PCMA is shown. The active impedance of these array antennas is included in the discussion as well. Secondly, a design of an equal split one-to-four T-Junction power divider as a feed network for the four U-shaped element PCMAA is presented. Finally, the simulation of the antenna with the feed network is shown and is validated by measurement. In order to obtain a physical insight of a beam-scanning pattern of this antenna array, a design of the four U-shaped element PCMAA integrated with a set of delay lines is presented and closes this section.

4.1 Printed Circular Monopole Antenna Array (PCMAA)

Antenna arrays are widely realized for narrow frequency band applications. However, the number of investigations related to broadband applications is still limited. A general problem faced in designing a wide-band array antenna is the mutual coupling of neighbouring elements which alters the antenna input impedance over the entire frequency band. The input impedance of the elements can spuriously change over frequency. To achieve impedance matching over the whole frequency band, the reflection coefficient of the array is optimized based on the active impedance concept.

The design of UWB linear array antennas by using planar radiator elements can be categorized based on two arrangement topologies. The first type is that the radiator elements are positioned vertically and the feed network is arranged in an orthogonal plane. The second type is the so called planar topology where the radiator elements are positioned horizontally in the same plane as the feed network. These two topologies have been been presented in several publications. An example of array designs using the vertical topology can be found in [52] while an array design based on the planar topology for the frequency range of 8-12 GHz has been presented in [53]. With respect to the feature size, the planar topology offers more compact geometry than the vertical topology. By considering this benefit, the design of planar topology becomes the focus of this research work especially for the operating frequency band of 3.1 to 10.6 GHz.

4.1.1 Four-element printed circular monopole antenna array

As discussed in chapter 2, the input impedance of elements in an array antenna deviate from the input impedance of a single element due to mutual coupling. Therefore, the reflection coefficient of the array antenna is not calculated based on the reflection coefficient of the single isolated element, but the reflection coefficient is calculated based on the concept of active impedance, based on the reflection coefficient of elements in the array by considering the presence of mutual coupling.

In case of a very large array antenna, e.g, an antenna for satellite communication system, it takes high effort to calculate the active impedance of every element. Therefore, the active impedance is calculated based on few elements at certain positions in the array. In addition, the active impedance of a very large array antenna can be approximated by an *infinite array*. In such an approach, for broad side radiation, the elements are assumed to be enclosed by magnetic and electric walls. Hence, the active impedance is approximated by the reflection coefficient of a single element enclosed by magnetic and electric walls.

On the other hand, the active impedance of each element in a small array antenna can readily be calculated. Indeed, the calculation can be simplified as well since the active impedance of an element can be the same as the active impedance of certain neighboring elements due to symmetry. In this case, it is not necessary to calculate the active impedance of every element.
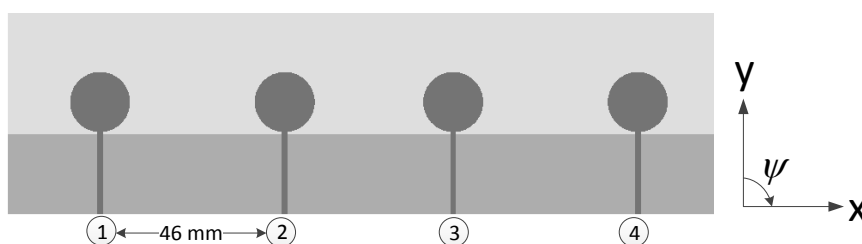
Figure 4.1: Four-element PCMAA

In order to describe the active impedance concept, a simulation of the active impedance of a four 'original' element PCMAA is demonstrated where the scenario is shown in Fig. 4.1. The four PCMAs are uniformly spaced by 46 mm. The antenna array is simulated by the scenario of using Duroid 5870 substrate, with $\epsilon_r = 2.33$, thickness $t = 0.5$ mm; the four ports of the PCMAA are excited by a uniform amplitude. The simulation result of the active impedance can be seen in Fig. 4.2.

Due to the symmetrical geometry of the array, it is apparent that the active impedance of the outer side elements, namely the 1st and the 4th elements, are equal. On the other hand, the active impedance of the inner side elements, namely the 2nd and the 3rd elements, are obviously equal as well. It is evident that the reflection coefficient of the elements over a certain frequency range strongly degrade from the isolated reference element, which is matched better than -10 dB. The reflection coefficient of the inner elements seems higher

Figure 4.2: Active impedance of four PCMAs

(a) 1st element

(b) 2nd element

(c) 3rd element

(d) 4th element

Figure 4.3: Element pattern of four PCMAs on azimuth plane

than the reflection coefficient of the outer elements since the inner elements suffer more electromagnetic coupling than the outer elements. This simulation describes the essential information of the active impedance concept in order to design UWB array antennas.
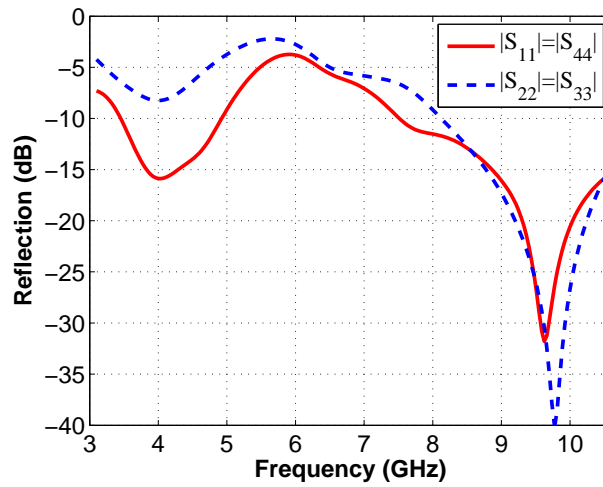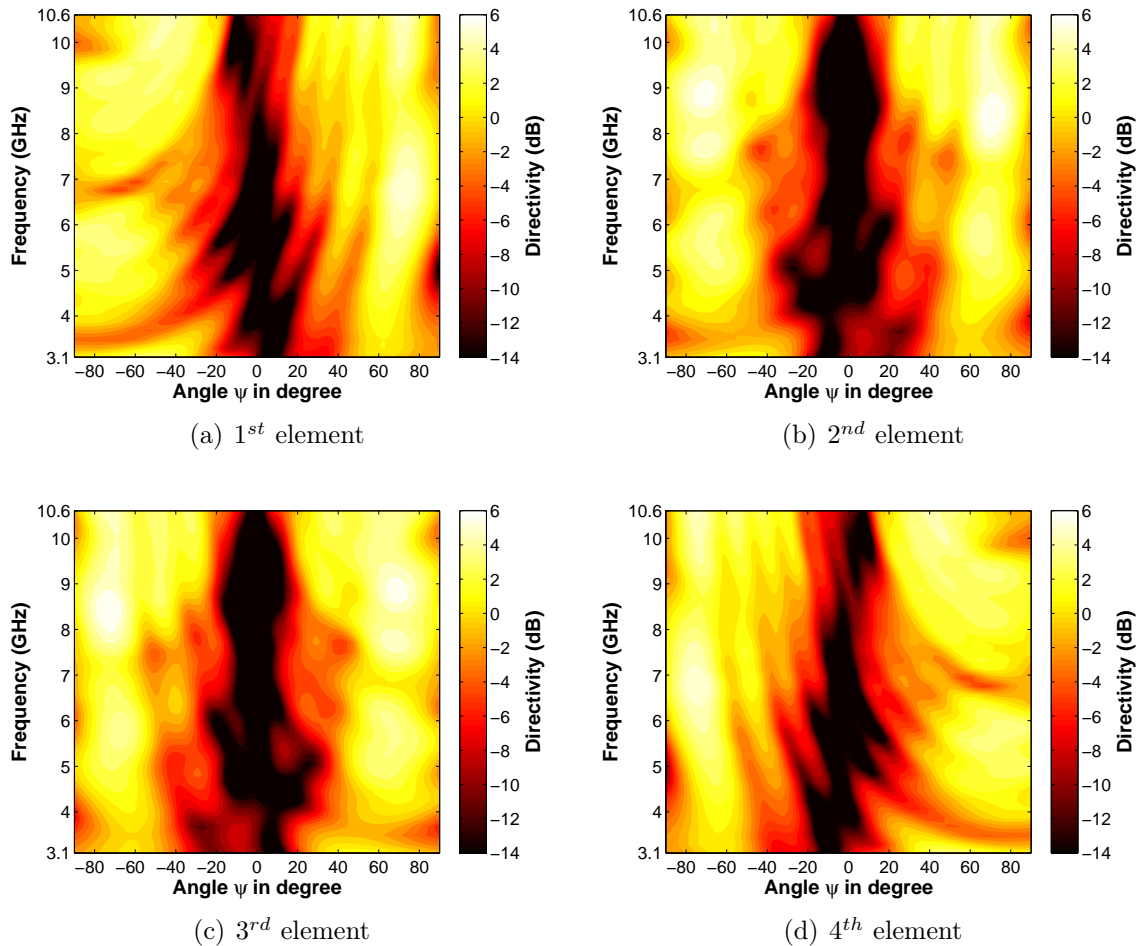
It is subsequently of high interest to observe the spurious effect of the mutual coupling on the radiation pattern of the elements. Therefore, an examination of element patterns is presented by using the full-wave analysis where the simulation results are shown in Fig. 4.3(a) to Fig. 4.3(d). The simulations are presented in the frequency range of 3.1 to 10.6 GHz and the spatial observation is taken in the range of azimuth angle -90° to 90°. The spurious effect of the mutual coupling can be clearly identified from the plots. Also, the element patterns can be distinguished as the element pattern of the inner elements and the element pattern of the outer elements. The 1st and the 4th element patterns are seen exactly symmetrical while the 2nd element pattern is perfectly symmetrical in comparison with the 3rd element pattern.

One purpose of calculating the element pattern is to plot the array pattern based on the concept of pattern multiplication. This concept can be an alternative to calculating the pattern of an array antenna instead of using EM-field analysis since some problems corresponding to time and numerical cost can be faced in the full-wave analysis of a large array antenna. Therefore, such a practical method is effective to assess the pattern of an array antenna rigorously. Based on the concept of pattern multiplication, the pattern of a linear array antenna can be calculated according to the element pattern and the array factor which is expressed as

$$E\left(\psi\right) = \frac{1}{\sqrt{N}} \sum_{n=1}^{N} f_n\left(\psi\right) \; exp\left[j\left(kd\left(n-1\right)\sin\psi\right)\right] \qquad (4.1.1)$$

where $f_n\left(\psi\right)$ denotes the element pattern of the nth element and d is the uniform spacing between the elements.

(a) Based on pattern multiplication   (b) Based on full-wave analysis
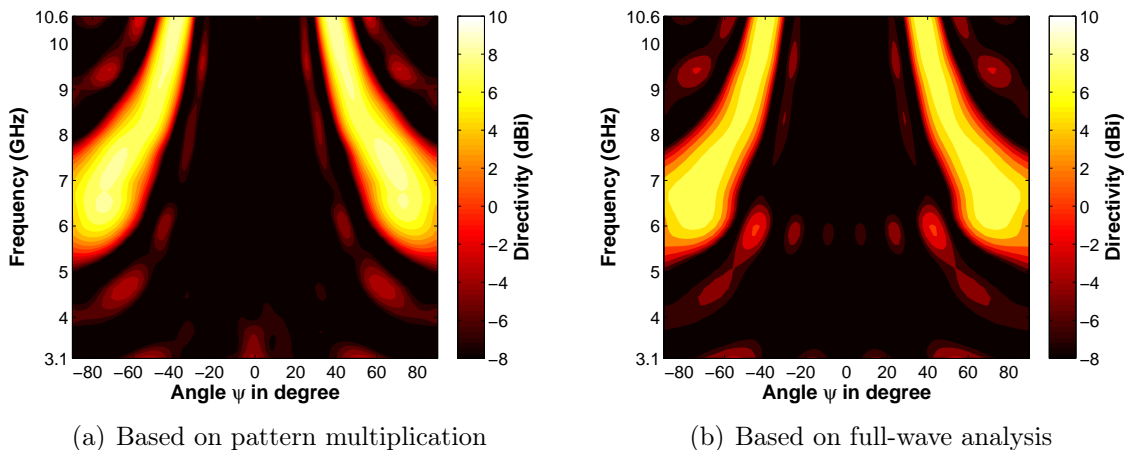
Figure 4.4: Pattern of the four-element PCMAA on azimuth plane

To apply the concept in the UWB frequency range, the pattern of the four-element PC-MAA is calculated based on equation (4.1.1). The element patterns described in Fig. 4.3(a) to Fig. 4.3(d) substitute the variable $f_n(\psi)$. Fig. 4.4(a) shows the result of such a semi full-wave analysis. It is seen from the plot that a double beam pattern is generated on the azimuth plane. This characteristic is effected by the the single element pattern with a null in broadside in combination with the grating lobes of the array configuration. Moreover, the grating lobes seem appearing in the plot, recognized by the higher directivity part. The grating lobes raise due to the relatively large spacing between the elements compared to the free-space wavelength at the highest frequency. Since the elements are uniformly spaced by 46 mm, the grating lobes at the end-fire direction rise at 6.5 GHz while the grating lobes appear at $\pm 53°$ at the upper limit of the frequency band.

To validate this semi full-wave analysis, the pattern is compared to the simulation result of a complete full-wave analysis which is presented in Fig. 4.4(b). In this case, the four element PCMAs are excited simultaneously. It is seen that the two patterns show a reasonably good agreement. The directivity peaks as well as the position of the grating lobes seem to be nearly identical. Therefore, the pattern multiplication concept can be accepted as an alternative to calculate the pattern of UWB antenna arrays.

4.1.2 Four U-shaped element printed circular monopole antenna array

Based on the full-wave analysis, the four-element PCMAA is found to generate a pattern without broadside beam and the active impedances do not achieve the matching limit of -10 dB. As discussed in the previous chapter, the U-shaped PCMA offers some benefits compared to the original PMCA as it provides a broadside directive pattern and generates considerably low mutual coupling. Considering these advantages, the next step to be taken is to realize a UWB linear array antenna by using this element. The active impedance of the radiators is first optimized to fit the array antenna. The specified three strategies which deal with achieving impedance matching described in chapter 3 were implemented in the element design.

The layout of U-shaped printed circular monopole antenna array is shown in Fig. 4.5. The matching circuits: the shunt-stub, the modified transition stub and the pin-stub are seen in the design where their feature sizes and positions have been optimized in the full-wave analysis. The simulation result of the active impedance reflection coefficient can be seen in Fig.4.6. The active impedance of all elements seem different due to the unsymmetrical element geometry. However, they show satisfying reflection coefficients better than -10 dB thus we expect the elements completed with feed network will match for the frequency range of interest.

On the other hand, the simulation of active element pattern shows an interesting phenomenon. As can be seen in Fig. 4.7(a) to Fig. 4.7(d), the element patterns seem to be nearly identical with each other which is significantly different from the simulation of the
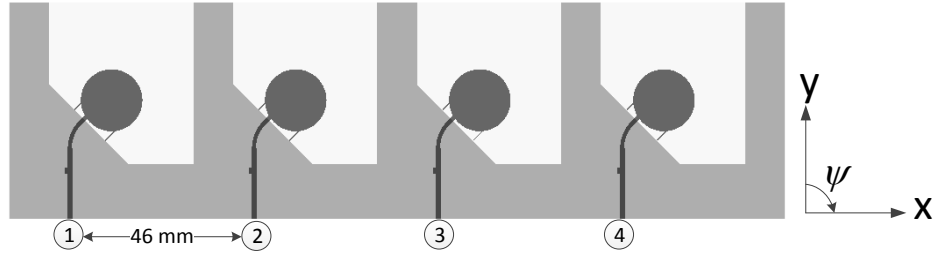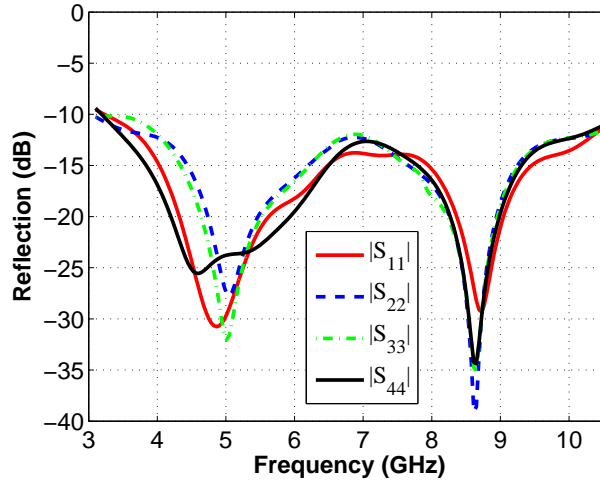
Figure 4.5: Four-element *U*-shaped PCMAA

Figure 4.6: Active impedance of four *U*-shaped PCMAs

four original element PCMAA. Such an identical pattern is mainly attributed to the relatively low mutual coupling in the array which, on the other hand, becomes an advantage in the design. In addition, the element patterns show a typical broadside directive pattern in particular within the direction ±45°.

The pattern of the four *U*-shaped element PCMAA simulated by using the full-wave analysis is described in Fig. 4.8 which shows a 3D pattern at an observed frequency of 5.6 GHz. It is seen that a quasi fan-shaped pattern is generated by the PCMAA with relatively small beamwidth in broadside direction. Such a typical directive pattern could be implemented in some commercial applications which require directive radiation patterns, for example in localization systems and transportation systems. The directivity of the four-element PCMAA in the elevation and azimuth plane can be seen in Fig. 4.9(a) and Fig. 4.9(b) respectively. As shown in Fig. 4.9(a), the directivity in the elevation plane seems uniform over the spatial direction. On the other hand, the beamwidth of the azimuth pattern strongly varies over frequency as can be seen in Fig. 4.9(b). The beamwidth is calculated as 30° at the lower limit of the frequency band and decreases to 8.8° at the upper limit of the frequency band.

A variation of beamwidth over frequency is a general phenomenon in antenna array theory. Such a variation needs to be considered in any application since the spatial distribution of

(a) 1st element

(b) 2nd element

(c) 3rd element

(d) 4th element
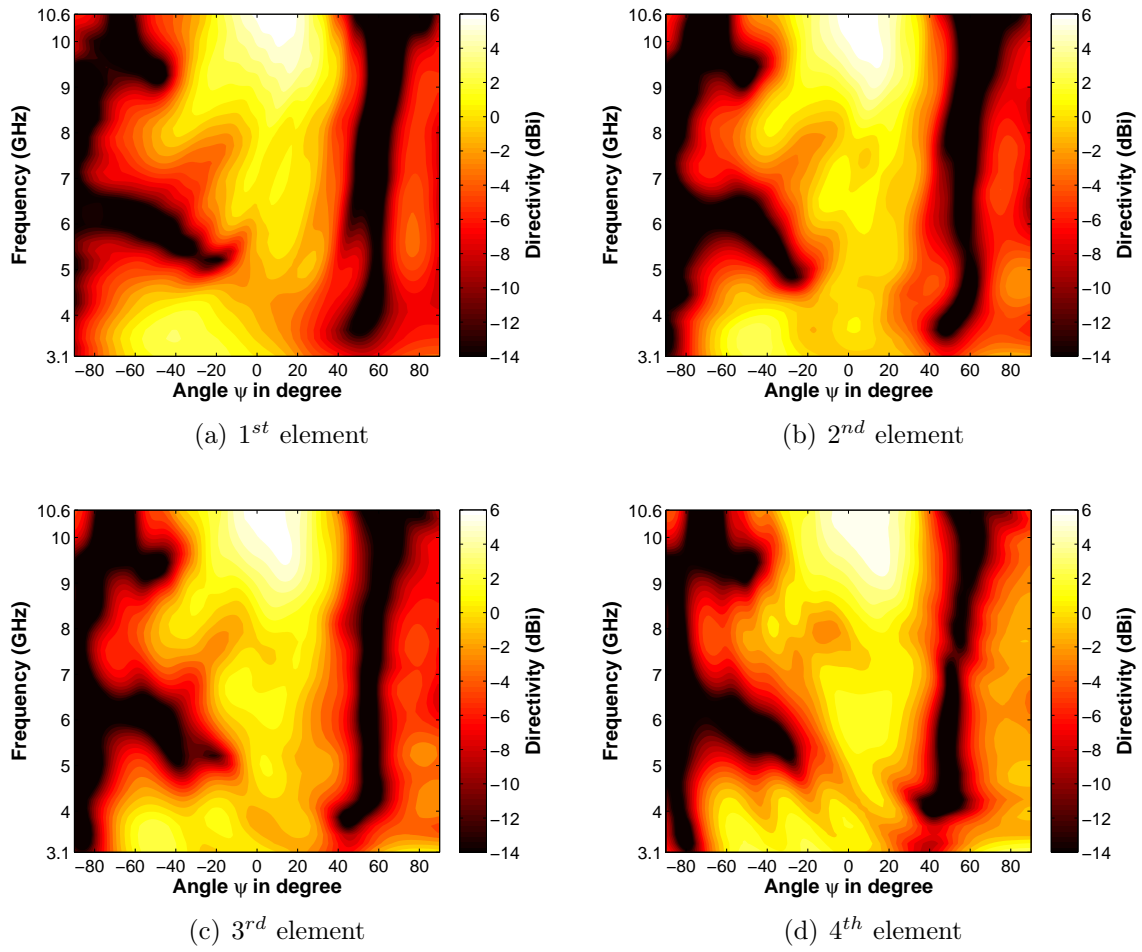
Figure 4.7: Element pattern of U-shaped PCMAs on the azimuth plane

side view

front view
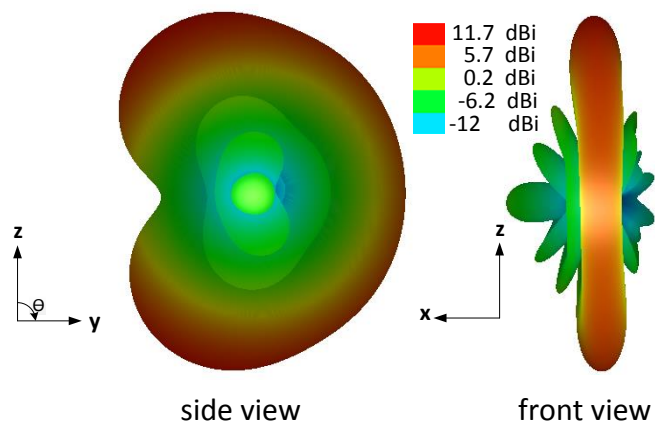
Figure 4.8: 3D fan-shaped pattern of four-element U-shaped PCMAA at 5.6 GHz

(a) Elevation plane

(b) Azimuth plane
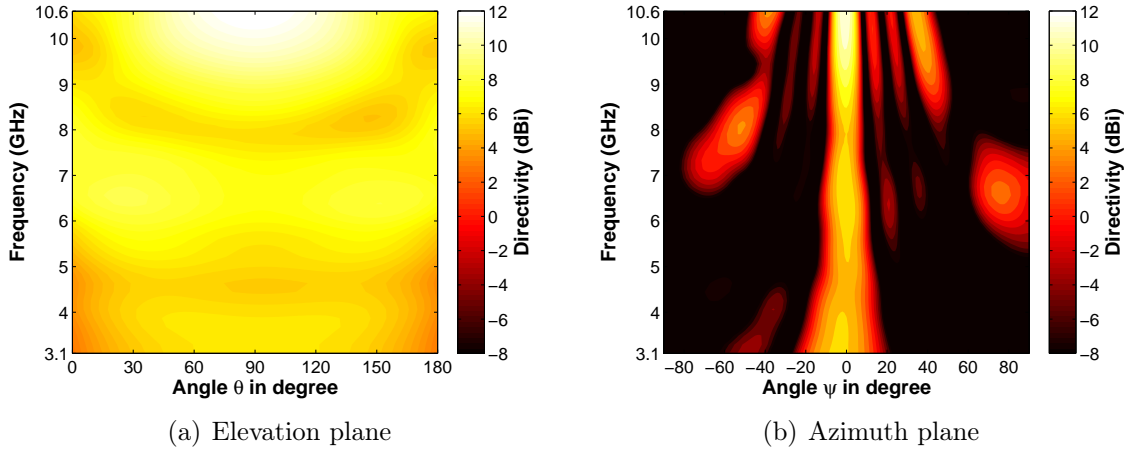
Figure 4.9: The pattern of four U-shaped element PCMAA

the radiated power is changed over frequency. The beamwidth is in particular a property which determines the resolution of localization systems, e.g, radar systems. One solution to the problem will be discussed in detail in chapter 5 and 6 by applying a set of low pass filters to the U-shaped element PCMAA to create a frequency independent beamwidth.

4.1.3 Time domain pattern of U-shaped PCMA array

The time domain patterns of the four-element U-shaped PCMA array calculated based on inverse Fourier transform are illustrated in Fig. 4.10(a) and Fig. 4.10(b).

(a) Elevation plane

(b) Azimuth plane
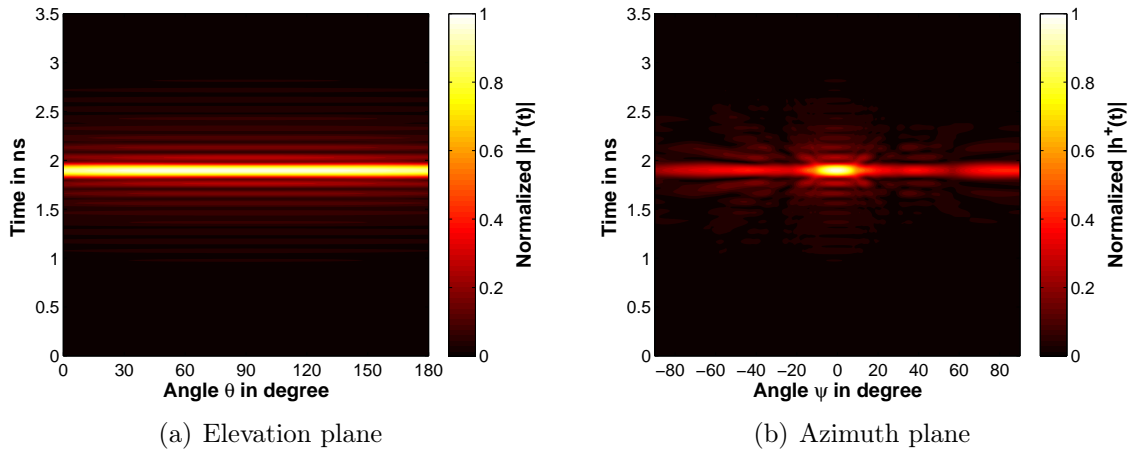
Figure 4.10: The time domain patterns of four U-shaped element PCMA array

The time domain pattern in the elevation plane is shown in Fig. 4.10(a). This figure describes an omni directional pattern which is corresponding to the quasi *fan shaped*
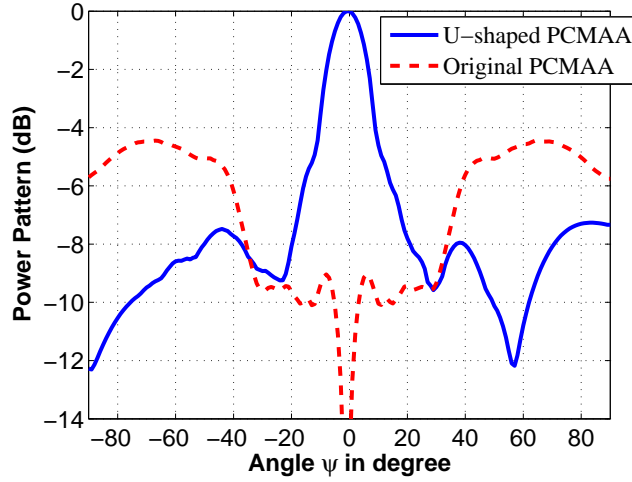
Figure 4.11: Snapshot of time domain patterns of original element PCMA array and *U*-shaped element PCMA array

pattern in the frequency domain. The pulse magnitude on this plane is seen nearly uniform within the elevation direction 0° to 180°. On the other hand, the time domain pattern in the azimuth plane is illustrated in Fig. 4.10(b). The pattern is seen to be focused on the broad side direction. This directive pulse is strongly contributed by the the array factor and the *U*-shaped element pattern.

Fig. 4.11 shows the snapshot of the pulse power pattern of the *U*-shaped element PCMA array in comparison with the original element PCMA array in the azimuth plane. It is evident that the pulse beam is focused to the broadside and the peak of the pulse increases by approximately 4.3 dB due to the modification of the original PCMA element.
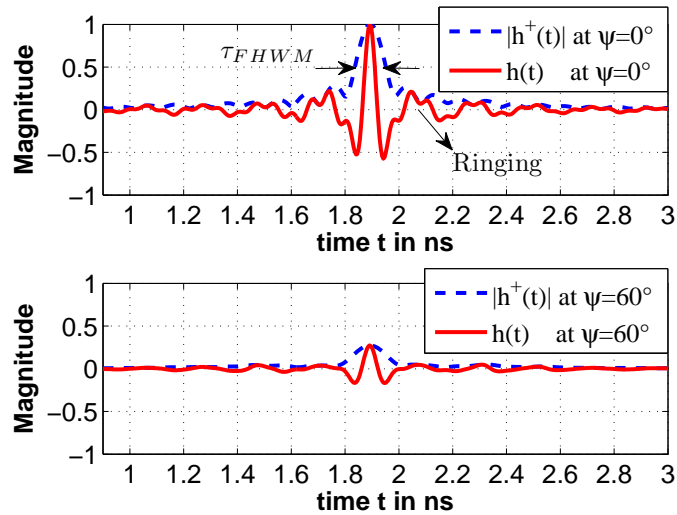
Figure 4.12: Impulse response of PCMA array at 0° and 60°

Fig.4.12 shows the impulse response of the PCMA array at azimuth angles of 0° and 60°. The pulse peak at 60° is seen approximately 73 % lower than the peak at broadside. The pulse width τ_{FHWM} and the ringing time $\tau_{\text{r},0.22}$ at broadside are 150 ps and 120 ps respectively. These values are comparable with the width of the full pulse at half maximum and the ringing time of the other antennas shown in [6].

4.2 UWB T-Junction power divider for UWB array antennas

The four-element PCMAA will be excited through a single input connector. Thus, a feed network realized as one-to-four power divider is required to feed the printed monopole array. The feed network is designed to transfer uniform power to the four outputs and the reflection coefficient at the input connector is required to be better than -10 dB over the UWB frequency range. The T-Junction power divider is chosen for the feed network since it provides a simple structure without additional lumped elements.

A T-Junction is a simple three-port network that can be used for power division or power combination [46]. A transmission line model of the T-Junction power divider is shown in Fig. 4.13. The relation of characteristic impedance Z_0 at the input with Z_1 and Z_2 at the
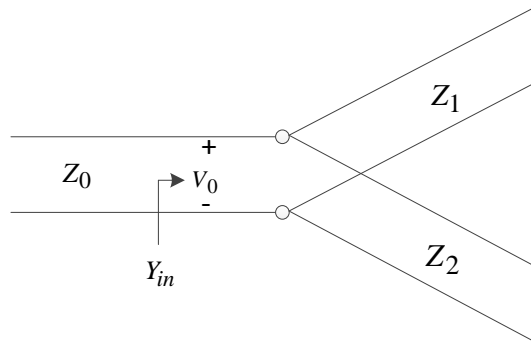
Figure 4.13: Transmission line model of T-Junction power divider

outputs is given as

$$\frac{1}{Z_0} = \frac{1}{Z_1} + \frac{1}{Z_2}.$$
(4.2.1)

The relation between the input power P_{in} with the output power P_{out1} and P_{out2} is

$$P_{in} = P_{out1} + P_{out2}.$$
(4.2.2)

For an equal split power divider, a power division of the outputs by 1:1 is needed. Hence, the output voltage V_1 and V_2 are

$$V_1 = V_2 = V_0$$
(4.2.3)

where V_0 denotes the voltage of the input transmission line. Furthermore, equation (4.2.2) can be written as

$$\frac{V_0^2}{Z_0} = \frac{V_0^2}{Z_1} + \frac{V_0^2}{Z_2}. \tag{4.2.4}$$

Since $Z_1 = Z_2$, the relation of output-to-input impedance is expressed as

$$Z_1 = Z_2 = 2Z_0. \tag{4.2.5}$$

Based on equation (4.2.5), the input impedance of 50 Ω is corresponding to the impedance of 100 Ω at the output. However, the output ports will be connected to the radiators with a 50 Ω feeding line. Thus, a microstrip line transformer is needed to transform the characteristic impedance of 100 Ω to 50 Ω.

A quarter-wave length transformer is widely used to match two transmission lines for narrow frequency band applications. The main principle is that an additional transmission line by the length of $\lambda/4$ with respect to the operating frequency is inserted between the two transmission lines. However, the quarter wavelength transformer is not appropriate to be implemented in broadband systems. Therefore, a broadband transformer is designed to match two transmission lines for a wide band application.

4.2.1 The theory of broadband T-Junction

Some concepts of broadband transformer are given in [46], namely *binomial* matching transformers and *chebyshev* matching transformers. In this work, the *chebyshev* transformer is used as the broadband transformer since it provides a broader relative bandwidth than the binomial matching transformer of the same order.
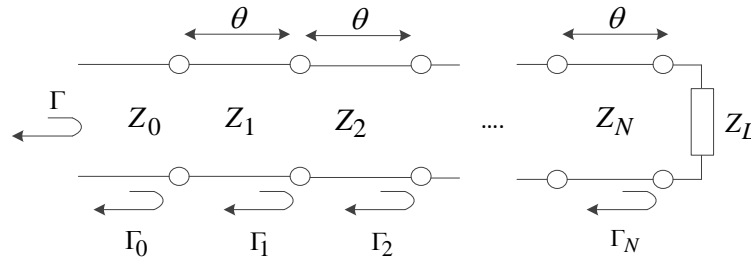
Figure 4.14: Multi-section transformer

The broadband transformer concept is repeated in the following based on the theory of multi-section transformer as described in Fig. 4.14. As seen in the picture, the transformer consists of N-equal length transmission lines with electrical length $\theta = \beta l$, where $l = \lambda/4$ at the center frequency. The impedance of corresponding sections are denoted as Z_1, Z_2 to Z_N respectively. In addition, the partial reflections are represented as Γ_0, Γ_1, Γ_2 and Γ_N. The transformer is designed to match the load impedance Z_L to the impedance Z_0.

For N even, the total reflection coefficient $\Gamma\left(\theta\right)$ is derived as

$$\begin{aligned}\Gamma\left(\theta\right) =&2e^{-jN\theta}\left[\Gamma_0\cos N\theta + \Gamma_1\cos(N-2)\theta + \cdots\right.\\ &\left.+\Gamma_n\cos(N-2n)\theta + \cdots + \frac{1}{2}\Gamma_{N/2}\right]\end{aligned} \tag{4.2.6}$$

whereas for N odd

$$\begin{aligned}\Gamma\left(\theta\right) =&2e^{-jN\theta}\left[\Gamma_0\cos N\theta + \Gamma_1\cos(N-2)\theta + \cdots\right.\\ &\left.+\Gamma_n\cos(N-2n)\theta + \cdots + \Gamma_{(N-1)/2}\cos\theta\right].\end{aligned} \tag{4.2.7}$$

A *Chebyshev* transformer is designed by making $\Gamma\left(\theta\right)$ proportional to the Nth *Chebyshev* polynomial T_N

$$\Gamma\left(\theta\right) = Ae^{-jN\theta}T_N\left(\sec\theta_m\cos\theta\right) \tag{4.2.8}$$

and

$$\sec\theta_m \approx \cosh\left[\frac{1}{N}\cosh^{-1}\left(\left|\frac{\ln Z_L/Z_0}{2\Gamma_m}\right|\right)\right], \tag{4.2.9}$$

where A is a constant and Γ_m is the maximum allowable value of the reflection coefficient. Moreover, θ_m represents the the maximum value of θ with respect to Γ_m and T_N is extracted as a function of $\sec\theta_m\cos\theta$. In case of a four-section transformer which will be shown in this work, the 4th order polynomial is expressed as

$$T_4\left(\sec\theta_m\cos\theta\right) = \sec^4\theta_m(\cos 4\theta + 4\cos 2\theta + 3) - 4\sec^2\theta_m(\cos 2\theta + 1) + 1. \tag{4.2.10}$$

Furthermore, the bandwidth Δf is defined as

$$\frac{\Delta f}{f_0} = 2 - \frac{4\theta_m}{\pi} \tag{4.2.11}$$

where f_0 is the center of frequency band. The relation between the characteristic impedance of the nth section Z_n and the partial reflection coefficient Γ_n is expressed as

$$\Gamma_n \approx \frac{1}{2}\ln\frac{Z_n+1}{Z_n} \tag{4.2.12}$$

In order to match the load Z_L to Z_0, the values of N and Γ_m are firstly determined. Then, the achievable bandwidth can be assessed from (4.2.11). Furthermore, the impedance of each section can be obtained from equations (4.2.6) to (4.2.8) and equation (4.2.12).

The above analysis is derived in [46] based on the theory of *small reflection*. A more practical procedure to design a *Chybeshev* transformer can simply use the impedance ratio table of *Chebyshev* transformers which provides the normalized impedance of the transmission lines.

Fig. 4.15 illustrates a schematic design of a four-section microstrip line transformer to match the transmission line of 50 Ω to 100 Ω. The characteristic impedance of sequential
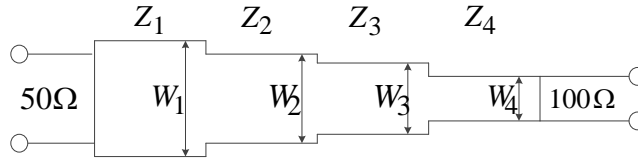
Figure 4.15: Microstrip line multi-section transformer

sections are denoted as: Z_1, Z_2, Z_3 and Z_4. In this design, the allowable reflection coefficient $\Gamma_m = 0.05$ and $Z_L/Z_0 = 2$ are assumed. From equations (4.2.9) and (4.2.11), θ_m is obtained 35.14° which results in a fractional bandwidth of 122 %.

The transformer was designed based on the *Chebyshev* impedance ratio table [46] where the impedance ratio of a four-section *Chebyshev* transformer for $\Gamma_m = 0.05$ is shown in table 4.1. Based on this table, the impedance of the four sections can be obtained.

Table 4.1: Impedance ratio of a four-section *Chebyshev* transformer for $\Gamma_m = 0.05$ and $Z_L/Z_0 = 2$

Z_L/Z_0	Z_1/Z_0	Z_2/Z_0	Z_3/Z_0	Z_4/Z_0
2.0	1.1201	1.2979	1.5409	1.7855

Table 4.2: The width of a four-section microstrip line *Chebyshev* transformer

W_1	W_2	W_3	W_4
1.20 mm	0.94 mm	0.68 mm	0.5 mm

The width of the corresponding section: W_1, W_2, W_3 and W_4 can be calculated from the impedance table by considering the parameter of Duroid 5870 substrate with $\epsilon_r = 2.33$ and thickness $t = 0.5$ mm where the result can be seen in table 4.2.

A broadband T-Junction power divider is realized by using two broadband *Chebyshev* transformers as depicted in Fig. 4.16. It can be seen that the *Chebyshev* transformers are inserted between the input and the outputs. Since there is no isolation between the output ports, the reflected signal can propagate from one output to the other. Therefore, the load at the output ports must be designed well matched.

The calculated S-parameters of this power divider, including material loss, with $\epsilon_r = 2.33$ and $\tan \delta = 0.0005$, are depicted in Fig. 4.17. The reflection coefficient at the input seems to be matched over the whole frequency band and the average transmission coefficient is approximately -3.2 dB. On the other hand, the isolation varies in the range of -5 dB to -8.5 dB.
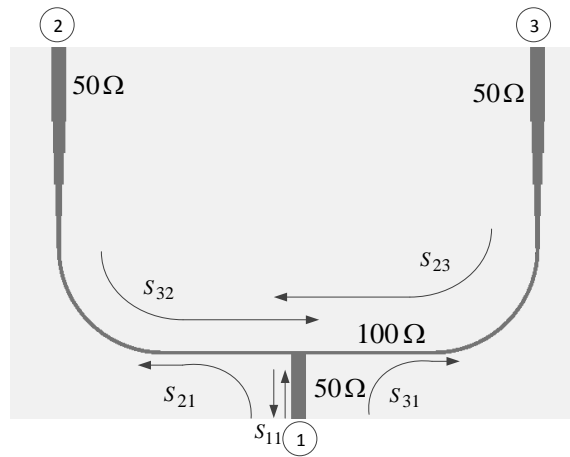
Figure 4.16: Layout of the broadband T-Junction power divider
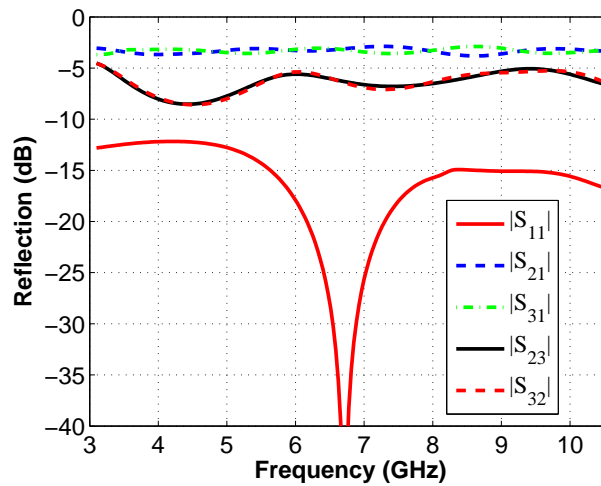
Figure 4.17: S-parameters of broadband T-Junction power divider

4.2.2 Two-stage T-Junction power divider

As the next step, a one-to-four power divider is designed by cascading the single broadband T-Junction. The layout of the cascaded power divider is shown in Fig. 4.18 where the uniform spacing between the outputs is kept to 46 mm. The simulation of the one-to-four power divider included material loss by using the full wave analysis shows satisfactory transmission and reflection S-parameter as shown in Fig. 4.19. The transmission S-parameter coefficients show a flat magnitude response around -6.3 dB. In addition, the reflection coefficient shows a -10 dB match bandwidth from 3.1 GHz to 10.6 GHz.
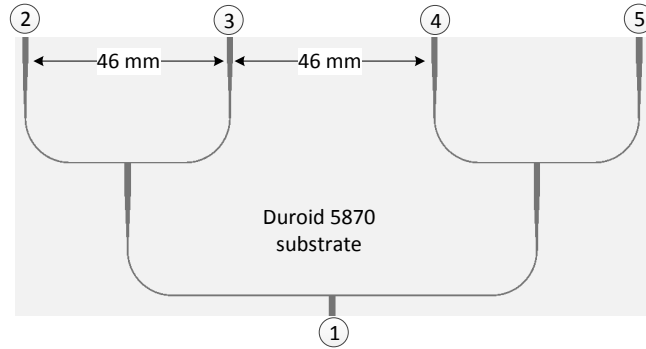
Figure 4.18: Layout of two-stage T-Junction power divider
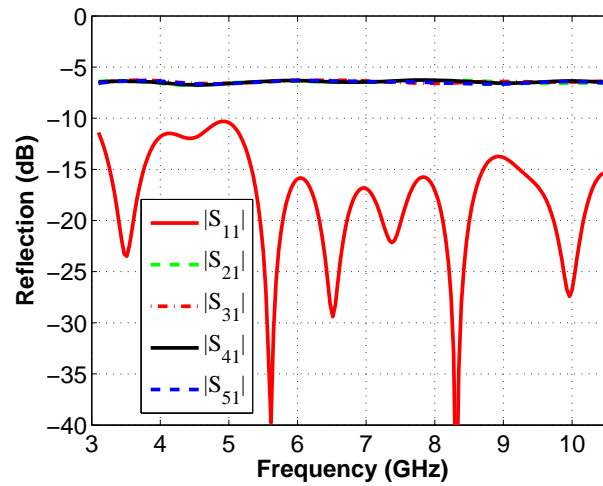
Figure 4.19: S-parameters of two-stage broadband T-Junction power divider

4.3 Fabricated four-element UWB printed circular monopole antenna array

4.3.1 The fabricated PCMAA

As the final step of the design, the feed network is used to feed the four-element PCMAA as depicted in Fig. 4.20. As seen from the layout, the radiator elements and the feed network are etched on the top side of the substrate while the ground plane is etched on the bottom side. The in-house fabricated antenna depicted from the top and bottom view
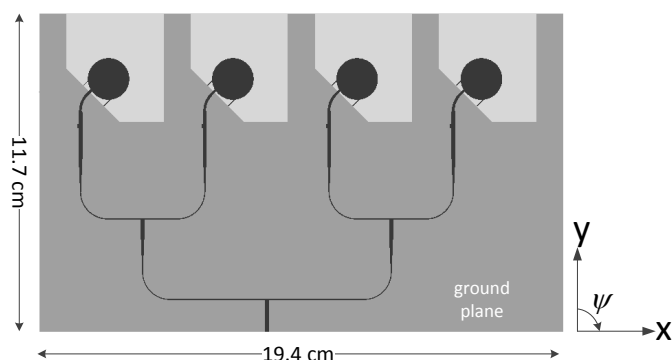
Figure 4.20: Layout of the four-element PCMAA with feeding network

perspectives can be seen in Fig. 4.21(a) and Fig. 4.21(b) respectively where the antenna has been etched on the Rogers RT/duroid 5870 substrate, with $\epsilon_r = 2.33$ and thickness $t = 0.5$ mm. The measurement result of the reflection coefficient is shown in Fig. 4.22. In

(a) Top-side perspective

(b) Bottom-side perspective
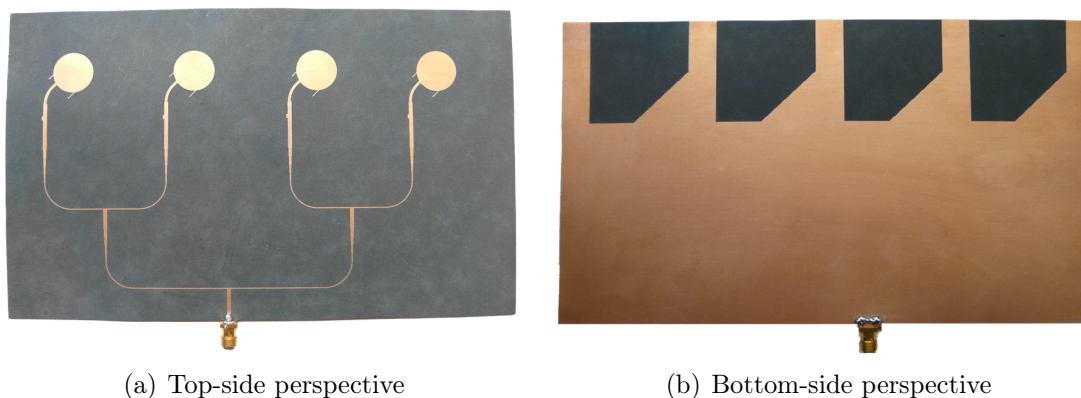
Figure 4.21: Fabricated PCMAA

comparison with the simulation result, the measurement shows a good agreement. The matching better than -10 dB is achieved over the UWB frequency range.

The antenna pattern measurement on the azimuth plane, reproduced as Cartesian and contour plots, can be seen in Fig. 4.23(a) and Fig. 4.23(b) respectively. The side lobe
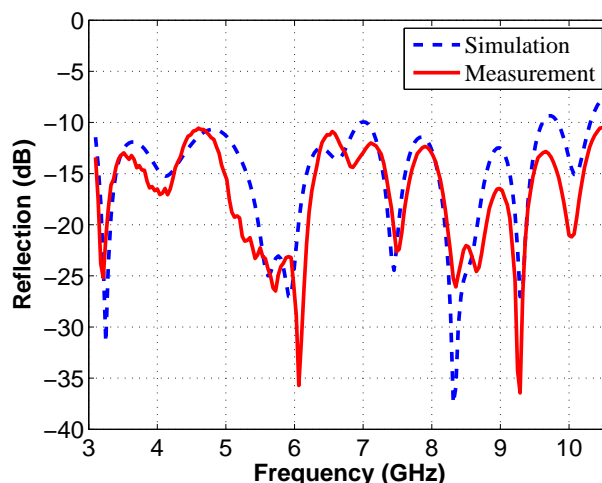
Figure 4.22: Reflection coefficient of the complete antenna and feed network

level seems to be asymmetrical. Based on antenna array theory, a uniform linear array antenna with uniform excitation generates symmetrical side lobes. In this design, the asymmetrical characteristic is mainly due to the titled circular radiator, as can be seen in Fig. 3.26(e) which generates an asymmetrical element pattern. However, the fabricated antenna provides a broadside directive pattern across the UWB frequency range which validates the previous simulation.

(a) Cartesian plot,co-polarization

(b) Contour plot, co-polarization
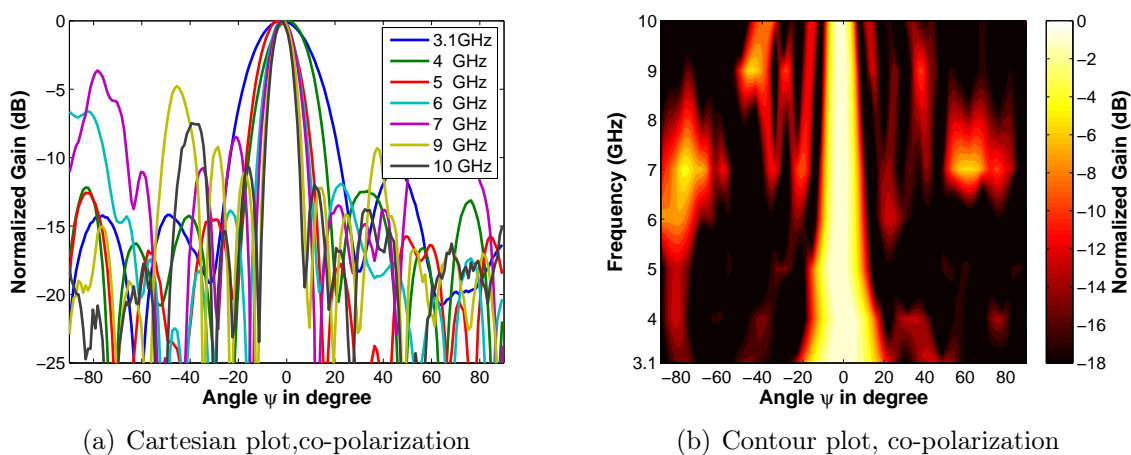
Figure 4.23: Measurement of radiation pattern on azimuth plane

4.3.2 Investigation of material losses

The antenna power loss is one property which is used to evaluate the performance of an antenna. One main source of loss is dissipation loss due to the material and this loss is a

function of the frequency. In the following, such a loss in the PCMAA is characterized by using post processing in the full wave analysis. The loss is assumed as the difference of the directivity and the IEEE Gain. The parameters of the substrate are: $\epsilon_r = 2.33$, $\tan \delta = 0.0012$ and the conductivity of the metal layer $\sigma = 5.8e7 \cdot 1/\Omega m$. The loss magnitude over the UWB frequency band can be seen in Fig. 4.24 where the loss seems to increase over frequency. At the lower limit of the frequency band the loss is approximately 0.3 dB while at the upper limit of the frequency range the loss approaches to 0.6 dB.
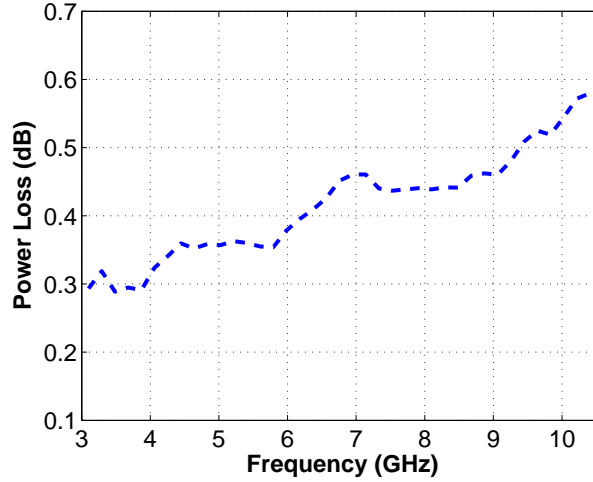
Figure 4.24: The magnitude of the power loss due to material losses over frequency

4.4 Time-delay beam scanning of printed circular monopole antenna array

Beam scanning techniques namely the phase shifter and the time-delay beam scanning have been briefly discussed in chapter 2. A time-delay network is widely used to realize a beam scanning for wide-band applications. It can be realized as a set of microstrip delay lines in planar technology. A planar time-delay feeding network is designed to illustrate a beam scanning of the PCMAA. In this scenario, the main beam for the whole frequency band would be scanned to a target angle of $22.5°$. The incremental length of the time delay as given in chapter 2

$$\Delta L = \frac{d \sin \theta_0}{\sqrt{\epsilon_r}} = 12.73 \, \text{mm}. \tag{4.4.1}$$

In order to minimize the feature size of the time delay, the microstrip line can be practically shaped as a so-called *worm quarter-circle* as shown in Fig. 4.25. The worm shaped consists of four quarter circles with radius R. The relation between R and ΔL is given as

$$R = \frac{\Delta L}{(2\pi - 4)}. \tag{4.4.2}$$

69
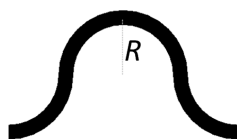
Figure 4.25: Worm quarter-circle microstrip line

Fig. 4.26 shows the layout of the four-element PCMAA integrated with the time-delay. The incremental length of the delay line can be recognized from the picture as the length increase from one element to the next element.
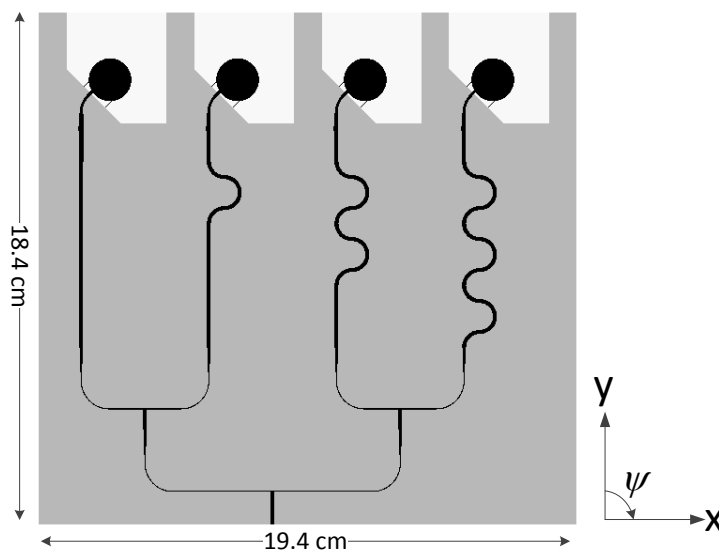
Figure 4.26: The layout of the PCMAA with time-delay

The radiation pattern of this antenna on the azimuth plane calculated by using the full wave simulator is shown in Fig. 4.27. It is clearly seen that the beam scan angle is fixed at 22.5° and that the beamwidth varies over frequency. In addition, according to equation (2.4.3) a grating lobe should appear at 4.7 GHz near $\psi = -90°$ if the beam is scanned to 22.5°. However, the grating lobes only appears at a higher frequency of approximately 7 GHz due to the contribution of the element pattern, as the directivity of the element patterns decays steeply towards the direction of -90°, compare Fig. 4.7.
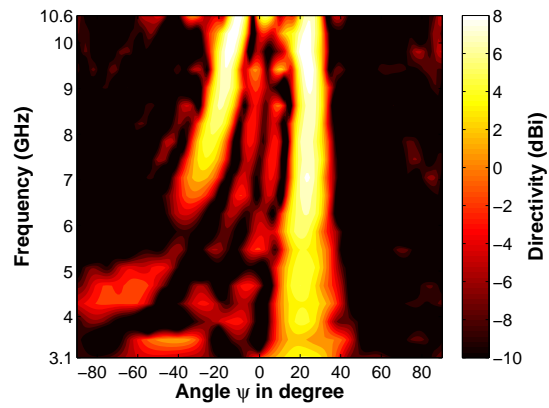
Figure 4.27: Azimuth radiation pattern of beam scanned PCMAA

5 Concept of Frequency Invariant Beam Pattern for UWB Antenna Arrays

This chapter applies the concept of the frequency invariant far-field beam pattern to a printed linear UWB antenna array. The theory of the broadband frequency invariant far-field sensor from the field of acoustics is adopted and applied to a discrete UWB printed circular monopole antenna array (PCMAA) for the frequency range from 3.1 to 10.6 GHz. Low pass filters (LPF) are employed to feed the individual elements of the PCMAA in order to establish an array of frequency invariant electrical width.

The discussion will be organized as following. Firstly, the concept of the frequency invariant far-field beam pattern will be presented. Secondly, the investigation is extended to the concept of frequency invariant beam scanning. Finally, the theory of the frequency invariant far-field beam pattern is applied to an eight-element PCMAA.

5.1 Basic concept of the frequency invariant far-field beam pattern

As previously demonstrated, the problem associated with an antenna array is that the pattern strongly varies across the frequency. With respect to UWB communication systems, this phenomenon becomes an important issue since the systems cover extremely large bandwidth. Some attempts have been made to achieve frequency invariant far-field beam patterns based on signal processing theory as well as based on a microwave theory. An example of a work related to this issue based on a microwave approach is a rectangular array of monopole antennas with integrated attenuators as the weighting factors applied to each element working across the 1.9-2.5 GHz frequency range [8]. Another example is a circular array of mono cone antennas which are fed by FIR filters for frequencies of 1.5-2 GHz [9]. In the following disscussion, a concept of achieving frequency invariant far-field beam pattern in the range of frequency 3.1 to 10.6 GHz is proposed.

One of the most attractive concepts of broadband far-field sensor has been developed in the frame of acoustic technology. The theory describes a discrete sensor array as an approximation of a continuous sensor in order to achieve a frequency invariant beam pattern [54]. The theory starts out from of a continuous distributed sensor which is

approximated in a discrete set of filtered broadband omni-directional array elements. The output of a linear continuous sensor aligned with the x-axis is defined as :

$$Z_f = \int\limits_{-\infty}^{+\infty} S(x, f)\rho(x, f)\, dx \qquad (5.1.1)$$

where $S(x, f)$ is the signal incident and received at a point x on the sensor due to the signal of frequency f, and $\rho(x, f)$ represents the receive sensitivity or gain at point x at frequency f. A sensitivity distribution (5.1.2) as given by a product of frequency f and a complex valued function G of xf can be shown to lead to

$$\rho(x, f) = fG(xf). \qquad (5.1.2)$$

The output of the sensor can then be represented as

$$Z_f = \int\limits_{-\infty}^{+\infty} S(x, f)fG(xf)\, dx. \qquad (5.1.3)$$

For a discrete array, the integral in (5.1.3) can be approximated by the numerical approximation, given as

$$\tilde{Z}_f = f \sum_{i=0}^{N-1} S(x_i, f)G(x_i f) \qquad (5.1.4)$$

where $\tilde{Z}_f$ represents the output of the discrete sensor array, N is the number of the discrete sensor elements, $S(x_i, f)$ is the sample signal received by sensor i at point x at frequency f, and $G(x_i f)$ represents the sensitivity (gain) function sampled at $x = x_i$.

The sensitivity function $G(x_i f)$ of a frequency invariant sensor at x_i is understood as the primary frequency response (or filter) at this point and is set equal to $H_x(f)$. Consider $H_{\gamma x}(f)$ is the filter response at point γx. For a linear array, due to linear phase progression

$$\begin{aligned} H_{\gamma x}(f) &= G(f\gamma x) \\ &= H_x(\gamma f) \end{aligned} \qquad (5.1.5)$$

and thus $H_x(f)$ at position x_i can be represented as

$$H_{x_i}(f) = H_{x_1}(x_i/x_1 f) \qquad (5.1.6)$$

Fig. 5.1 shows the block diagram of a broadband discrete linear array. The specific filter function up to this point has not been defined. In realization, low pass filters (LPF) are applied as the primary filter with cut-off frequency varying inversely to the position x in the linear array. This leads to frequency invariant beamwidth since the array aperture size is constant in terms of wavelength. Assuming the aperture length of a linear array is defined as $Pk_1\lambda$, where P is an integer, λ is the wavelength and k_1 is the fractional number
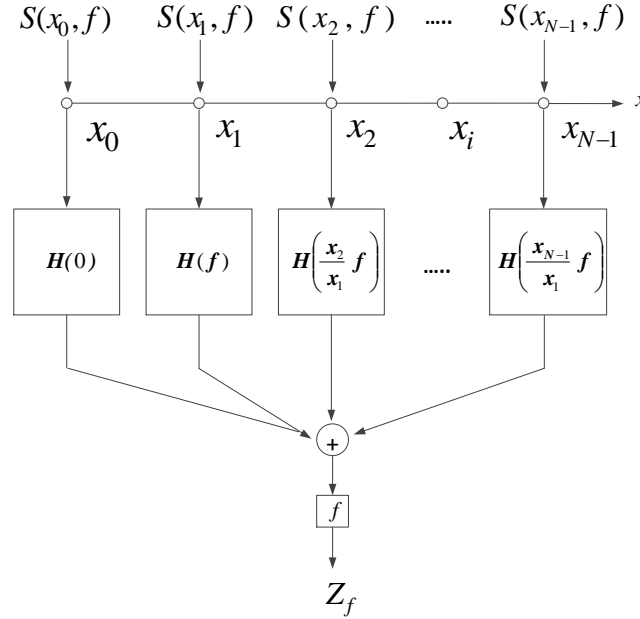
Figure 5.1: Block diagram of a discrete linear array with broadband pattern (origin at $x = 0$).

of the wavelength where $0 < k_1 \leq 1$, for $k_1 \in R$, the first sensor is located at $x = 0$; then, the position of the active sensor at the greatest position for the highest operating frequency is defined as

$$x_i = P k_1 \lambda_i \tag{5.1.7}$$

where i is the index of the active sensor of the greatest distance from the origin and λ_i is the wavelength corresponding to the highest operating frequency. At the sensor position larger than the aperture length corresponding to the highest operating frequency, the position of the sensor is given as

$$x_i = x_{i-1} + k_1 \lambda_i \tag{5.1.8}$$

In general, the position of the of the size $P k_1 \lambda$ can be summarized as follows:

$$x_i = \begin{cases} k_1 \lambda_U i, & \text{for } 0 \leq i \leq P; \\ P(k_1 \lambda_U)(\frac{P}{P-1})^{i-P}, & \text{for } P < i < N - 1; \\ P(k_1 \lambda_L), & \text{for } i = N - 1 \end{cases} \tag{5.1.9}$$

Where the λ_L and λ_U are the wavelength of the lowest frequency f_L and the highest frequency f_U respectively. According to the sensor position, the cut-off frequency of the LPF connected to sensor$-i$ is expressed as

$$f_i = \frac{P k_2 c}{x_i}, \; i \in \{0, 1, ..., N - 1\} \tag{5.1.10}$$

where c is the speed of light and N is the total number of the discrete sensors. We introduce the coefficient k_2 as the coefficient of the filter cut-off frequency that determines the length of the active sensor. If the value of k_2 is equal to k_1, the length of the active sensor at the wavelength λ is equal to $Pk_1\lambda$.

Figure 5.2: Antenna array with weighting elements

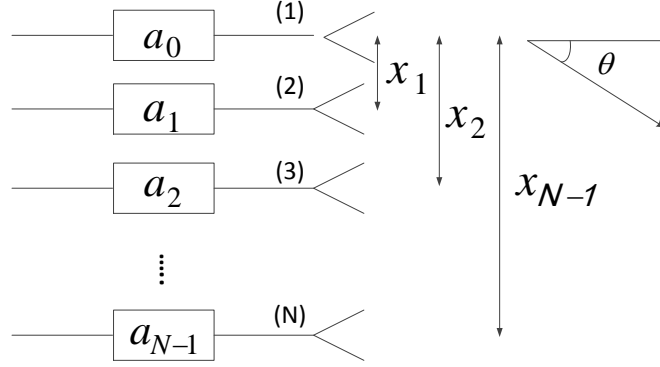The antenna array with frequency invariant beam pattern can be approximated as an array antenna with weighting functions as illustrated in Fig. 5.2. The antenna consist of N elements which are spaced non uniformly where x_1, x_2 and x_{N-1} are spacings from the 2nd, the 3rd and the Nth elements relative to the position of the first element. The radiator elements are weighted by complex weighting factors: a_0, a_1, a_2,..., and a_N. The normalized far-field pattern as the function of the frequency is defined as

$$E_{norm}(f,\theta) = \frac{1}{\sum_{n=0}^{N-1} |a_n(f)|^2} \sum_{n=0}^{N-1} a_n(f) exp\left[j\left(\frac{2\pi f}{c} x_n \sin\theta \right) \right]. \qquad (5.1.11)$$

By treating the LPFs as the weighting elements, the frequency invariant beam pattern of a linear array antenna can be designed.

In the following, a simulation based on this theory is shown. The parameters are chosen as: P=6, N=13, k_1=0.7, k_2=0.7, f_L=3.1 GHz, f_U=10.6 GHz. According to (5.1.9), this design results in partly uniform spacing and partly non-uniform spacing. The individual elements are spaced such as to just avoiding the arising of a grating lobe. As shown in Fig. 5.3(a) the individual spacing from the first to the 7th element, denoted as inner elements, is kept uniform while the individual spacing above the 7th, denoted as outer element, is non-uniformly distributed. All elements, with the exception of the 1st element are equipped with a feeding filter. As can be seen in Fig. 5.3(b), the cut-off frequency of the filters decreases as the element number increases. The 12th order Butterworth-type LPFs are assumed with the cut-off frequencies calculated based on equation (5.1.10), leading to a control of the number of active elements as function of frequency. As the result, the outer elements are active at the lower frequencies only while at 10.6 GHz the first up to the 7th element are active. The cut-off frequency of the feeding filter of the inner elements appears higher than the upper limit of the frequency band and these filters

(a) Sensor position
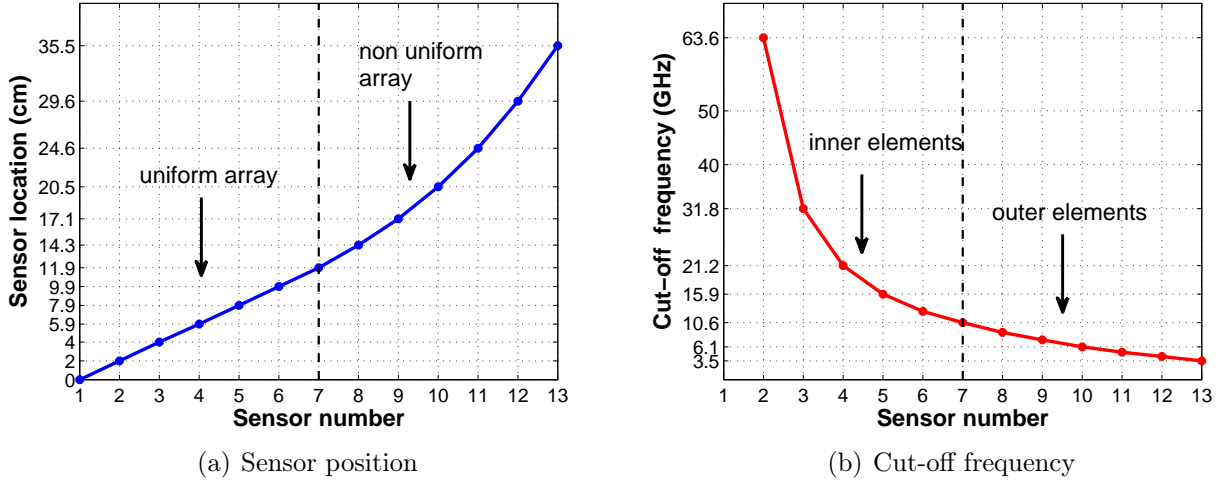
(b) Cut-off frequency

Figure 5.3: Sensor position and cut-off frequencies of frequency invariant linear array
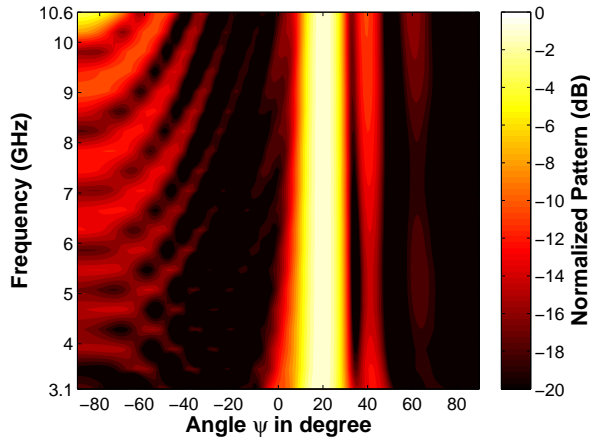
Figure 5.4: Frequency invariant beam pattern of 13-element linear array by using Butterworth-type LPF elements

have no significant contribution to deactivate the elements but the group delay of these filters contributes to keep the frequency invariant beam pattern.

Fig. 5.4 shows the normalized beam pattern for the UWB frequency range for the above design. The beamwidth seems to be constant across the UWB band and scanned to 19° which is due to the variation in the group delay of the filters (depending on cut-off frequencies); the beam scan can be compensated by insertion of suitable delay line as shown in the next section. The figure also shows an increased side lobe right to the main lobe which was found to be due to the phase error in the excitation of the array elements caused by the sloping variations in the LPF responses near cut-off frequencies. The single increased side lobe level is not present if idealized low-pass filters are used with abrupt cut-off behavior, as demonstrated in Fig. 5.5.

Figure 5.5: Frequency invariant beam pattern of 13-element linear array by using idealized filter functions

5.2 Procedure of controlling beam scanning

The concept of a discrete sensor array with position dependent filter functions has been theoretically successful to achieve a frequency invariant beam pattern. However, the group delay of Butterworth filters makes the filters to behave as a set of delay lines (time delay) which leads to a beam scanning, as shown in Fig. 5.4. On the other hand, a relation between the scan angle and the cut-off frequencies has been found. A f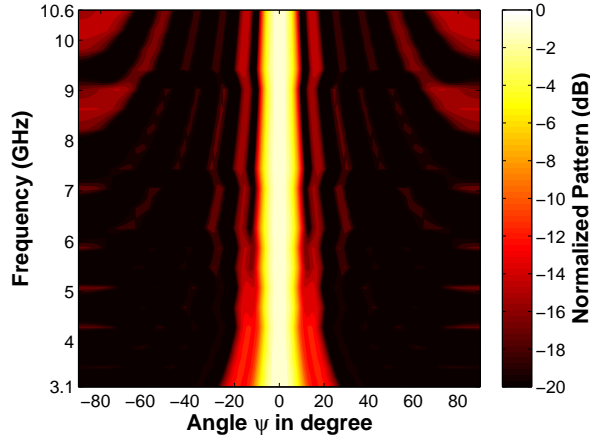requency invariant beamforming at different scan angles can be established by scaling the cut-off frequencies of the LPFs while still maintaining the position of the elements.

The coefficient k_2 has been introduced in equation (5.1.10) to calculate the cut-off frequency of the LPFs. According to (5.1.9) and (5.1.10), the number of the active element at the highest operating frequency is equal to $P + 1$ since the value of k_2 is equal to k_1. By setting a different value of k_2, the electrical length of the active sensor over frequency is changed and the cut-off frequencies are scaled to new values. The group delay of the LPFs are changed as well since the cut-off frequencies are altered. Therefore, the beam can be controlled to a particular scan angle.

Before investigating the frequency invariant beam scanning, the feeding filter, namely the Butterworth filter is firstly characterized. The Gaussian filter is described for a comparison with the Butterworth filter. The Butterworth filter is a filter which provides a maximally-flat amplitude and produces almost a maximally-flat group delay in the regime of passband. On the other hand, the Gaussian filter provides a complete maximally-flat group delay in the passband yet with reduced flatness of the amplitude in comparison with the Butterworth filter. In the regime of passband, both types of filter act like a time delay. Moreover, the delay of the filter is a function of cut-off frequency and filter order. As a brief description, the phase 'dilation' over frequency of nth order maximally flat gaussian

77

filter with cut-off frequency f_c is given as [46]

$$\varphi(f) = A2\pi f \left[1 + P \left(\frac{f}{f_c} \right)^{2n} \right] \tag{5.2.1}$$

where P and A are constants. A more detailed description of the Gaussian and the Butterworth filter are given as following.

5.2.1 Gaussian (maximally-flat group delay) response

A sharp cut-off response of a filter generally results in an inferior characteristic of phase response. On the other hand, some applications need to have linear phase distribution in the passband to avoid signal distortion. In this case, the Gaussian filter provides such a linear phase (maximally flat group-delay response).

(a) Amplitude response   (b) Phase response
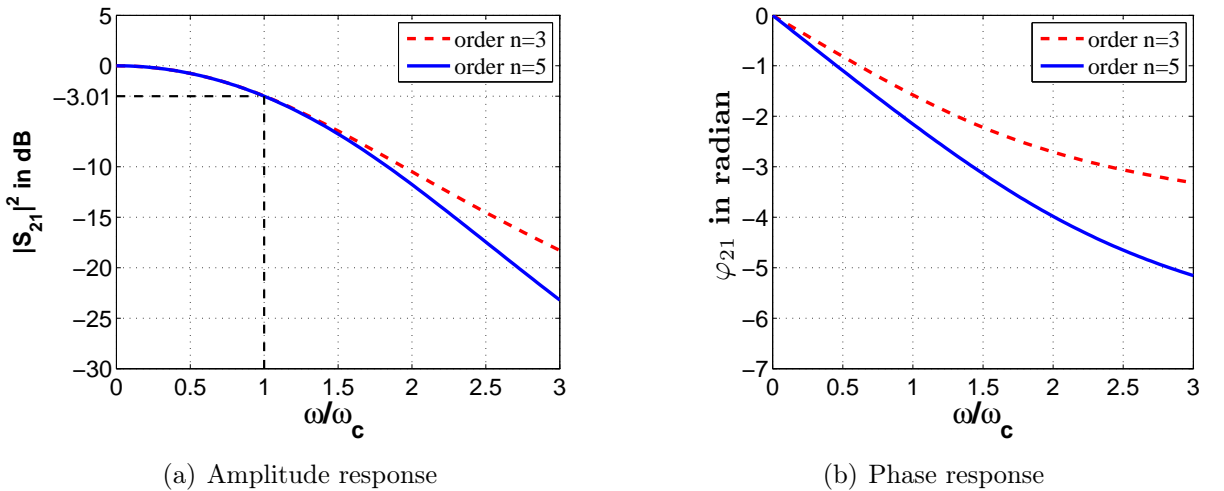
Figure 5.6: Amplitude and phase response of Gaussian filter order 3 and order 5

Fig. 5.6(a) and Fig. 5.6(b) illustrate amplitude and phase response of the 3rd and the 5th order Gaussian filters simulated by using a circuit simulator. The 5th order filter seems to provide higher amplitude attenuation outside the passband and more phase linearity in comparison with the 3rd order filter. In the passband regime, this filter has poor selectivity by the amplitude response. The Gaussian filter is not appropriate to be used as LPF feed of the discrete array sensor due to the lower selectivity of the amplitude response.

5.2.2 Butterworth maximum-flat response

In comparison with the Gaussian filter, the Butterworth filter provides a flatter amplitude in the passband regime and a higher attenuation outside the passband. The transfer

function of the Butterworth filter is given as [55]

$$S_{21}(p) = \frac{1}{\prod_{i=1}^{n}(p - p_i)}, \tag{5.2.2}$$

where $p = \sigma + j\Omega$ is normalized complex frequency variable and n represents the filter order. For a lossless passive network, $\sigma = 0$, and $p = j\Omega$, where Ω is the normalized angular frequency ω/ω_c. The pole distribution of a Butterworth filter is expressed as

$$p_i = e^{j\frac{\pi}{2n}(2i+n-1)}. \tag{5.2.3}$$
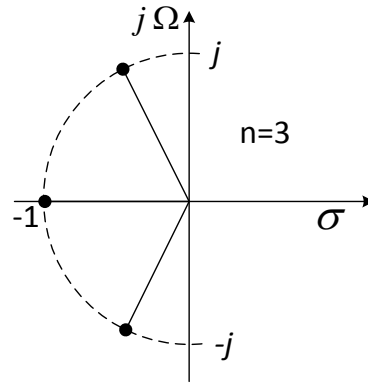
Figure 5.7: Pole distribution of the 3rd order Butterworth filter

(a) Amplitude response

(b) Phase response

Figure 5.8: Amplitude and phase response of Butterworth filter

An example of pole distribution for the Butterworth filter of order 3 is illustrated in Fig. 5.7. It is evident from the picture that the poles are equally distributed on a half circle at the left part of the half circle as a characteristic of the Butterworth filter.
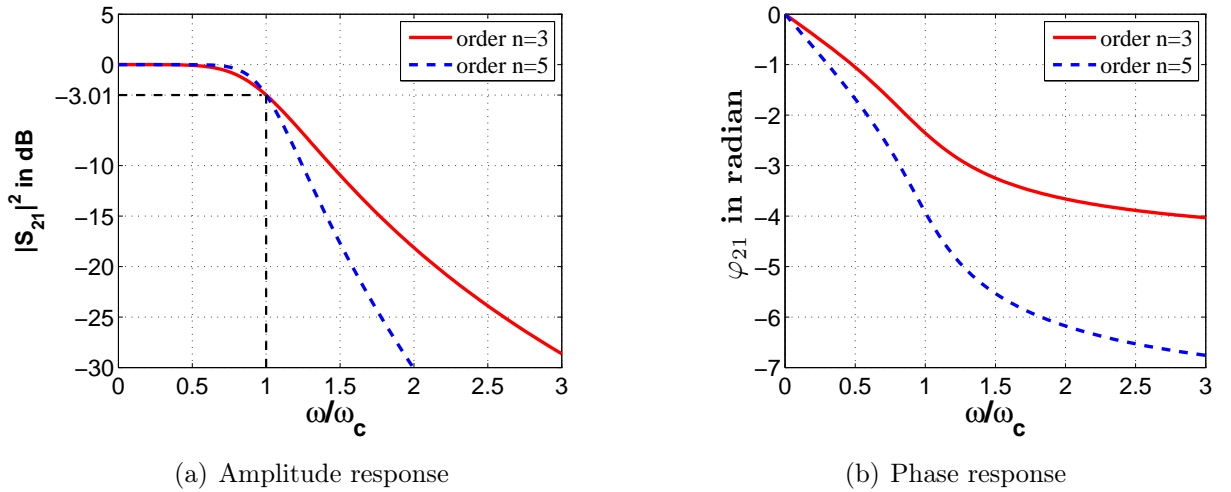
Based on the pole formulation, amplitude and phase delay of the filter can be derived. The amplitude variation and the phase delay of the 3th order and the 5th order Butterworth filters are shown in Fig.5.8(a) and Fig. 5.8(b) respectively. As can be seen in Fig. 5.8(a), the filter of order 5 provides a flatter amplitude response in the passband; a higher attenuation is found outside of the passband. On the other hand, the phase delay of the filter seems to be linear in the passband region as depicted in Fig. 5.8(b). In addition, the filter of order 5 provides a steeper phase delay which indicates a longer delay.

5.2.3 Design of a frequency invariant beam scanning

The pattern of a non-uniform spacing linear array antenna of N-elements can be expressed as

$$AF = \sum_{i=0}^{N-1} exp\left[j\left(kx_i \sin\theta + \alpha_i\right)\right] \tag{5.2.4}$$

where x_i is the position of the ith element with respect to the reference position x_0. To scan the beam to a direction of θ_0, the excitation phase of α_i is given as

$$\alpha_i(f) = -\frac{2\pi f}{c}x_i \sin\theta_0. \tag{5.2.5}$$

Since the element x_i is excited by the filter with phase response φ_i, equation (5.2.5) can be expressed as

$$\varphi_i(f) = -\frac{2\pi f}{c}x_i \sin\theta. \tag{5.2.6}$$

As shown before, the frequency invariant beamfoming results in a scanned beam at a particular angle as a side effect of phase dilation of the LPFs. The scan angle can be controlled to a particular direction by using a reference design. The reference design is a preliminary design with a set of initial parameters. By identifying the cut-off frequencies and the scan angle of the reference design, a parameter design for a particular scan angle can be obtained.

Assumed $\varphi_{1,i}(f, f_{c1})$ is the phase response of the reference model with cut-off frequency f_{c1} and $\varphi_{2,i}(f, f_{c2})$ is the the phase response of the design with cut-off frequency f_{c2}, then

$$\varphi_{1,i}(f, f_{c1}) = -\frac{2\pi f}{c}x_i \sin\theta_1$$
$$\varphi_{2,i}(f, f_{c2}) = -\frac{2\pi f}{c}x_i \sin\theta_2 \tag{5.2.7}$$

where θ_1 and θ_2 are the reference scanning angle and the desired scanning angle respectively. Since the spacing between the elements are kept constant, equation (5.2.7) can be written as

$$\sin\theta_2 = \frac{\varphi_{2,i}(f, f_{c2})}{\varphi_{1,i}(f, f_{c1})}\sin\theta_1. \tag{5.2.8}$$

Assumed τ_1 and τ_2 are the group delay of $\varphi_{2,i}(f, f_{c2})$ and of $\varphi_{1,i}(f, f_{c1})$ respectively, the relation between the group delay and the scanning angle is expressed as

$$\sin \theta_2 = \frac{\tau_2(f)}{\tau_1(f)} \sin \theta_1. \tag{5.2.9}$$

Since f_{c2} is scaled from f_{c1} by the coefficient of k_2, the target angle θ_2 can be controlled by adjusting k_2.

In order to prove this concept, a beamforming scenario over the UWB frequency band is shown as following. An isotropic radiator array sensor with element number $N = 11$ is designed. The parameter $P = 4$ is assumed; the value of $k_1 = 0.5$ is given while the value of k_2 is varied from 0.5 to 1.8. The 12th order Butterworth LPF is assumed in the scenario. The cut-off frequencies associated with k_1 and k_2 are calculated in table 5.1

Table 5.1: Cut-off frequency of each sensor associated with k_1 and k_2

	Cut-off frequency of the sensor at position-i (GHz)										
$k_1;k_2$	*0*	*1*	*2*	*3*	*4*	*5*	*6*	*7*	*8*	*9*	*10*
0.5;0.5	-	42.40	21.20	14.13	10.60	8.48	5.96	4.47	3.35	2.52	1.89
0.5;07	-	59.36	29.68	19.79	14.84	11.87	8.35	6.26	4.70	3.52	2.64
0.5;1	-	84.80	42.40	28.27	21.20	16.96	11.93	8.94	6.71	5.03	3.77
0.5;1.2	-	101.76	50.88	33.92	25.44	20.35	14.31	10.73	8.05	6.04	4.53
0.5;1.8	-	152.64	76.32	50.88	38.16	30.53	21.47	16.10	12.07	9.06	6.79

The gray colored cells of each combination k_1 and k_2 in the table denote the active elements at the upper limit of the frequency band. From the cut-off frequencies of the first row, it is seen that five elements are active when the value of k_2 is 0.5. The number of active elements increases as the increased value of k_2. The associated filters with cut-off frequency higher than 10.6 GHz have no contribution to deactivate the elements. Yet, they act as a time delay where the filter with higher cut-off frequency provides a shorter time delay. The variation of the filter group delay determines the scan angle. Fig. 5.9 describes the group delays of the sensor at second position for different values of k_2 by keeping the value of $k_1 = 0.5$. It is seen that the increased value of k_2 makes the group delay to be smaller. Therefore, the beam would be scanned closer to the broadside direction.

Fig. 5.10(a) to Fig. 5.10(f) show the frequency invariant beam forming of the array for different values of k_2. The simulation indicates that the beam is scanned to different directions by changing k_2 while still keeping the frequency invariant beam pattern. As k_2 increases, the beam is scanned to a direction closer to the broad side. If the design with parameters $k_1 = 0.5$ and $k_2 = 0.5$ is assumed as the reference design, then the beam scan angle of 45° is assumed as the reference angle. Hence, the target angle θ_2 can be calculated
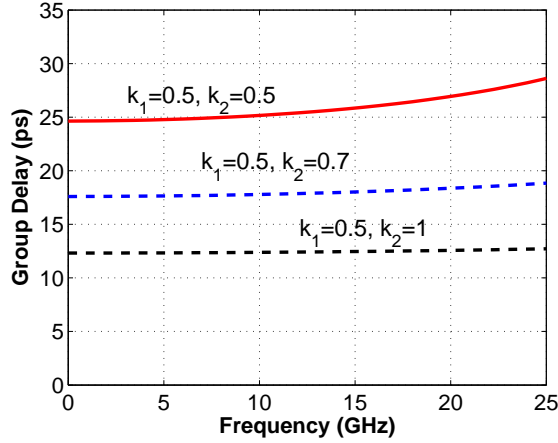
Figure 5.9: Group delay of the 2nd sensor with given values of k_1 and k_2

by extracting the phase of the transfer function in (5.2.2). In this scenario, the values of target angle are calculated as 30° for $k_2 = 0.7$ and 20° for $k_2 = 1$. These results verify the simulations in Fig. 5.10(d) and Fig. 5.10(f).

Another parameter to control the beam scanning is the filter order. Since the filter order increases, the phase gradient of the filter in the passband is steeper such that the group delay is larger. Therefore, the beam would be scanned closer to the end fire direction. To verify this concept, the beam scanning of the 11-element array sensor is simulated by varying the filter order. In this scenario, the variables of k_1 and k_2 are kept 0.7. The order of Butterworth LPFs is varied as 5, 10 and 20. Fig. 5.11(a) to Fig. 5.11(f) show the simulation results of such a beam scanning. As shown in Fig. 5.11(a), the beam is scanned to 13° by employing the filter of order 5. As the filter order increases, the beam is scanned closer to the end fire direction. It is clearly seen that the beam is scanned to 30° by employing the 10th order filter and the scanning angle increases to 40° by employing the 20th order filter .

Based on these simulations, the frequency invariant beam scanning can be controlled by varying the order and the cut-off frequency of the Butterworth LPFs. This concept seems to be attractive in the field of antenna beamforming theory since the variation of the beamwidth over frequency can be avoided. The concept could be extended by utilizing active electronic variable filters as the feeding filters to create electronic beam scanning.

(a) Contour plot, $k_1 = 0.5$ and $k_2 = 0.5$

(b) Cartesian plot, $k_1 = 0.5$ and $k_2 = 0.5$

(c) Contour plot, $k_1 = 0.5$ and $k_2 = 0.7$

(d) Cartesian plot, $k_1 = 0.5$ and $k_2 = 0.7$

(e) Contour plot, $k_1 = 0.5$ and $k_2 = 1$

(f) Cartesian plot, $k_1 = 0.5$ and $k_2 = 1$
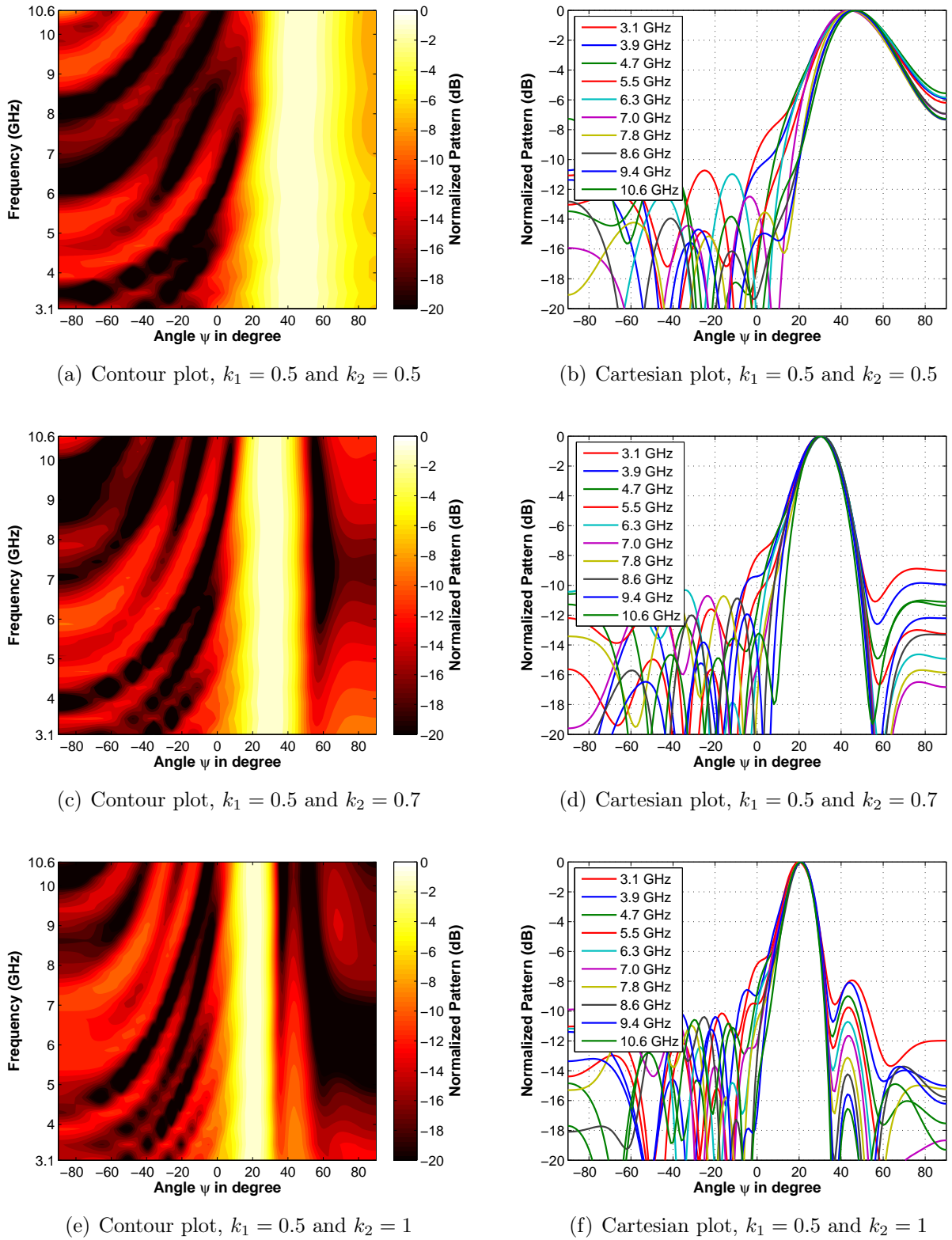
Figure 5.10: Frequency invariant beamforming of 11-isotropic element array sensor for different values of k_2

(a) Contour plot, order 5

(b) Cartesian plot, order 5

(c) Contour plot, order 10

(d) Cartesian plot, order 10

(e) Contour plot, order 20
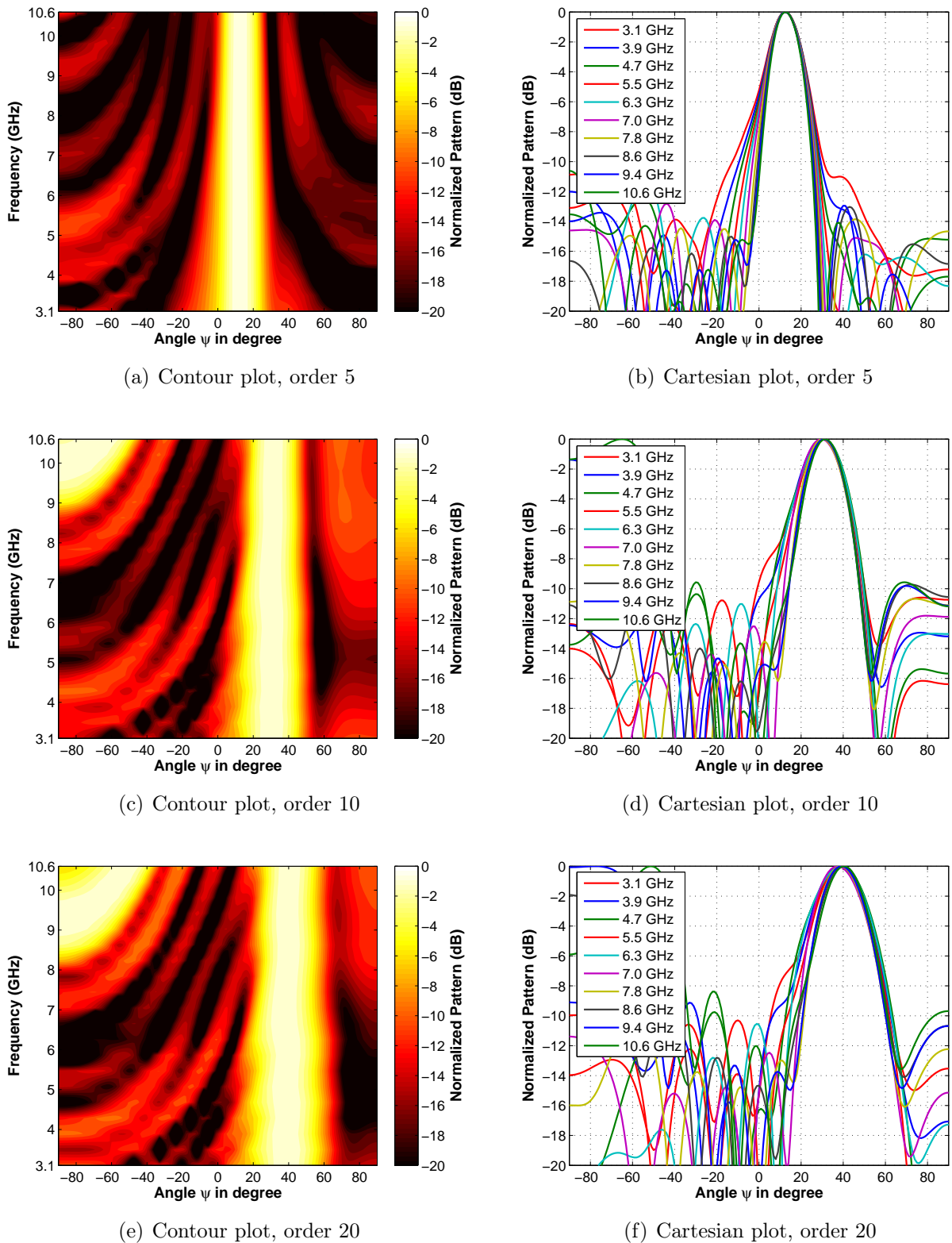
(f) Cartesian plot, order 20

Figure 5.11: Frequency invariant beamforming of 11-isotropic element array sensor for different values of filter order

5.3 Discrete sensor array theory in comparison with FIR-filter controlled array

Many investigations have been done, especially based on signal processing theory, to achieve frequency invariant beam patterns. Some concepts propose a FIR filter feed where the frequency invariant beam pattern is achieved by optimizing the coefficients of the FIR filters based on a prescribed template of radiation patterns. Reference [56] proposed a hybrid concept combining the digital signal processing concept with a microwave realization of a frequency invariant beam pattern. The coefficients of the filters are calculated by an optimization algorithm, the so called *convex* algorithm [57] and the FIR filters have been successfully realized as analog filter circuits for the frequency range of 1.5 to 2 GHz. The concept is relatively robust and can establish frequency invariant beam patterns with high correlation to a given template of radiation pattern. However, the array design strongly depends on the optimization procedure where the effective number of required antenna elements and delay tabs of the filters can not be assessed analytically. The effective number of elements as well as the number of tabs depends on bandwidth and scan angles. A larger number of antenna element somehow is required to achieve a frequency invariant beam pattern.
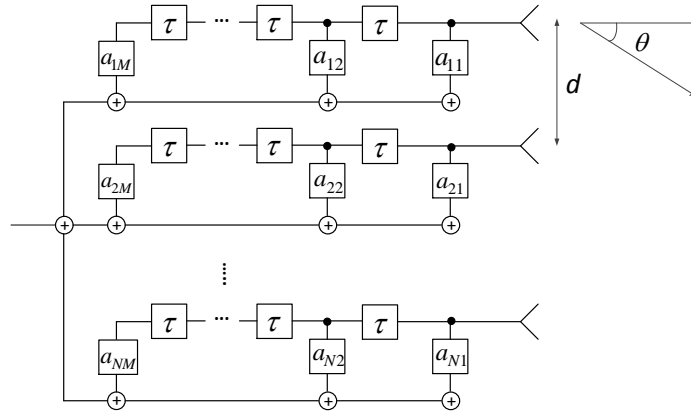
Figure 5.12: Structure of FIR-filter controlled array [56]

Fig. 5.12. shows the schematic of a linear antenna array fed by a FIR filter feed network. The array consists of N elements and the weighting coefficients of the FIR filter are denoted as a_0, a_1, a_2, ... ,and a_M.

The pattern of a linear array antenna with FIR filter feed network can be expressed as

$$E(f, \theta) = \sum_{n=1}^{N} \sum_{m=1}^{M} a_{nm} exp \left(j \left(\frac{2\pi f}{c} (n-1) d \sin \theta - 2\pi f (m-1) \tau \right) \right) \qquad (5.3.1)$$

where a_{nm} is the mth weighting filter coefficient of the nth antenna element and τ is the incremental delay of the FIR filter. Fig. 5.13(a) shows an example simulation result of

frequency invariant beam pattern for the ratio of the highest and the lowest frequency of 2:1. In the scenario, the beam is scanned to 10°. To achieve the frequency invariant beam pattern over frequency range, 20 antenna elements are arranged as a linear array and 16th filter order is required in the design.

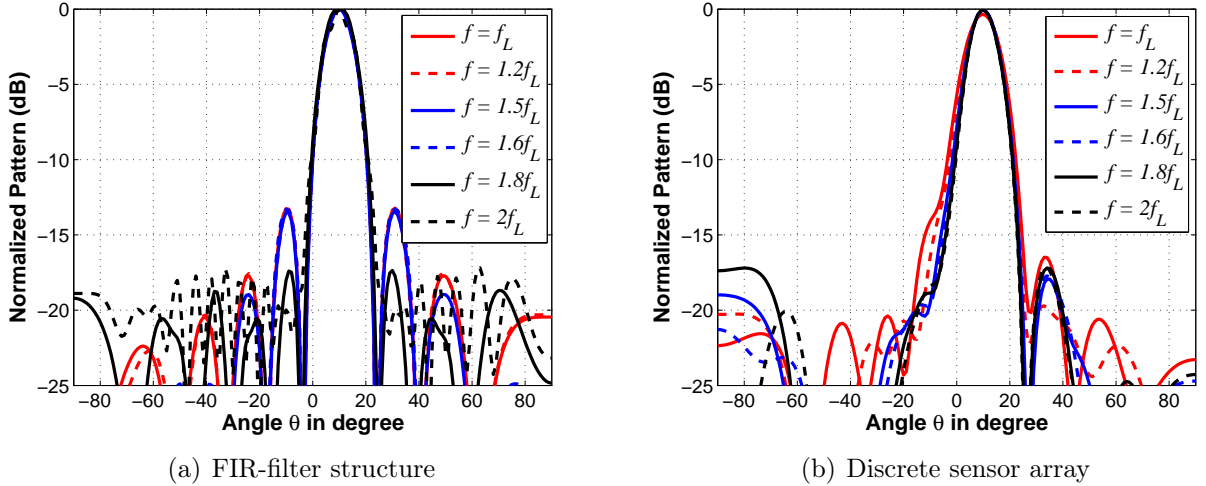(a) FIR-filter structure   (b) Discrete sensor array

Figure 5.13: Frequency invariant beam pattern of FIR-filter structure array (a) and of discrete sensor array (b)

The result for a discrete sensor array designed under the same specification is shown in Fig. 5.13(b). In the scenario, the frequency invariant beam pattern is established by only 11 antenna elements with 5th order LPFs. Even though small variation of the beam pattern is seen in this design, the number of the elements was reduced significantly and a much lower filter order was used as well. Therefore, the discrete sensor concept can be an alternative to design frequency invariant beam patterns instead of the FIR-filter controlled array procedure.

5.4 Time domain analysis of the frequency invariant beam pattern

The variation of the beam pattern over frequency has been introduced in chapter 2. For a conventional array design, the beamwidth changes dramatically over frequency and grating lobes can appear at higher frequencies. The pattern in frequency domain can be compared to the pattern in time domain which will be shown in this subsection.

The inverse Fourier transform can be applied to describe the radiation pattern in the time domain. For demonstration, a simulation scenario of a conventional isotropic element antenna array in the UWB frequency range was designed where the antenna consists of seven elements and the beam scanned to 20°. The uniform element spacing is the free-space wavelength at the highest operating frequency. Fig. 5.14(a) shows the beam pattern

over the UWB frequency range. It is seen that at the lowest frequency the beamwidth is 28° while at the highest frequency the beamwidth decreases to 8°. In addition, a grating lobe appears at frequency 7.8 GHz. The time domain pattern of this array is shown in Fig. 5.14(c). The variation of the beamwidth with frequency seems less pronounced in the time domain. The appearance of the grating lobes in the frequency domain is not seen significantly in the time domain. As clearly seen in the spatial snapshot of the time domain power pattern at the peak value, shown in Fig. 5.14(e), the side lobe level is seen constant between -9 and -11 dB below the peak value, which can be understood as an averaging of the sidelobes plus the grating lobe. This effect could benefit UWB pulse communication systems compared to carrier based systems.

In contrast, it is interesting to see the time domain pattern based on the frequency invariant beam pattern. An isotropic element linear array was designed to create a frequency invariant beam pattern where the length of active element is kept at 6 λ. The beam pattern over the UWB frequency range can be seen in Fig. 5.14(b). In this simulation, the beamwidth seems to be constant around 10°. A side lobe peak of approximately -12 dB is found at the angle of 44°. The inverse Fourier transform of this pattern can be seen in Fig. 5.14(d) while the spatial snapshot of the power pattern is depicted in Fig. 5.14(f). The time domain pattern in Fig. 5.14(f) looks similar to the frequency domain pattern in Fig. 5.14(b). This indicates that the the time domain and the frequency domain plots for frequency invariant beam pattern arrays are more identical in comparison with the time domain and frequency domain plots of conventional linear arrays. Moreover, at the spatial angles close to -90° the amplitude seems to be lower due to less contribution from the grating lobe. On average, the side lobe level of the time domain pattern based on the frequency invariant pattern seems to be lower by around 3 dB than the time domain pattern of the conventional linear array, although the peak side lobe appearing due to the phase dilation of the LP-filters produces a distinct side lobe in the time domain pattern at -7 dB.
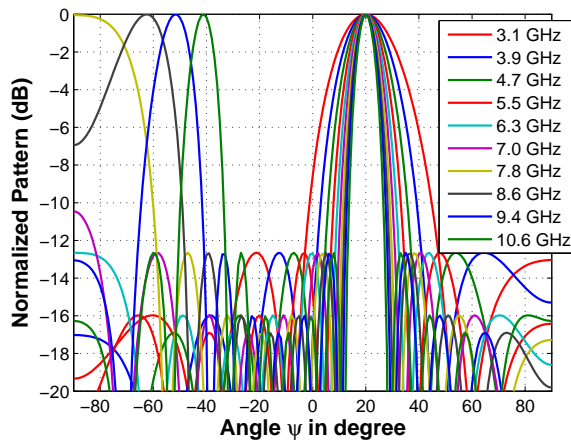
(a) Frequency domain pattern of conventional linear array
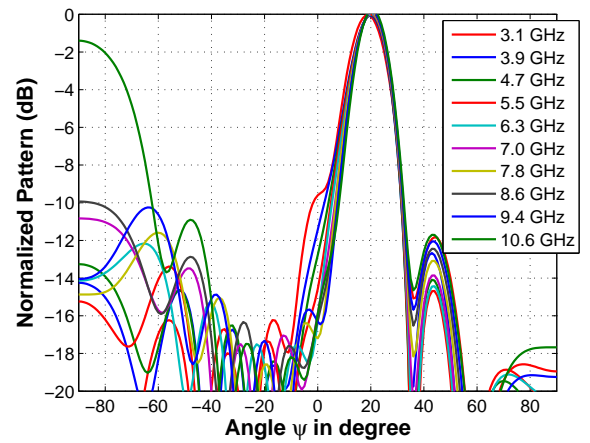
(b) Frequency invariant beam pattern of linear array sensor
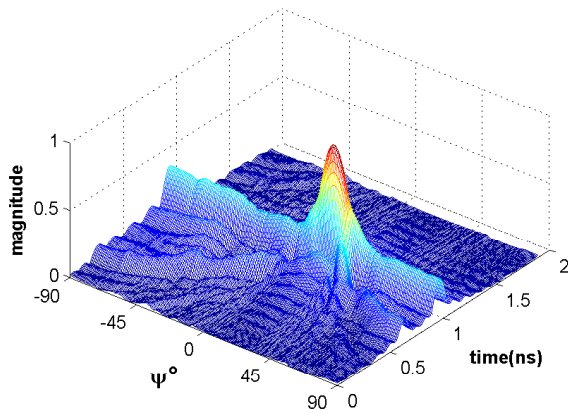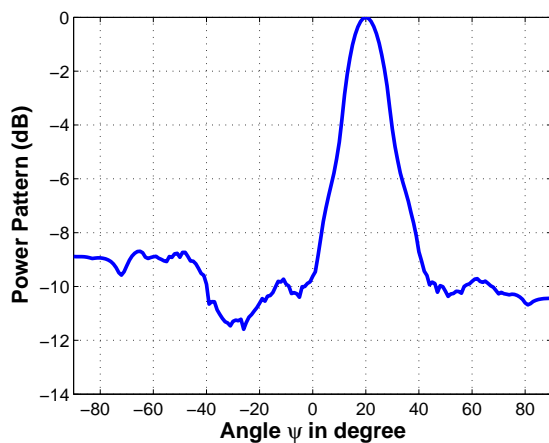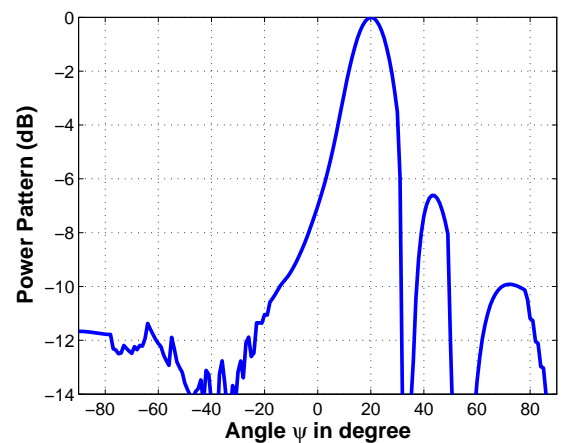

(c) Time domain pattern of conventional linear array sensor
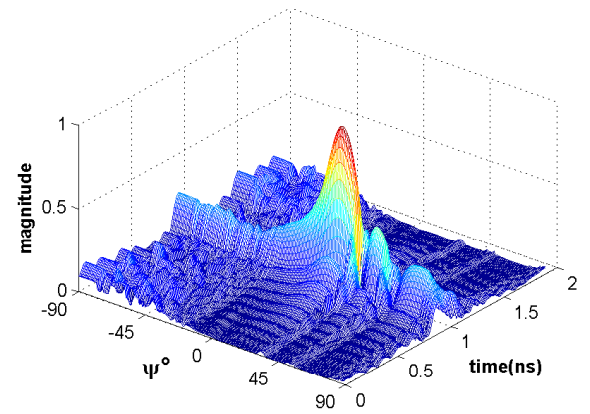
(d) Time domain pattern of frequency invariant linear array sensor

(e) Snapshot of time domain pattern of conventional linear array

(f) Snapshot of time domain pattern of frequency invariant linear array sensor

Figure 5.14: Comparison of the frequency and the time domain radiation patterns

5.5 Eight-element U-shaped PCMAA with frequency invariant far-field beam pattern

The concept described in section 2 of this chapter was applied to a uniform spacing eight-element U-shaped PCMAA to realize a frequency invariant beam pattern. The minimum spacing between the elements is restricted by the width of the single radiator, namely 46 mm. This limitation together with the uniform element spacing makes the array structure to deviate from the ideal model. In order to approximate the ideal structure, the array is designed as following: $N = 8$, $P = 6$, $k_1 = 1$, $k_2 = 0.7$ and $f_U = 6.5$ GHz. The calculated cut-off frequencies based on these parameters are given in table 5.2. The radiation pattern

Table 5.2: Cut-off frequency of the LPFs for eight-element uniform spacing array

Cut-off frequency of the filter at i^{th} position (GHz)							
i	0	1	2	3	4	5	6	7
f_c	-	27.30	13.65	9.10	6.83	5.46	4.55	3.90

of an eight-element isotropic linear array sensor with uniform spacing of 46 mm is shown in Fig. 5.15(a). For a linear array with uniform spacing of 46 mm, theoretically, the grating lobe rises at 6.5 GHz and the beam position is found at the center. Due to the LP-filter phase dilation, the beam is scanned to 19° and the grating lobe rises at a lower frequency of approximately 5 GHz.

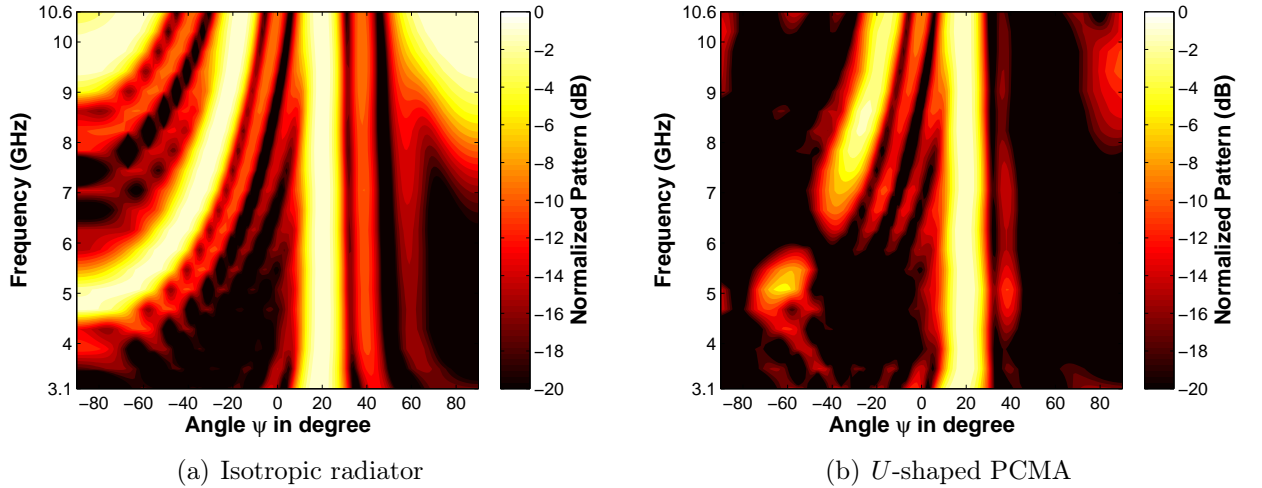(a) Isotropic radiator

(b) U-shaped PCMA

Figure 5.15: Frequency invariant beam pattern of eight-element uniform spacing linear array

Further, the pattern of an eight-element U-shaped PCMAA based on the pattern multiplication concept is shown in Fig. 5.15(b). In comparison with the isotropic model, a

significant difference associated with the grating lobe can be seen. The plot shows that the grating lobe is first appearing at an angle of -40° (instead of -90°). This can be explained by antenna array theory as follows. The pattern of an array antenna $E(\psi, f)$ results from

$$E(\psi, f) = f_i(\psi, f)AF(\psi, f) \tag{5.5.1}$$

where $f_i(\psi, f)$ and $AF(\psi, f)$ represent element pattern and array factor respectively. The element pattern of the printed circular monopole antenna is directive and provides low directivity at angles of -90° to -40°, see Fig. 4.7, such that it suppresses the grating lobe of the array factor in this angular range.

With respect to the scanned beam, a set of additional delay lines can be inserted in the feed network to compensate the filter delays such that the beam returns to the broad side. Fig. 5.16. shows the schematic design of the frequency invariant beam pattern antenna array with additional delay lines.
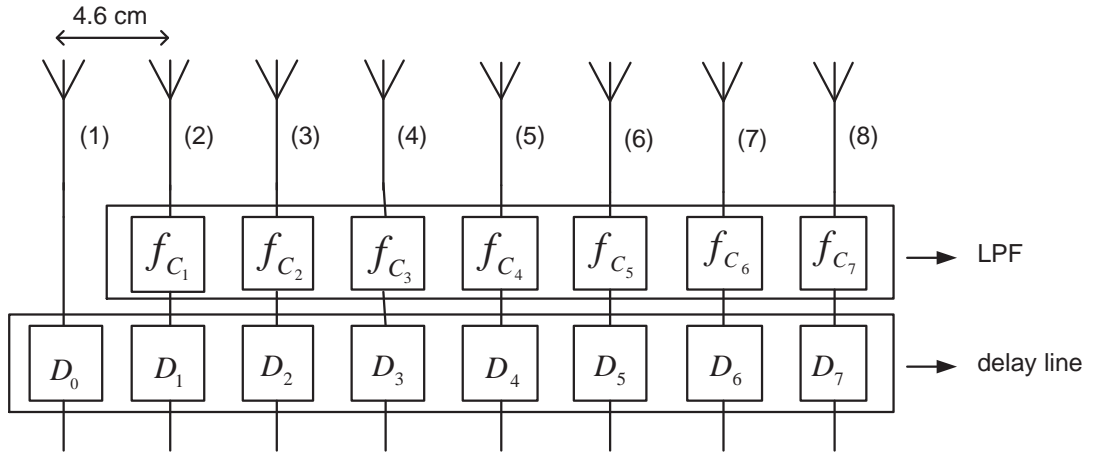

Figure 5.16: Schematic of antenna array integrated with filter and delay line

Based on this schematic, an eight-element PCMAA with frequency invariant beam pattern was designed. The uniform spacing between the elements is equal to the width of the *U*-shaped PCMA. Seven elements are fed by LPFs and eight progressive delay lines are used to compensate the delay of the LPFs. The LPFs are realized as microstrip line stub LPF and the delay lines are realized as worm-shaped microstrip lines as shown in Fig. 5.17. The normalized radiation pattern in the UWB frequency range can be seen in Fig. 5.18. This pattern is obtained from the combination of employing three simulators namely MATLAB, circuit simulator and full wave simulator which is simulated based on pattern multiplication concept. In this case, the delay line and the microstrip-stub LPFs are simulated by using the Momentum simulation (circuit design software ADS Agilent) and the element pattern is simulated by using full wave simulator (EMPIRE XCcel). The simulation based on the pattern multiplication shows that the beam position is found at the broad side direction. In addition, the grating lobes appear less pronounced due to the contribution of the element pattern and the beamwidth seems constant over frequency.
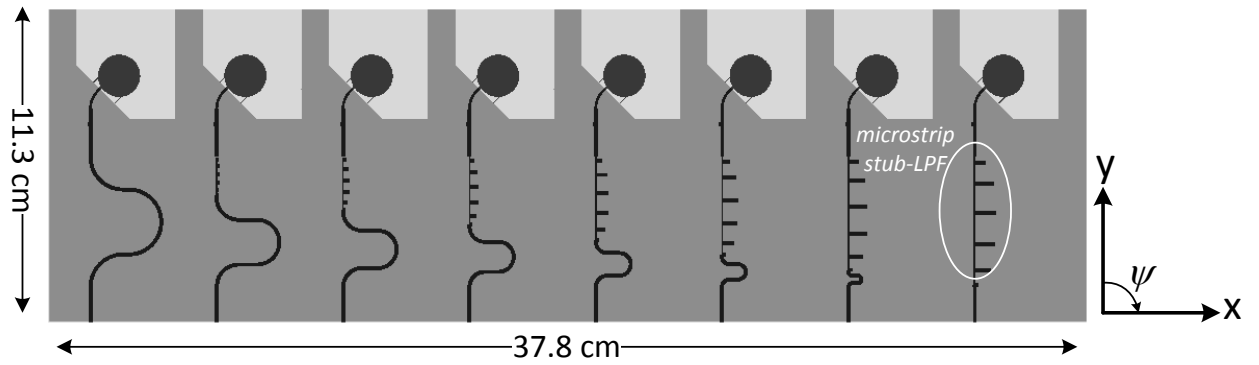
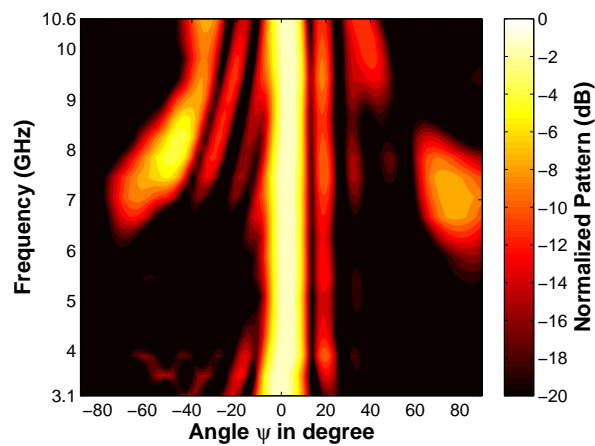Figure 5.17: Layout of eight-element U-shaped PCMA array fed by LPFs and delay lines

Figure 5.18: Frequency invariant beam pattern of eight-element PCMAA

6 Realization of U-shaped PCMA Array with Frequency Invariant Beam Pattern

Results presented in this chapter have been object of publication [11]. Further details on published results are provided in this chapter. The concept of the UWB Wilkinson power divider is discussed in order to realize a feed network for the eight-element PCMAA. First, the design of a single UWB Wilkinson power divider in planar technology is presented. Second, the single Wilkinson power divider is cascaded as a three-stage UWB Wilkinson power divider. Finally, the eight-element PCMAA and the three-stage Wilkinson power divider are fabricated and combined, and the measurement of the antenna radiation pattern performed to verify the simulation of the frequency invariant beam pattern of chapter 5.

6.1 The UWB Wilkinson power divider

In order to realize an array antenna with frequency invariant beam pattern, a set of LPFs are inserted in the feed network. The input wave is passed to the radiators at frequencies lower than the cut-off frequency while the signal is reflected at frequencies higher than the cut-off frequency. An isolation of the output port of the feeding network is required in order to suppress the coupling of the reflected wave from one output to the other output port, since such coupling contributions would superimpose the original incident waves and thus produce serious phase and amplitude errors which degrade the radiation pattern.

One type of power divider, namely the T-Junction power divider, has been discussed in chapter 4. The T-Junction power divider does not provide isolation between the output ports since it is without dissipative component. A circulator/isolator could be used to pass the signal below the cut-off frequency and at the same time to absorb the reflected signal above the cut-off frequency. However, circulators are expensive and bulky. Instead, a Wilkinson power divider is proposed for the feed network since the Wilkinson power divider provides an isolation by employing bridging resistors which can absorb the port-to-port coupling power of the reflected signal from the LPFs. In addition, a three-stage Wilkinson power divider can be used as the feeding network of the PCMAA to prove the concept of the frequency invariant beam pattern.
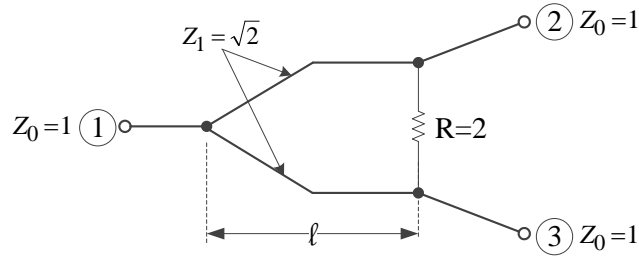
Figure 6.1: Equivalent circuit of Wilkinson power divider

A Wilkinson power divider is a passive circuit to provide n-output ports power division which was firstly proposed by Ernest J. Wilkinson in 1960 [58]. A three-port Wilkinson power divider by treating $n = 2$ is a special Wilkinson power divider which has been widely known as Wilkinson power divider.

An equivalent transmission line circuit of the Wilkinson power divider is shown in Fig.6.1. The equivalent circuit represents an equal-split power divider. It consists of two transmission lines Z_1 which connect the input to the output ports and the resistor R which is interconnecting the two output ports to provide isolation between the output ports. The length l of the transmission line Z_1 is equal to a quarter wavelength. The ratios of Z_1 and R to the characteristic impedance Z_0 are given as $\sqrt{2}$ and 2 respectively. These values can be calculated based on even-odd mode analysis [46]. In the best case, an equal-split Wilkinson power divider can provide approximately 100 % bandwidth with -14.7 dB isolation at the upper and the lower limit of frequency band. The bandwidth of this Wilkinson power divider does not completely cover the UWB frequency band. Therefore, a broadband Wilkinson power divider is proposed.

6.1.1 The broadband Wilkinson power divider

Several years after the concept of Wilkinson power divider has been published, Cohn proposed the concept of broadband three port hybrid power divider [59]. In his concept, the bandwidth as well as the isolation can be enhanced by designing a multiplicity of cascaded pairs of line lengths and interconnecting resistors which is described as a circuit design in Fig.6.2.

In this schematic, the power divider is designed as N-pair of cascaded transmission lines and each pair of transmission line is interconnected with one resistor. Each pair of transmission line and associated resistor is referred to as section. The length of each section, denoted as electrical length ϕ, is equal to a quarter wavelength with respect to the center frequency. The characteristic impedances of each section are represented as Z_1, Z_2, Z_3 to Z_N while the bridging resistors are defined as R_1, R_2, R_3 and R_N. These impedances and resistors can be analytically calculated by the method of even- and odd-mode. However, the impedances and the resistors can be practically calculated by using Cohn's table of three-port hybrid design [59].
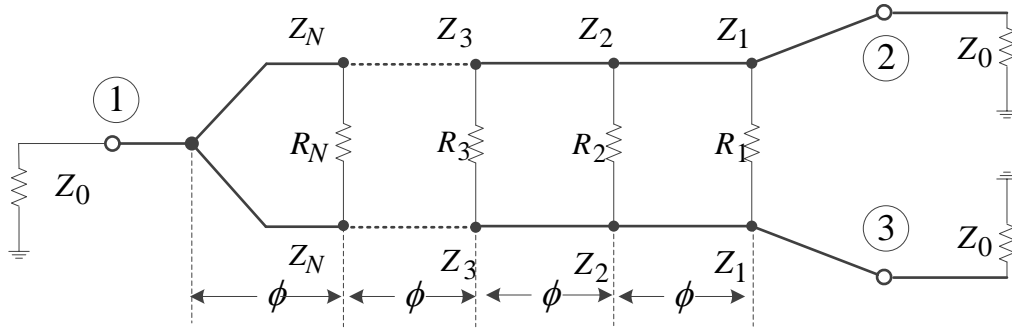
Figure 6.2: Equivalent circuit of multi-stage Wilkinson power divider

Table 6.1: N-section Wilkinson power divider (three-port hybrid design) [59]

N	1	2	4
Z_1	1.414	1.2197	1.1157
Z_2		1.6398	1.2957
Z_3			1.5435
Z_4			1.7926
R_1	2	4.8204	9.6432
R_2		1.9206	5.8326
R_3			3.4524
R_4			2.0633

Table 6.1 shows the parameters of equal split three-port hybrid power dividers for $N = 1$, 2 and 4 where the values are normalized to Z_0. The design of $N = 1$ was defined by Wilkinson while the design of $N = 2$ and $N = 4$ were proposed by Cohn. Theoretically, the performance of reflection and isolation enhance with the number of sections. However, increasing the number of section will also enlarge the feature size of the power divider and the transmission line dissipation loss.

For demonstration, three-port hybrid power dividers with different number of section are simulated by using the circuit design software ADS Agilent [60]. In the scenario, the power dividers are designed at the center frequency of 6.85 GHz and cover the frequency range from 3.1 to 10.6 GHz where the design parameters in table 6.1 are used in the simulation.

The reflection coefficient and the isolation of the one-, two- and four-stage Wilkinson power divider are shown in Fig.6.3(a) and Fig.6.3(b) respectively. It is clearly seen that the average value of reflection and isolation are lower as the section number increases while the reflection coefficient as well as the isolation decrease at the frequencies closer to the upper and the lower limit of the frequency band. The reflection coefficient and

(a) Reflection coefficient, $|S_{11}|$ (b) Isolation, $|S_{23}| = |S_{32}|$
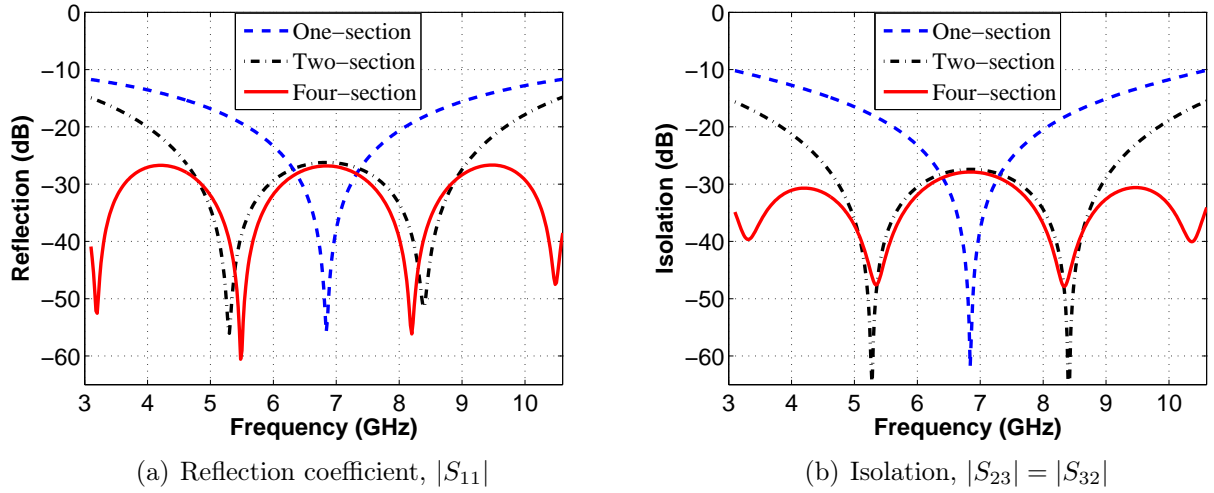
Figure 6.3: Reflection coefficient and isolation of Wilkinson power divider for one-, two- and four-section

the isolation of two-section power divider achieve the minimum value at 6.85 GHz. The values increase to -15 dB at the upper part and the lower part of the frequency band. On the other hand, the four-section power divider shows the reflection coefficient better than -25 dB for the whole frequency band. Therefore, the four-section Wilkinson power divider was selected and chosen as the feed network for PCMA array.

6.1.2 UWB four-section Wilkinson power divider

As theoretically discussed, the broadband Wilkinson power divider is realized in planar microstrip technology. The power divider is designed on the Duroid 5870 substrate, with $\epsilon_r = 2.33$, thickness $t = 0.5$ mm. Some deviations from the theoretical design can be found in the planar design. First, the coupling between the microstrip lines is not included in the theoretical design. Second, the parasitic effects of the resistors increases at the higher frequencies while such parasitic effects are not included in the theoretical design. To handle these problems, the microstrip part of the power divider is optimized in the 2.5-D simulator ADS momentum. A passive circuit design guide toolbox is used in the simulation as well. In addition, the *co-simulation* is applied to allow the interconnecting resistor to be integrated to the microstrip line as a circuit component described by its equivalent circuit in the window schematic.

Fig.6.4 shows the layout of the planar UWB Wilkinson power divider after optimization of the width of transmission lines and of the resistor values. It can be seen that the transmission lines of each section are shaped as rings to make the power divider to be more compact. The simulation result of the reflection coefficient and the isolation can be seen in Fig.6.5(a). The simulation shows matching impedance in the UWB frequency
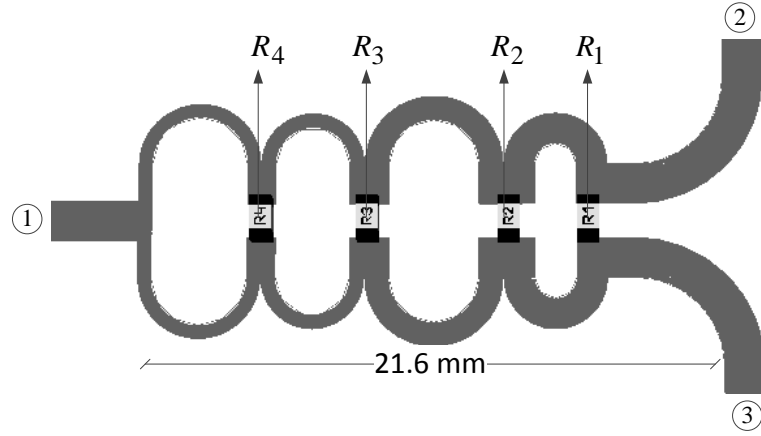
Figure 6.4: Layout of four-section Wilkinson power divider

range. In comparison with the broadband power divider available in the market place [61], it is acceptable with respect to reflection, isolation as well as the feature size.

Moreover, the broadband Wilkinson power divider is cascaded as a three-stage UWB Wilkinson power divider in order to realize a feed network for the eight-element PCMAA. The reflection coefficient and the isolation of the three stage Wilkinson power divider is shown in Fig.6.5(b). The reflection coefficient shows some peaks in the frequency range of interest where the maximum peak is found at -12 dB and the isolation is found better than -18 dB.

(a) one stage

(b) three stage

Figure 6.5: Reflection coefficient and isolation of four section Wilkinson power divider simulated by using the ADS (Agilent) circuit simulator

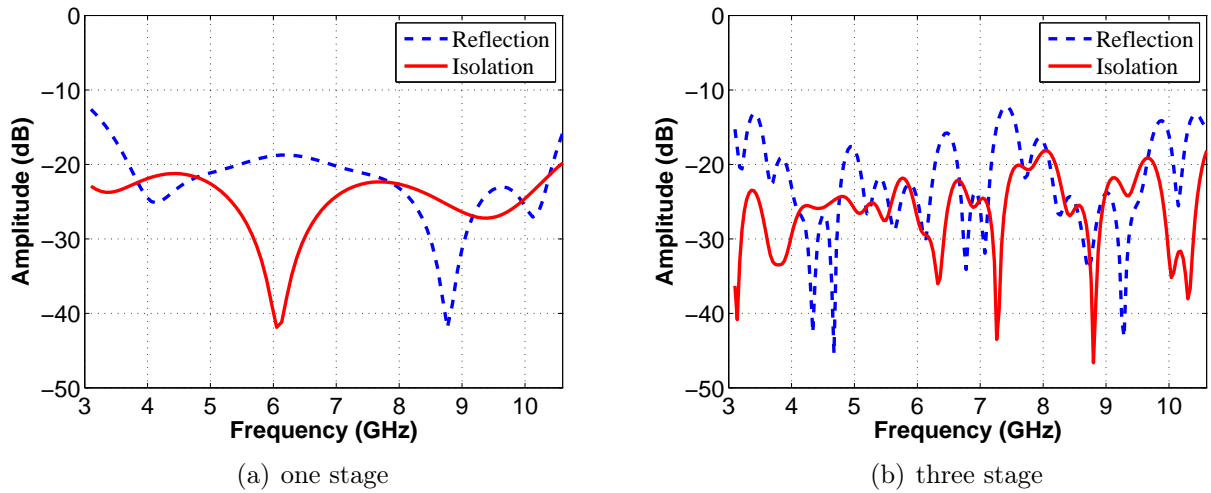## 6.2 Fabricated U-shaped PCMAA with frequency invariant beam pattern

As a verification of the theoretical design in chapter 5, the eight-element PCMAA was fabricated as shown in Fig.6.6. It can be seen that a set of microstrip line stub LPFs and a set of suitable microstrip delay lines are inserted in the feed network. The three-stage Wilkinson power divider feeds the PCMAA. The PCMAA and the power divider have been etched on the Duroid 5870 substrate, with $\epsilon_r = 2.33$ and thickness $t = 0.5$ mm. The PCMAA is plugged to the power divider by using eight SMA (Sub Miniature Version A) connectors.
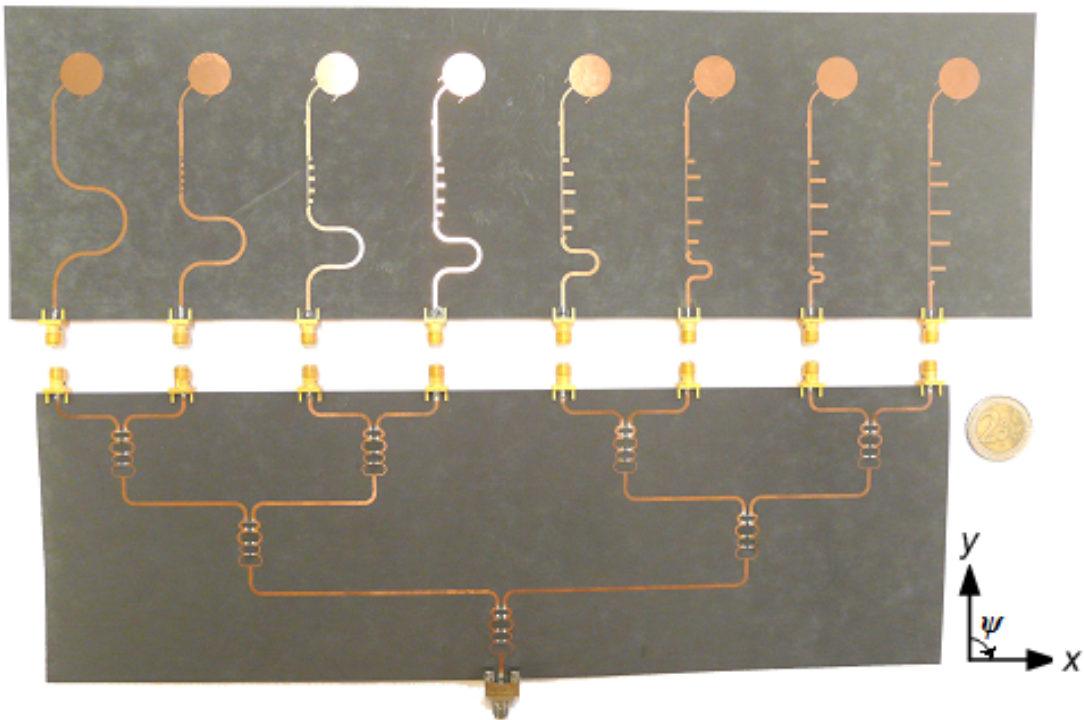
Figure 6.6: Fabricated antenna and power divider

The measurement results of the reflection coefficient can be seen in Fig.6.7. The measurement was carried out in two steps. The first step is the measurement of the power divider without the antenna and the second step is the measurement of the antenna which is connected to the power divider. The reflection coefficient of the Wilkinson power divider shows a good match from 3.1 to 7 GHz while peak reflection coefficient values up to -7 dB are found in the measurement above 7 GHz. On the other hand, the measurement of the antenna and the power divider shows peak reflection coefficients up to -7 dB as well while average return loss is found better than -10 dB across the band. These measurements indicate that the peak of -7 dB is strongly influenced by the reflection coefficient of the power divider. Further, a better reflection coefficient can be achieved by re-optimizing the power divider since the peak difference between the simulation and the measurement of

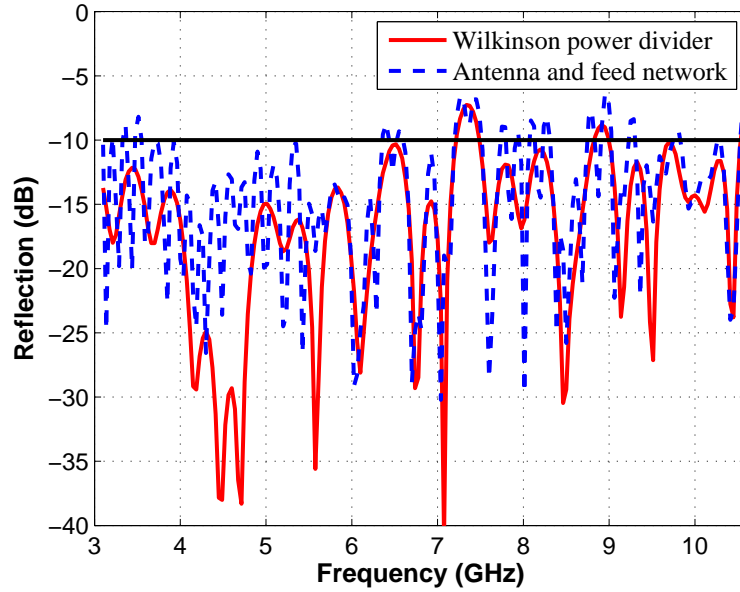Figure 6.7: Measured S-parameter reflection coefficient: feed network, antenna and feed network

the power divider could be due to the difference between the parasitic effects of the resistor model in the circuit design and the parasitic effects of the SMDs used in the fabrication. It has to be mentioned here that also the simple SMA connectors used at the input and the output port of the power divider contribute to the increase of the reflection coefficient in particular at the upper part of the band.

The measurement result of the radiation pattern can be seen in Fig.6.8(b). It can be compared to the normalized pattern from full-wave analysis in Fig.6.8(a) which shows a good agreement. The measurement verifies that the grating lobes appear less pronounced than in the simulation using isotropic radiators due to the directive element pattern of the printed circular monopole which partly suppresses the grating lobes. Even though the measured absolute gain was less than the simulated due to loss and imperfect matching, the frequency invariant beamwidth can be achieved over of most of the UWB frequency range. This experimental result proves that a set of low pass filters can be used to keep the array beamwidth over the UWB bandwidth constant.
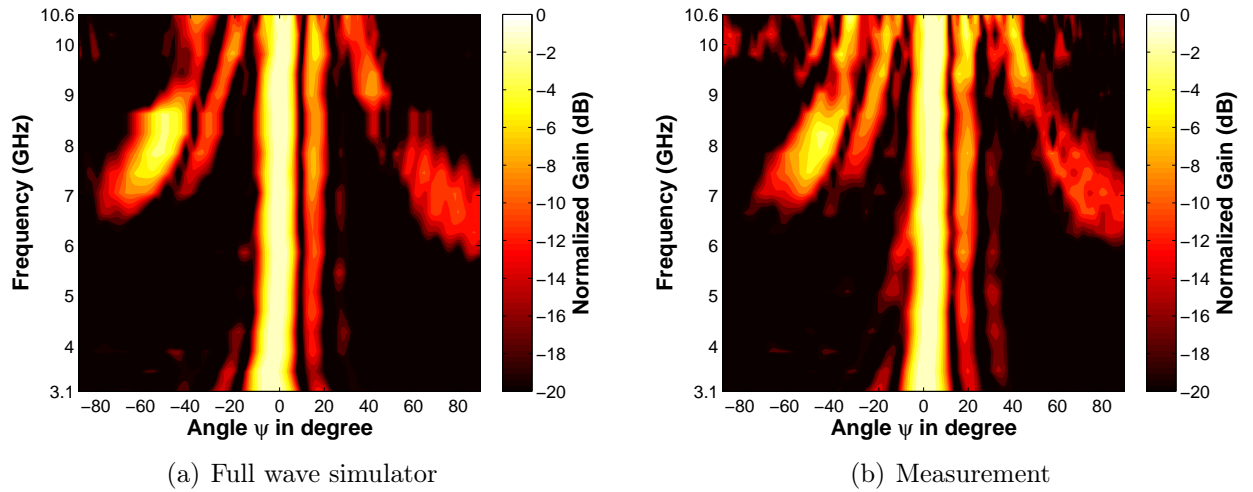
(a) Full wave simulator

(b) Measurement

Figure 6.8: Normalized gain of eight-element U-shaped PCMAA

7 Conclusion and future work

In this dissertation a planar array antenna has been designed for the frequency range of 3.1 to 10.6 GHz which employs special features to tackle the challenge of UWB technology with respect to the extremely low power radiation requirement. Three strategies based on antenna concepts have been proposed in this work. First, the directive printed circular monopole antenna, the so called U-shaped PCMA has been designed by modifying the original model of PCMA.

Next, a four-element linear array by using the U-shaped PCMA element has been realized which shows impedance matching better than -10 dB. In addition, a focused radiation pattern is produced by the antenna.

A design of an antenna array with frequency invariant beam pattern is proposed as the third strategy. The theory of discrete sensor array, adopted from the acoustic field, was applied in the microwave regime to realize frequency invariant beam patterns for the UWB frequency range. Consequently, the technique of frequency invariant beam scanning by using a set of low pass filters was presented as an alternative of the beamforming concepts such as the phase shifter and the time-delay beam scanning. This concept can also be an alternative of the frequency invariant beam pattern technique based on the FIR filter feed. In order to prove the concept, an 8-element PCMA linear array fed by microstrip shunt-stub low pass filters has been fabricated in planar technology. Simulation and measurement results indicated that the beamwidth can be kept constant across the UWB frequency band.

For the future work, active microwave FIR filters instead of passive LPFs could be implemented based on this concept to realize frequency invariant beam patterns which would require fewer FIR filters with lower filter order as well as fewer antenna elements as compared to Neinhues' method. A better radiation performance could be achieved by using microwave active filter since the variation of the gain due to the losses and imperfect matching can be compensated by amplitude weighting factors. A FIR filter could be used as a shaping filter [62] to perfectly compensate the loss in the feed network. In addition, the reflection from the low pass filters above the cut-off frequencies could be avoided by employing microwave FIR filters. Smaller radiator elements should also be realized to avoid the grating lobes in the whole frequency band. Moreover, the concept could be extended to the UWB communication systems for spectral masks of the higher frequency range, for example the bands from 54 to 59 GHz and from 61 to 66 GHz. In these frequency bands, the frequency invariant beam pattern antenna arrays could be realized in a much smaller size in comparison with the design of this work.

Literature

[1] L. Yang and G. Giannakis, "Ultra Wideband Communications: An Idea Whose Time Has Come," *IEEE Signal Processing Magazine*, vol. 21, no. 6, pp. 26–54, Nov. 2004.

[2] J. Kraus, "Antennas since Hertz and Marconi," *IEEE Transactions on Antennas and Propagation*, vol. 33, no. 2, pp. 131–137, Feb. 1985.

[3] H. Schantz, "A Brief History of UWB Antennas," in *IEEE Conference on Ultra Wideband Systems and Technologies*, pp. 209–213.

[4] ——, "Introduction to Ultra-Wideband Antennas," in *IEEE Conference on Ultra Wideband Systems and Technologies*, Nov. 2003, pp. 1–9.

[5] W. Sörgel and W. Wiesbeck, "Influence of the Antennas on the Ultra Wideband Transmission," *EURASIP Journal on Advances in Signal Processing*, 2005.

[6] W. Wiesbeck, G. Adamiuk, and C. Sturm, "Basic Properties and Design Principles of UWB Antennas," *Proceedings of the IEEE*, vol. 97, no. 2, pp. 372 –385, Feb. 2009.

[7] M. Sun, Y. P. Zhang, and Y. Lu, "Miniaturization of Planar Monopole Antenna for Ultra Wideband Radios," *IEEE Transactions on Antennas and Propagation*, vol. 58, no. 7, pp. 2420 –2425, July 2010.

[8] M. Uthansakul and M. Bialkowski, "Fully Spatial Wide-band Beamforming Using a Rectangular Array of Planar Monopoles," *IEEE Transactions on Antennas and Propagation*, vol. 54, no. 2, pp. 527–533, Feb. 2006.

[9] M. Neinhues and K. Solbach, "Finite Impulse Response Filter Based RF Beamforming Network for Wideband and Ultra-Wideband Antenna Arrays," *IET Microwaves, Antennas Propagation*, vol. 5, no. 7, pp. 844–851, 2011.

[10] A. Lambrecht, S. Beer, and T. Zwick, "True-Time-Delay Beamforming With a Rotman-Lens for Ultrawideband Antenna Systems," *IEEE Transactions on Antennas and Propagation*, vol. 58, no. 10, pp. 3189 –3195, Oct. 2010.

[11] Z. Ihsan and K. Solbach, "Frequency Invariant Far-Field Beam Pattern of UWB Printed Circular Monopole Antenna Array," in *German Microwave Conference (GeMiC)*, March 2012.

[12] C. Balanis, *Antenna Theory: Analysis and Design.* John Wiley & Sons, 2005.

[13] Z. Ihsan and K. Solbach, "Investigation of Patch Array Antenna Pattern Degradation," *German Microwave Conference (GeMiC)*, March 2008.

[14] B. Allen, M. Dohler, E. Okon, W. Malik, A. Brown, and D. Edwards, *Ultra Wideband Antennas and Propagation for Communications, Radar and Imaging.* Wiley, 2006.

[15] J. Proakis and M. Salehi, *Fundamentals of Communication Systems.* Pearson Prentice Hall, 2005.

[16] W. Sörgel, *Charakterisierung von Antennen für die Ultra-Wideband Technik.* Doctoral Dissertation, Universität Karlsruhe, 2006.

[17] M. El-Hadidy and T. Kaiser, "An UWB Channel Model Considering Angular Antenna Impulse Response and Polarization," in *The Second European Conference on Antennas and Propagation (EuCAP)*, Nov. 2007.

[18] M. El-Hadidy, T. Mohamed, F. Zheng, and T. Kaiser, "3D Hybrid EM Ray-Tracing Deterministic UWB Channel Model, Simulations and Measurements," in *IEEE International Conference on Ultra-Wideband (ICUWB)*, Sept. 2008.

[19] W. Wiesbeck, "Ultra-Wideband Antennas," *Script of UWB Antenna Course European School of Antennas*, April 2012.

[20] E. Pancera, *Strategies for Time Domain Characterization of UWB Components and Systems.* Doctoral Dissertation, Universität Karlsruhe, 2009.

[21] J. Marple, S.L., "Computing the Discrete-Time 'Analytic' Signal via FFT," in *IEEE Transaction on Signal Processing*, vol. 9, Sept. 1999.

[22] P. Knott, *Antennenmodellierung mit Diagrammsynthese zur Systemanalyse von konformen Gruppenantennen.* Doctoral Dissertation, RWTH Aachen, June 2002.

[23] T. Ma, *Theory and Application of Antenna Arrays.* Wiley, 1974.

[24] C. T. Famdie, W. L. Schroeder, and K. Solbach, "Numerical Analysis of Characteristic Modes on the Chassis of Mobile Phones," in *Proceedings of The First European Conference on Antennas and Propagation (EuCAP)*, Nov. 2006.

[25] P. Yazdanbakhsh and K. Solbach, "A Circuit Model of Monopole Four-Square Array Antenna on a Finite Ground Plane Including Mutual Coupling Effects," in *Proceedings of the Fourth European Conference on Antennas and Propagation (EuCAP)*, April 2010.

[26] B. Sanadgol, O. Litschke, and K. Solbach, "Method to Predict Scan Blindness in Printed Planar Phased Arrays," in *Proceedings of The Third European Conference on Antennas and Propagation (EuCAP)*, March 2009.

[27] R. Mailloux, *Phased Array Antenna Handbook*, ser. Artech House Antenna Library. Artech House, 1994.

[28] W. Sorgel, C. Sturm, and W. Wiesbeck, "Impulse Responses of Linear UWB Antenna Arrays and the Application to Beam Steering," in *IEEE International Conference on Ultra-Wideband (ICU)*, Sept. 2005.

[29] M. Neinhues, S. Held, and K. Solbach, "FIR-Filter Based Equalization of Ultra-Wideband Mutual Coupling on Linear Antenna Arrays," in *2nd International ITG Conference on Antennas*, March 2007.

[30] "EMPIRE XCcel," http://www.empire.de, accessed: 2013-04-01.

[31] J. Zürcher and F. Gardiol, *Broadband Patch Antennas*, ser. Artech House Antenna Library.

[32] D. Pozar, "Microstrip Antennas," *Proceedings of the IEEE*, vol. 80, no. 2, pp. 79–91, Jan 1992.

[33] P. Gibson, "The Vivaldi Aerial," in *The 9th European Microwave Conference*, Sept. 1979, pp. 101–105.

[34] Microwave Engineering (Hrsg.), "The 2000 CAD Benchmark." *Microwave Engineering*, July 2001.

[35] J. Liang, C. Chiau, X. Chen, and C. Parini, "Study of a Printed Circular Disc Monopole Antenna for UWB Systems," *IEEE Transactions on Antennas and Propagation*, vol. 53, no. 11, pp. 3500–3504, Nov. 2005.

[36] M. Pergol and W. Zieniutycz, "Unified Design Procedure for Planar Dipoles Oriented on UWB Application," *Progress In Electromagnetics Research*, vol. 102, no. 2, pp. 249–265, Jan. 2010.

[37] J. Langley, P. Hall, and P. Newham, "Balanced Antipodal Vivaldi Antenna for Wide Bandwidth Phased Arrays," *IEE Proceedings Microwaves, Antennas and Propagation*, vol. 143, no. 2, pp. 97 –102, Apr 1996.

[38] D. Manteuffel, T. Ould, and T. Kempka, "Antenna and Propagation Impairments of a UWB Localization System Integrated into an Aircraft Cabin," in *Loughborough Antennas and Propagation Conference (LAPC)*, Nov. 2010, pp. 589 –592.

[39] I. Hossain, S. Noghanian, and S. Pistorius, "A Diamond Shaped Small Planar Ultra Wideband (UWB) Antenna for Microwave Imaging Purpose," in *IEEE Antennas and Propagation Society International Symposium*, June 2007, pp. 5713–5716.

[40] I. Makris, D. Manteuffel, and R. Seager, "Miniaturized Reconfigurable UWB Antennas for the Integration into Consumer Electronic Products," in *Procedings of The Second European Conference on Antennas and Propagation EuCAP*, Nov. 2007.

[41] C.-C. Lin and H.-R. Chuang, "A 3-12 GHz UWB Planar Triangular Monopole Antenna with Ridged Ground-Plane," *Progress In Electromagnetics Research*, vol. 83, pp. 307–321, 2010.

[42] H. Schantz, "A Brief History of UWB Antennas," *IEEE Aerospace and Electronic Systems Magazine*, vol. 19, no. 4, pp. 22–26, April 2004.

[43] L. Orellana and K. Solbach, "Study of Monopole Radiators for Planar Circuit Integration," in *The 38th European Microwave Conference (EuMC)*, Oct. 2008, pp. 1300–1303.

[44] M. A. Yahia, *Microstrip and Printed Antennas*, ser. Artech House Antenna Library.

[45] A. Locatelli, D. Modotto, F. Pigozzo, S. Boscolo, E. Autizi, C. De Angelis, A.-D. Capobianco, and M. Midrio, "Highly Directional Planar Ultra-Wide Band Antenna for Radar Applications," in *European Microwave Integrated Circuit Conference (EuMIC)*, Oct. 2007, pp. 623–626.

[46] D. Pozar, *Microwave Engineering*. Wiley, 2004.

[47] M. Srifi, S. Podilchak, M. Essaaidi, and Y. Antar, "Compact Disc Monopole Antennas for Current and Future Ultrawideband (UWB) Applications," *IEEE Transactions on Antennas and Propagation*, vol. 59, no. 12, pp. 4470–4480, Dec. 2011.

[48] I. Makris, D. Manteuffel, R. Seager, and J. Vardaxoglou, "Modified Designs for UWB Planar Monopole Antennas," in *Loughborough Antennas and Propagation Conference (LAPC)*, April 2007, pp. 249–252.

[49] M. Mokhtaari and J. Bornemann, "Directional Ultra-Wideband Antennas in Planar Technologies," in *European Microwave Conference 2008*, Oct. 2008, pp. 885–888.

[50] F. Yang and Y. Rahmat-Samii, "Microstrip Antennas Integrated with Electromagnetic Band-Gap (EBG) Structures: A Low Mutual Coupling Design for Array Applications," *IEEE Transactions on Antennas and Propagation*, vol. 51, no. 10, pp. 2936–2946, Oct. 2003.

[51] O. Haraz and A. Sebak, "On The Mutual Coupling of UWB Antenna Arrays Using EBG Layers," in *IEEE Antennas and Propagation Society International Symposium (APSURSI)*, July 2012.

[52] D.-C. Chang, C.-H. Liao, and P. Hsu, "UWB Antenna Array," in *International Workshop on Antenna Technology (iWAT)*, March 2011, pp. 164–167.

[53] R. Kazemi, A. Fathy, and R. Sadeghzadeh, "Ultra-Wideband Vivaldi Antenna Array Using Low Loss SIW Power Divider and GCPW Wide Band Transition," in *IEEE Radio and Wireless Symposium (RWS)*, Jan. 2012, pp. 39–42.

[54] D. Ward, R. Kennedy, and W. Williamson, "Theory and Design of Broadband Sensor Arrays with Frequency Invariant Far-Field Beam Patterns," *J. Acoustic Society*, vol. 97, no. 2, pp. 1023–1024, Feb. 1995.

[55] J. Hong and M. Lancaster, *Microstrip Filters for RF/Microwave Applications*, ser. Wiley Series in Microwave and Optical Engineering. Wiley, 2004.

[56] M. Neinhues, *FIR-Filter basierte Steuerung von ultrabreitbandigen Gruppenantennen*. Doctoral Dissertation, Universität Duisburg-Essen, 2008.

[57] "CVX RESEARCH," http://cvxr.com/cvx/, accessed: 2013-06-1.

[58] E. Wilkinson, "An N-Way Hybrid Power Divider," *IRE Transactions on Microwave Theory and Techniques*, vol. 8, no. 1, pp. 116–118, 1960.

[59] S. B. Cohn, "A Class of Broadband Three-Port TEM-Mode Hybrids," *Microwave Theory and Techniques, IEEE Transactions on*, vol. 16, no. 2, pp. 110–116, 1968.

[60] "ADS Agilent," http://www.home.agilent.com, accessed: 2013-04-01.

[61] J. Schneider, "Marki Microwave," http://www.markimicrowave.com/Assets/ datasheets/PD-0R413.pdf, accessed: 2013-04-01.

[62] E. Pancera, J. Timmermann, T. Zwick, and W. Wiesbeck, "Spectrum Optimization in Ultra-Wideband Systems," *International Journal of Microwave and Wireless Technologies*, vol. 2, pp. 203–209, March 2010.